# Synthesis and Characterization of Carbon nanowalls by ICP- CVD using Aluminium-Acetylacetonate precursor

Von der Fakultät für Physik
der Universität Duisburg-Essen
zur Erlangung des akademischen Grades eines
Doktors der Naturwissenschaften
genehmigte Dissertation

von

**Himani Gaur Jain**

aus

Gulaothi, India

1. Gutachter: Prof. Dr. Volker Buck
2. Gutachter: PD Dr. Christian Pflitsch

Tag der Disputation: 30. August 2012

# Versicherung

Hiermit versichere Ich, dass Ich die vorliegende Arbeit selbständig verfasst und keine aneren als die angegebenen Quellen und Hilfsmittel benutzt habe. Die Stellen der Arbeit, die dem Wortlaut oder Sinn nach anderen Werken entnommen wurden, have ich in jedem einzelnen Fall unter Angabe der Quelle als Entlehnung kenntlich gemacht. Das Gleiche gilt auch für beigegebene Zeichnungen, Kartenskizzen und Darstellungen. Anfang und Ende von Wörtlichen Textübernahmen habe ich durch Anführungszeichen bzw.Zitatformatierung, sinngemäße Textübernahmen durch direkten Verweis auf die Verfasserin oder den Verfasser gekennzeichnet.

Die Arbeit ist noch nicht an anderer Stelle als Prüfungsleistung vorgelegt worden.

(Himani Gaur Jain)

Duisburg, den 29 Mai 2012

# Abstract

*A new method of synthesis of carbon nanowalls using acetylacetonate as metal organic precursor is presented. The films were deposited in ICP-CVD generated argon plasma by varying gas flow rate, plasma power, substrate temperature and reactor pressure. The precursor-feeding rate into the plasma chamber was controlled by the argon gas flow. No catalyst or other carbon gas source was added to deposit such structures.*

*The wall size of CNWs was strongly influenced by the aluminium content present inside the film, plasma parameters like substrate temperature, plasma power and gas flow rate. The smallest wall size observed was 5nm. All films were analysed using SEM, XRD, Raman and TEM techniques in order to characterize the morphology of the samples. XPS, EDX, SIMS, and NRA were used for chemical analysis.*

*The structuring of CNW layers was performed successfully with a pulsed power laser. The resulting cathodes exhibited fairly aligned and efficient field emission (FE) at onset fields for 1 nA of 10-20 V/µm. Local FE measurements of selected CNW patches revealed promising maximum current values up to about 100 µA.*

*Aluminium oxide films were observed when deposited in oxygen/argon plasma. Investigated films consisted of a mixture of polymorphs like $\gamma$, $\theta$, $\kappa$, $\alpha$- $Al_2O_3$.*

# Abstract

*Es wird ein neues Verfahren zur Synthese von Carbon Nanowalls mit Acetylacetonat als metallorganischem Precursor vorgestellt. Die Schichten wurden in einem ICP-CCP generierten Argon-Plasma unter Variation der Gasflussrate, Plasmaleistung, Substrattemperatur und Arbeitsdruck abgeschieden. Die Precursor-Zufuhrrate in die Plasmakammer wurde durch den Argongasstrom gesteuert. Es wurden weder ein Katalysator noch Kohlenstoffgas hinzugefügt.*

*Die Größe der CNWs wurde stark vom Aluminium-Gehalt in der Schicht, von Plasma-Parametern wie Substrattemperatur, Plasmaleistung und Gasfluss beeinflusst. Die kleinste gemessene Wandgröße war 5 nm. Alle Filme wurden mittels REM, XRD, Raman und TEM-Verfahren untersucht, um die Morphologie der Proben zu charakterisieren. XPS, EDX, SIMS, und NRA wurden zur chemischen Analyse verwendet.*

*Die Strukturierung der CNW Schichten wurde mit einem gepulsten Laser durchgeführt. Die damit hergestellten Kathoden weisen eine gut ausgerichtete und effiziente Feldemission (FE) von 1 nA bei Feldern von 10-20 V/µm auf. Lokale FE-Messungen ausgewählter CNW Patches zeigten vielversprechende maximale Stromwerte bis zu etwa 100 µA.*

*Aluminiumoxid-Schichten wurden beobachtet, wenn in einem Sauerstoff/Argon-Plasma abgeschieden wurde. Die untersuchten Schichten bestanden aus einer Mischung von Polymorphen wie $\gamma$, $\theta$, $\kappa$ und $\alpha$- $Al_2O_3$.*

# Acknowledgments

This thesis arose from research that has been done since I joined the group of Prof. Buck. During this time, I worked with many great people whose contribution in assorted ways to the research and the making of the thesis deserves special mention. It is a pleasure to convey my gratitude to all of them in my humble acknowledgment.

Foremost, I would like to give my gratitude to **Prof. Dr. Volker Buck** for his supervision, advice, and guidance from the very early stage of this research. His truly scientific intuition and instincts made him as a constant oasis of ideas and passions in science, which exceptionally inspired and enriched my growth as a student, a researcher and a scientist. I am deeply indebted to him and gratefully acknowledge his contribution to this research as well as this thesis.

I thank **Prof. Dieter Mergel**, for his originality has triggered and nourished my maturity that I will benefit from, for a long time to come.

I have also benefited by advice and guidance from **Dr. Christian Pflitsch** (Thermodynamics), who always kindly granted me his time even for answering some of my unintelligent questions about XRD analysis for Alumina films.

I should also mention **Prof. Günter Müller** who provided me electric field measurements. I am grateful for the chance to visit and be a part of his laboratory.

I am highly thankful to **Prof. P.K.Barhai** for introducing me to University Duisburg for my PhD. Also many thanks for giving a warm welcome and cooperation during my Indo-Germany project visit in India.

I am particularly obliged to **Prof. Ashutosh Sharma** under whose guidance I started my research career at IIT Kanpur. Without the enriching experience I had with you, it would not have been possible to pursue my research career. Many ideas and concepts I learned in your group will always benefit me.

I am grateful in every possible way to **Matthias Haase** especially for his precious time to proof read this thesis and gives critical comments about it.

I would like to thank my friend **Berrin Küzün**. Her unconditional help during my new days at Duisburg, her constant advice about the new culture and system in Germany are more than thanksgiving.

The colleagues of laboratory deserve my sincerest thanks. Their friendship and assistance means more to me than I can ever express. I could not have done my work without

invaluable friendly assistance of the participants. Thank you **Markus Neubert, Monika Timpner**, **Victoria Khlopyanova**, **Oleksiy Filipov**, **Yangyang He, Nicolas Wöhrl** and **Alexei Poukhovoi** for being very nice and kind to me.

I would like to thank the technical staff **Klaus Pärschke**, **Peter Walter** and **Heinz Loffeld** for their support during my experiments.

My thanks also go to **Manish Kulkarni** with whom I spent innumerable hours discussing about my research.

I could not have finished this thesis without the support of my **parents** who were always there for me whenever I needed them. Their encouragement and support kept me going and motivated. I am so obliged for my father in law **Sudhir Kumar** for his support in last years of my PhD and his help has shaped my research career. Thank you my brother **Himanshu** and brother in law **Varun** whose good wishes kept me going forward.

I gratefully thank my dear husband **Vipul** whose support and cooperation has always been my source of strength and inspiration. You always took my problems as your own, helped me to overcome them, and always encouraged me. Thank you so much for your patience and endless help.

I dedicate this thesis to my lovely little daughter **Evisha**. Her lovely smiles fill me with energy and inspire me to go forward and touch my dreams.

# Table of Contents

# List of Figures

# List of Tables

# 1.Introduction

Recent years have seen a rapid growth of interest in carbon nanostructures because of their various applications in electro-chemical devices, field emitters and sensors [1,3,4]. The discovery of carbon nanotubes by lijima [2] has attracted the interest of researchers in graphite like materials. Simultaneously, two dimension carbon structures have also been discovered in various forms like carbon nanohorns [5], carbon nanoflakes [6], carbon nanoflowers [7], carbon nanosheets [8] and carbon nanowalls. The major applications of two-dimensional carbon nanostructures can be electron field emitters and capacitor electrodes. In 2002, Wu et al. [9] observed for the first time carbon wall-like structures which were perpendicular to the substrate. They were called carbon nanowalls (CNWs). It was studied by TEM that CNWs consist of few graphene sheets standing on the substrate.

## 1.1. Various dimensionality of carbon based structures

The property of the bulk material depends on the chemical element and the type of chemical bonds. The bonding of a chemical element forms the material by holding atoms and molecules together. However, on the nanometer scale, this phenomenon no longer exists. Moreover, the chemical bonding, dimensionality and the shape are important factors to determine the properties of a material. Except nanodiamond, most of the carbon nanostructures are self-organized graphite nanostructures composed of graphene. Graphite nanostructures may be classified by their grown dimension as shown in Figure 1. According to the dimensionality carbon materials can be divided into the following categories:

- Three-dimensional (3D) (Diamond, Graphite)
- Two dimensional (2D) (Graphene)
- One dimensional (1D) (Carbon nanotubes)
- Zero dimensional (0D) (Fullerenes)

The basic difference in 2D and 3D is considered by the number of layers of atoms. For example, a single layer of an atomic crystal is considered as 2D carbon whereas 100 layers of carbon form the 3D graphite material [10].

If we focus on work done on carbon nanomaterials in the past, we find that in the last two decades, a lot of work has been done on 0D and 1D carbon nanomaterial [12-16]. 0D carbon (Bucky balls) is formed by wrapping 2D sheets. Fullerene is one of the examples of it. In 1985, Harold Kroto [17] discovered carbon clusters containing C60 [16] and C70 molecules. This discovery helped to determine the properties of fullerenes based on its atomic bonding between carbon atoms and its shapes.

Carbon science went on one step further with the crucial discovery of carbon nanotubes in 1991 [1]. Since the discovery of carbon nanotubes by Iijima, carbon nanostructures of various dimensionalities have become an attractive topic of research. One dimensional carbon structures (carbon nanotubes, carbon nanofibers) have proven to be applicable in electrochemical devices, electron field emitters and hydrogen storage material. The carbon nanotube (CNT), one dimensional carbon, is the form of rolled 2D graphene in one direction. CNTs showed their unique structure and properties and hence are studied widely. CNTs are a good example for excellent mechanical properties, and chemical inertness and high aspect ratio (length /diameter). CNTs can be metal or semiconductors, which offer a wide range of electronic properties. Hence, previous researches were mainly focused on 0D zero dimensional and 1D one dimensional nanostructures

## 1.2. Discovery of two dimensional carbon nanostructures

Graphene is as a basic building block of 0D, 1D and 3D materials [11]. An ideal graphene sheet will spread flat, and this can be classified as two dimensional carbons. Before the experimental proof of stability of 2D graphenes [11], 2D nanomaterials have been avoided. This can be because 2D crystals were considered instable in ambient environment [18-20]. 70 years ago, Peierls and Landau discussed that “a divergent contribution of thermal fluctuation in 2D crystal lattices should lead to such displacement of atoms that they become comparable to inter-atomic distances at any finite temperature” [18-19]. That means graphene can be theoretically described and believed as unstable in

an ambient environment. Wu et al. discovered the growth of two dimensional carbons (well separated graphene sheets) together with carbon nanotubes by microwave PECVD [9].

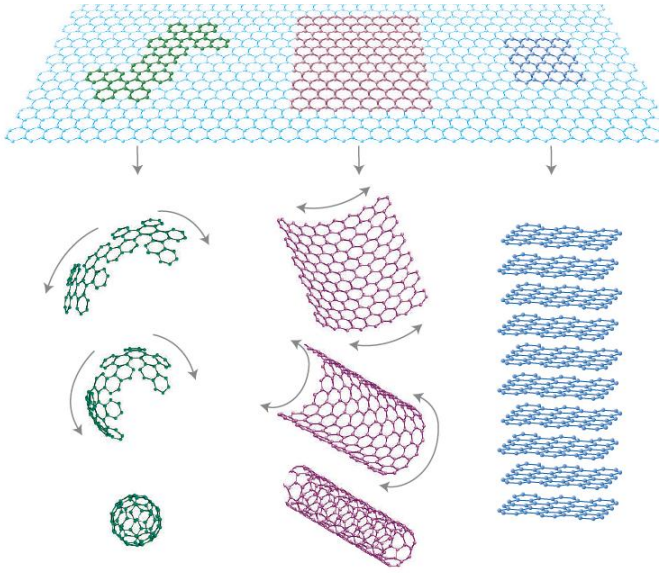

***Figure 1: 2D graphene is the basic building block of all other types of carbon dimensionalities. It can form 0D Bucky balls, 1D nanotubes and 3D graphite.*** *(Ref [11])*

Later on, the combined growth of CNWs and carbon nanotubes have been published in 2007 [21]. This shows that the growth mechanism has a correlation between both materials. Many other kinds of materials have also been discovered with the discovery of fullerene and CNTs like $WS_2$, $MoS_2$, $NbS_2$, BN, $BC_2N$, $BC_3$, $NiC_2$, and CN [22-26]. Such materials have a layered structure in bulk form. When the thin 2D layers decrease into one direction and form a single sheet, 2D sheet becomes unstable and form a curved or rolled-up material.

This is the basic phenomenon for the formation of materials like fullerenes, cages, cones, and tubes. Such nanomaterials have electronic, mechanical, optoelectronic, and magnetic applications because of their unique shape and symmetry. Special attention was drawn in the past to carbon nanotubes because they can be a metal or a semiconductor, depending on the rolling direction in which the graphene sheet is rolled up to form the tubular structure. This unique feature of carbon nanotubes made it attractive for electronic [27-29], optoelectronic [30] and sensor [31-32] applications. Hence it became very popular for further research. Moreover, 2D graphite sheets are studied in an open boundary.

Furthermore, it has more surface area (twice than 1D) than a close boundary like carbon nanotubes and sharp edges. This makes a 2D structure more attractive than 1D rolled-up structures for chemical and biosensor applications and sharp edges are promising for field emission application [10].

## 1.3. Brief description of CNWs

Two dimensional CNWs are nanostructured graphite sheets with edges, which are composed of planar graphene sheets standing vertically on the substrate. The sheets are few nanometers thick and form a network of wall type structures. The most important features of CNWs are high aspect ratio, large surface area and sharp edges. Hence, CNWs can be very useful in nanoelectronics. The most common tool for fabrication of CNW is chemical vapor deposition. It is well known that CNWs and similar structures have been grown using various CVD methods such as RF capacitively coupled plasma assisted by H radical injection [33, 34], radio frequency inductively coupled plasma [35], electron beam excited plasma [36], microwave plasma [9**,** 37, 38], DC plasma [39] hot filament CVD [40, 41], helical wave plasma [42], and by sputtering of a glassy carbon target [43].

## 1.4. Fabrication of CNWs

Chemical vapor deposition is a common method for the fabrication of CNWs. However, some reports have been published on the growth of CNWs by physical deposition [43]. The morphology and structure of CNWs films depend on the source gases, the pressure, the substrate temperature, as well as the type of plasma used for the growth of CNWs. It is observed that CNWs are a kind of porous film having honeycomb network structure, and are segregated nanosheets vertically standing on the substrate. CNWs are highly branch type carbon nanostructures. To find new applications, an isolated, aligned structure and a moderate spacing between the sheets are desired. For example, for electron field emission applications thin and sharp edges and moderate spacing are required. Similarly, for membrane filter applications, a honeycomb structure with controlled spacing between the sheets is required. However, for gas storage applications less aligned, dense CNWs with large surface area are promising.

Synthesis methods of CNWs are similar to those used for diamond films and carbon nanotubes. Typically, gases like $CH_4$ and $H_2$ and additionally argon are used as source gases for the synthesis of CNWs. Similar to the deposition of diamond microwave plasma and inductively coupled plasma are suitable. For the growth of CNWs, high density plasma is necessary for the efficient decomposition of $H_2$ molecules. To date, following methods have been used for the production of CNWs:

- Microwave plasma,
- Radio frequency (RF) inductively coupled plasma,
- RF capacitively coupled plasma assisted by H radical injection,
- Helicon wave plasma,
- Electron beam excitation plasma,
- Hot filament CVD,
- Sputtering of graphite target

## 1.4.1.Synthesis of CNWs by microwave PECVD

The microwave plasma is one of the high density plasmas and is suitable for decomposing $H_2$ molecules to generate H atoms effectively. In general, two types of models are used to fabricate CNWs: NIRIM (The National Institute of Research of Inorganic Materials, Japan) type and ASTeX (Applied science and technology, Inc) type.

In case of the NIRIM-type, MWPECVD systems with simple reactors are used having flexible positions of the substrate in the plasma. A $CH_4/H_2$ plasma is generated in a cylindrical quartz tube, which intersects a rectangular waveguide; the plasma provides the substrate heating.

The ASTex type reactor consists of a cylindrical stainless steel chamber. A discharge from the microwave (2.45 GHz) is coupled from a rectangular waveguide into the cavity via an axial antenna called plasma ball. This plasma ball provides the substrate heating. In this system, at too high pressure or low microwave power, the plasma cannot be sustained. The CVD process would be operated at a pressure of a few tens of mbar. The reactor pressure and microwave power cannot be independently varied. On the other hand, if the microwave power is too high for a given pressure, the plasma becomes

unstable and tends to jump to the quartz window. Wu et al. reported the synthesis of CNWs on various substrates using the NIRIM-type MWPCVD reactor [9, 10, 46, 47]. They successfully investigated the effects of the gas flow rate ratio and the electric field on the formation of CNWs and also studied field emission and electrical transport properties. Typically, CNWs were grown employing a mixture of $CH_4$ and $H_2$ at a total pressure of 0.0013 bar and with a substrate heating to 650-700°C. Chaung et al. [37] reported the growth of CNWs using ASTex type reactor and investigated field emission properties.

## 1.4.2.Synthesis of CNWs by ICP-CVD

The inductively coupled plasma is high density plasma and especially used to etch materials like Si, $SiO_x$, $SiN_x$ and metal films in large scale integration fabrication processes. The plasma is contained inside a chamber which is surrounded by an inductive coil antenna. The ICP is operated at a relatively low pressure below 100 mbar (10 Pa). Two kinds of ICP have been designed: planar and cylindrical.

In the planar geometry, the coil antenna of flat metal wound in spiral works like an electrode. In cylindrical geometry, the antenna is wound like a helical spring. The inductive mode plasma density is much higher than the capacitive mode plasma density. In case of planar geometry, RF power is inductively coupled into the process chamber with a planar-coil antenna through a quartz window. When a time-dependent electric current is passed through the RF coil antenna located on the quartz window, it creates a time-dependent magnetic field around it. It in turn induces the azimuthal electric current in the gas inside the chamber, leading to a breakdown and the production of high density plasma.

## 1.4.3.Synthesis of CNWs by electron beam excited PECVD

Electron beam excited plasma (EBEP) is high density plasma, which is directly introduced by a high current and low energy electron beam [44]. The electron beam energy and the electron current can be controlled independently by changing the accelerating voltage and discharge current. By setting the electron beam energy close to

the energy corresponding to the maximum electron impact ionization cross-section of source gases, highly ionized and dissociated plasmas can be produced even at low pressures. Mori et al. [36] produced high density CNWs at a substrate temperature of 570°C, and a total pressure 2.6 Pa. However, in this case, vertical alignment of CNWs was poor.

### 1.4.4.Synthesis of CNWs by hot filament CVD

Hot filament CVD has been commonly used to grow diamond films since long. It was also used for CNWs growth. Itoh et al. [45] have reported CNW films employing only $CH_4$ gas and a mixture with $H_2$, respectively. The substrate temperature is reported to be 500°C and 800°C. Itoh et al. reported field emission properties of CNW films showing a turn on field of about 2.6 V/μm. The CNWs fabricated by HFCVD method seem less aligned compared to those fabricated by plasma enhanced CVD and microwave plasma CVD. This suggests that an electrical field or ionic species contribute to the growth of CNWs.

## 1.5. Characterization of CNWs

CNWs have been characterized by scanning electron microscopy, transmission electron microscopy, Raman spectroscopy, X-ray diffraction, X-ray photo electron spectroscopy, secondary ion mass spectroscopy and spectroscopic ellipsometry. Considering a variety of possible applications of CNWs, the important factors for studies are the growth controls of CNWs including spacing, thickness, morphology, crystalline and electrical properties. CNWs have a high density of atomic scale graphitic edges that are potential sites for electron field emission. This might lead to applications in flat-panel displays and light sources. Researchers have studied the field emission properties from CNWs and related structures. The key properties of CNWs are vertically standing walls with a high surface to volume ratio which makes them ideal gas storage materials. Several nanoparticles such as Ni, Co, Ni, Fe and Pt were also deposited on the surface of CNWs. CNWs were also used as a template for synthesizing mesoporous materials with high surface areas. CNWs care expected to be a source of high mobility and large sustainability current and can be used for applications as electrodes of batteries and

electro chemical sensors. In the following *Table 1* there is a brief summary of the characterizations of CNWs done so far.

**Table 1: Brief summary of the characterization of CNWs done so far**

| Fabrication Technique | Working Gas | Substrates | Growth Temperature | Characterization Methods |
|---|---|---|---|---|
| Microwave plasma enhanced CVD [9,10,37 46,47, 48] | $H_2$:$CH_4$=5:1, $H_2$:$CH_4$=4:1 or $H_2$:$C_2H_2$=16:1 | Si, stainless steel, Cu, GaAs, and sapphire substrates coated with NiFe, CoFe, FeMn, and CoCrPt catalysts. | 650-700 ºC | SEM, TEM, Raman, field emission, and transport measurement |
| DC arc-discharge Evaporation[49] | Graphite and $H_2$ | Graphite | 25 ºC | SEM, TEM |
| RF-Capacitively coupled PECVD [33,34,36] | $H_2$:$CH_4$, or $H_2$:$CF_4$, or $H_2$:$C_2F_6$ | Si, fused silica, Si, $SiO_2$, $Al_2O_3$, Mo, Zr, Ti, Hf, Nb, W, Ta, Cu, Steel Sapphire | 500-900 ºC | SEM, Raman, transport Properties |
| RF PECVD[40] | Ar:$C_2H_2$:$H_2$ =500:8:1 | $SiO_2$ capped with 5 nm Ni | > 600 ºC | SEM, Raman and XRD |
| Catalytic CVD [45] | $CH_4$ | Stainless steel, Ni on quartz substrate | 400-500 ºC | SEM, Raman, field Emission |
| Hot filament CVD [50] | $H_2$ and $C_2H_2$(3-15%) | Si | 400-700 ºC | SEM, XPS, Raman, field emission |

# 1.6. Film deposition in oxygen plasma

CNW films can be deposited under oxygen plasma to improve random orientation for the large plane sheets [52]. In this work, films were grown by continuous delivery of argon gas, which is the carrier gas of precursor (aluminium acetylacetonate). Oxygen gas introduced directly in the plasma chamber at various flow rates. No carbon content could be found in the film. Aluminium acetylacetonate reacts with oxygen to form aluminium oxide. Hence, amorphous and crystalline films of $Al_2O_3$ were observed. It is well known that aluminium oxide coatings exhibit advantageous mechanical properties as well as high chemical inertness and oxidation resistance at high temperature. Hence, this material is suitable for corrosion protection and as a diffusion barrier [53, 54], advanced dielectrics [55], optical coatings [56] and electro-chromics. The film constitution, like different polymorphs (α, k, δ, γ-$Al_2O_3$) and amorphous alumina, depends on the deposition condition. The thermodynamically stable phase is alpha alumina, and is very often favored in high temperature and high load applications. Further, k and gamma have also proven to be suitable alternatives. However, several reports have been published on aluminium oxide films and reported low temperature deposition of alpha alumina. It is well known that the use of energetic particles in plasma deposition can dramatically influence the substrate temperature. A significant decrease of temperature in the formation of alpha alumina was reported using pulsed magnetron sputtering (>760°C) [57]. It also demonstrated that PECVD may be engineered to deliver a self-limiting growth of metal oxides using pulsed power modulation [57] and also being developed for the deposition of metal oxide/ alumina films. However, few groups have reported substrate temperatures sufficiently low to allow the deposition on tool steels (500°C - 900°C), α alumina at temperatures lower than 500°C is only based on homo-epitaxial and localized epitaxial growth on chromia templates, and the deposition rates were not compatible with the requirement of the tool coating industries. Few groups have reported film formation using plasma enhanced CVD. Due to the insulating properties of alumina utilization of either a high frequency or a pulsed DC discharge is necessary. By driving a discharge amorphous alumina was reported from 200°C to 600°C [58]. The formation of mixtures of γ and α alumina or a pure α alumina by utilizing a bipolar pulsed DC

generator at 650°C substrate temperature was also reported [59]. Hence, the deposition of α alumina coating at low temperature as well as good film quality remains challenges.

# 1.7. Objectives

The focus of this study is the fabrication and characterization of 2D carbon nanowalls. In the early work, CNWs were mainly formed by using $H_2$ and reactive organic gases (carbon sources). In order to go one step further, we introduce a deposition method by metal organic precursor. In this process, there is no need of introducing any organic gas or additional H radicals. Following the systematic study of the effect of aluminium on the morphology of the CNWs and its electron emission properties, we shall carry out the deposition at various substrate temperature, argon gas flow and plasma power.

More importantly, we could also draw some conclusions to achieve high quality CNW devices. High quality CNWs devices are very important in further investigation for uniform field emission properties of CNWs. Special attention has been given to answer the following questions/tasks:

- Is it possible to deposit CNWs without using organic gas and without injecting $H^+$ radicals additionally?
- To investigate the possibilities of the film depositions at various plasma conditions and study the effect on morphology as well as field emission properties.
- Is Al improving the properties of the films? How does it affect the morphology of CNWs?
- Deposition in $O_2$/Ar plasma results alumina films or is it possible to deposit CNWs in this condition too?
- How do the edges and defects affect the properties of CNWs?

## 1.8. Organization of the thesis

The thesis begins with a brief background on CNWs. The next chapter describes a brief overview of the work done so far on graphene-based structures. Chapter 3 includes an introduction of sample preparation, procedures and measurement techniques and the characterization methods of CNWs. Structural analysis like Raman spectroscopy, scanning electron microscopy, tunneling electron microscopy and chemical analysis by X-ray photon spectroscopy, electron diffraction method, secondary ion Mass spectroscopy, nuclear resonance analysis are introduced. The measurement setup and characterization techniques of electric field emission properties of CNWs are discussed in chapter 3. The chapter 4 discusses the results of characterizations of the CNWs. Then field emission properties of CNWs are discussed in chapter 5. Later, Aluminium oxide films are studied in detail for different mechanical applications. Finally, the work is summarized and is followed by brief comments on the future prospects of CNWs.

# References


1. Joseph P.T, Tai N.H, Lee C.Y, Niu H, W.F.Pong, Lin I.N "Field emission enhancement in nitrogen-ion-implanted ultrananocrystalline diamond films" Journal of Applied Physics 103: 2008, 043720
2. Iijima S "Helical microtubules of graphitic carbon" Nature 354:1991, 56
3. Iwata N, Hata Yasunori, Yoshikuni M, Yamamoto H "Preparation of carbon nanofiber emitters for diode type field emission display with organic luminescence thin films" Material Science and Engineering C 27: 2007, 1174-1180
4. Rao CN, Seshadri R, Govindraj A, Sen R "Fullerenes, nanotubes, onions and related carbon structures" Material Science and Engineering 95: 1995, 209-262
5. Aissa B, Hamoudi Z, Takahashi H, Tohji K, Mohamedi M, Khakani M "Carbon nanohorns-coated microfibers for use as free-standing electrodes for electrochemical power sources" Electrochemistry Communications 11: 2009, 862-866
6. NuLi Y, Guo P. Z, Liu H, Yang J, Wang J "Nickel-cobalt oxides/carbon nano flakes as anode materials for lithium-ion batteries" Material Research Bulletin 44: 2009, 140-145
7. Xiying Ma, Yuan B "Fabrication of carbon nano flowers by plasma-enhanced chemical vapor deposition" Applied Surface Science 255: 2009, 7846-7850
8. Kuang Q, Xie S.Y, Jiang Z.Y, Jiang Z.Y, Zhang X-H, Xie Z-X, Huang R. B, Zheng L.S , "Low temperature solvothermal synthesis of crumpled carbon nanosheets" Carbon 42: 2004, 1737 -1741
9. Wu Y, Peiwen Q, Towchong C, Shen Z "Carbon nano walls growth by microwave plasma enhanced vapor deposition" Advanced Materials 14(1): 2002, 65-67.
10. Wu Y, Yang B, Zong B, Sun H shen Z, feng Y "Carbon nanowalls and related materials" Journal of Materials Chemistry 14: 2004, 469-477
11. Geim AK and Novoselov KS "The rise of Graphene" Nature Materials 6: 2007, 183-191
12. Ebbesen TW, Ajayan PM "Large scale synthesis of carbon nanotubes" Nature 358: 1992, 220

13. Lieber CM “Nano scale science and technology: Building a big future from a small things.” MRS Bulletin 28: 2003, 486-491
14. Aiken JD, Finke RG “A review of modern transition –metal nano clusters: their synthesis, characterization and application in catalysis” Journal of Molecular Catalysis A : Chemical, 145: 1999, 1-44
15. Borovitskaya E, Shur MS “Quantum Dots” Worlds Scientific, New Jersey, 2002
16. Kratschmer W, Lamb L D, Fostiropoulos K, Huffman D R “Solid C60: a new form of carbon” Nature 347, 1990, 354–358
17. Kroto HW, Heath JR, Brien SCO, Curl RF, Smally RE “ C60 Buckmicterfullerene” Nature 318: 1985 ,162-163
18. Peierls RE “Quelques proprietes typiques des corpse solides” Ann. I.H. Poincare 5:1935, 177-222
19. Landau LD “Zur Theorie der Phasenumwandlungen II” Phys. Z. Sowjetunion.11: 1935, 26-35
20. Landau LD , Lifshitz EM, Statistical Physics, part I, Pergamon, Oxford, 1980.
21. Malesevic A, Vizireanu S, Kemps R, Vanhusel A, Haesendonck C.V, Dinescu G “Combined growth of carbon nanotubes and carbon nano walls by plasma-enhanced chemical vapor deposition” Carbon 45: 2007, 2932-2937
22. Feldman Y, Wasserman E, Srolovitz D J, Tenne R “High rate, gas phase growth of MoS2 nested inorganic-fullerenes and nanotubes” Science 267: 1995, 222
23. Nath M, Rao CNR “Nanotubes of the disulfides of groups 4 and 5 metals” Pure Applied Chemistry 74 :2002, 1545
24. Jishi RA, White CT Mintmire J W “Endohedral selenium chains in carbon, boron nitride, and BC2N nanotubes” International Journal of Quantum Chemistry 80: 2000, 480
25. Hacohen YR, Poovitz-Biro R, Grunbaum E, Prior Y, Tenne R “Vapor–Liquid–Solid (VLS) Growth of NiCl2 nanotubes via reactive gas laser ablation” Advance Materials 14: 2002, 1075
26. Dresselhaus MS, Drasselhaus G, Eklaund PC “Science of fullerenes and carbon nanotubes” Acedemic, New York, 1996
27. Tans SJ, Verschueren A R M, Dekker C “Room-temperature transistor based on a single carbon nanotube” Nature 393: 1998, 49

28. Avouris P, “Carbon nanotube electronics” Chemical Physics 281: 2002, 429
29. Javey A, Guo J, Wang Q, Lundstrom M, Dai H “Ballistic carbon nanotube field-effect transistors” Nature 424: 2003, 654
30. Misewich JA, Martel R, Avouris P, Tsang J C, Heinze S, Tersoff J“ Electrically induced optical emission from a carbon nanotube FET” Science 300: 2003,783
31. Kong J, Franklin N R, Zhou C, Chapline M G, Peng S, Cho K Dai H “Nanotube molecular wires as chemical sensors” Science 287: 2000, 622
32. Modi A, Koratkar N, Lass E, Wei B Q, Ajayan P M“ Miniaturized gas ionization sensors using carbon nanotubes” Nature 424: 2003, 171
33. Hiramatsu M, shiji K, Amano H, Hori M “Fabrication of vertically aligned carbon nanowalls using capacitively coupled plasma-enhanced chemical vapor deposition assisted by hydrogen radical injuction” Applied Physics Letters 84: 2004, 4708
34. Hirmatsu M, Hori M “Fabrication of carbon nanowalls using novel plasma processing” Japanese Journal of Applied Physics 45: 2006, 5522-5527
35. Wang JJ, Zhu MY, Outlaw RA, Zhao X, Manos DM, Holloway BC, et al. “Free-standing sub nanometer graphite sheets” Applied Physics Letters 85(7):2004, 1265–7
36. Mori T, Hiramatsu M, Yamakawa K, Takeda K, Hori M “Fabrication of carbon nanowalls using electron beam excited plasma enhanced chemical vapor deposition” Diamond and Related Materials 17: 2008, 1513-1517
37. Chuang ATH, Boskovic BO, Robertson J “Freestanding carbon nanowalls by microwave plasma-enhanced chemical vapour deposition” Diamond and Related Materials 15: 2600, 1103- 1106
38. Shrivastva SK, Shukla AK, Vannkar VD, Kumar V “Growth structure and field emission characterization of petal like carbon nano structured thin films” Thin Solid Films 492: 2005, 124- 130
39. Kurita S, Yoshimura A, Kawamoto H, Uchida T, Kojima K, Tachibana M “Raman spectra of carbon nanowalls grown by plasma-enhanced chemical vapor deposition” Journal of applied Physics 97 :2005, 104320-5
40. Shang N, Papakonstantinou P, McMullan M, Chu M, Stamboulis A, Potenza A, Dhesi S.S. Marchetto H “Catalyst free efficient growth, orientation and biosensing properties of multilayer graphene nanoflakes films with sharp edge planes” Advanced Functional Materials18: 2008, 3506-3514

41. Shimabukuro S, Hatakeyama Y, Takeuchi M, Itoh T, Nonomura S, “Preparation of carbon nanowalls by hot- wire chemical vapor deposition and effect of substrate heating temperature and filament temperature” Japanese Journal of Applied Physics 47: 2008, 8635- 8640
42. Sato G, Morio T, Kato T, Hatakeyama R “Fast growth of carbon nano walls from pure methane using helicon plasma-enhanced chemical vapor deposition” Japanese journal of Applied Physics 45 (6A): 2006, 5210-5212
43. Zhang H, Kikuchi N, Koguru T, Kusano E “Growth of carbon with vertically aligned nanoscale flake structure in capacitively coupled RF glow discharge” Vacuum 82: 2008, 754-759
44. Okitsu K, Imaizumi M, Yamaguch K, Khan A, Yamaguchi M, Ban M etal “Reduction of plasma-induced damage by electron beam excited plasma CVD” Solar Energy Materials & Solar Cells 65: 2001, 185-191
45. Itoh T, Shimabukuro S, Kawamura S, Nanomura S “Preparation and electron field emission of carbon nanowalls by cat-CVD” Thin Solid Films 501: 2006, 314-317.
46. Wu Y, Yang B, Han G, Zong B, Ni H, Luo P “Fabrication of a class of nano structured materials using carbon nanowalls as templates” Advanced Functional Material 12: 2002, 489-494
47. Wu Y, Yang B.J “Effects of Localized Electric Field on the Growth of Carbon Nanowalls”, Nano Letters 2 :2002, 355
48. Tanaka K, Yoshima M, Okamoto A, Ueda K “Growth of carbon nanowalls on a SiO2 substrate by microwave plasma-enhanced chemical vapor deposition”, Japanese Journal of Applied Physics 44: 2005, 2074-2076
49. Ando Y, Zhao X, Ohkohchi M “Production of petal- like graphite sheets by hydrogen arc discharge” Carbon 35: 1997; 153-158
50. Dikonimos T, Giorgi L, Giorgi R, Lisi N, Salernitano E, Rossi R “DC plasma enhanced growth of oriented carbon nanowall films by HFCVD” Diamond and Related Materials, 16: 2007, 1240-1243
51. Kondo H, Hori M, Takeuchi W, Hiramatsu M “Controlled Synthesis of Carbon Nanowalls for Carbon Channel Engineering Key Engineering Materials 470:2011, 85-91

52. Takeuchi W, Takedia K, Hiramatsu M Tokuda Y, kanu H, Kimura S, Sakata O, Tajiri H, Hori M "Monolithic selfstaining nanographene sheet using plasma enhanced chemical vapor deposition" Physics Status Solidi 207: 2010, 139-143
53. Schneider JM, Sproul WD, Voevodin AA, Matthews A "Crystalline alumina deposited at low temperature by reactive ionized magnetron sputtering" Journal of Vacuum Science and Technology A 15: 1997, 1084-1088
54. Serra E, Benamati G, Ogorodnikova OV "Hydrogen isotopes transport parameters in fusion reactor materials" Journal of Nuclear Matter 255: 1998, 105-115
55. Cho B-O, Lao SX, Chang JP "The Origin and Effect of Impurity Incorporation in Plasma Enhanced ZrO2 Deposition" Journal of Applied Physics 93: 2003, 9345-9351
56. Martinu L, Poitras D "Plasma deposition of optical films and coatings: A Review" Journal of Vacuum Science and Technology A 18: 2000, 2619-2645
57. Szymanski SF, Michael TS, Colin AW "Effect of wall conditions on the self-limiting deposition of metal oxides by pulsed plasma-enhanced chemical vapor deposition" Journal of Vacuum Science and Technology A 25: 2007, 1493-1499
58. Lin CH, Wang HL, Hon MH "Preparation and characterization of aluminium oxide films by plasma enhanced chemical vapor deposition" Surface Coating and Technology 90: 1997, 102-106
59. Tabersky R, van den Berg H, König U "Plasma chemical vapour deposition of aluminium oxide on hard metals" International Journal of Refractory Metals and Hard Mater 14: 1996, 79-84
60. Hiramatsu M, Inayoshi M, Yamada K, Mizuno E, Nawata M,Ikeda M, Hori M, Goto T "Hydrogen radical assisted radio frequency plasma enhanced chemical vapor deposition system for diamond formation" Review of Scientific Instrument 67: 1996, 2360-2365

# 2.Graphene based structures

Chapter one introduced 2D carbons such as CNWs and the innovative method to deposit the aluminium doped CNWs in inert gas atmosphere as well as alumina deposition under oxygen atmosphere. Now we know CNWs are composed of a few layers of graphene. Hence, a basic introduction is necessary discussing about graphene based structure. This chapter is an overview of graphene-based structures such as graphene bi-layer or multilayer, graphene nanoribbons, nanoflakes or nanodots, two-dimensional carbon sheets and carbon flowers. The detailed background is necessary to convince the reader that 2D carbon nanostructures are worth investigating.

Theoretically, graphene is the two-dimensional form of carbon. The hexagonal arrangement of carbon atoms is the base of all kinds of graphite structures like carbon nanotubes, fullerenes and carbon nanowalls. The synthesis of two-dimensional atomic crystals like graphene, have usually failed ending up with nanometer-sized crystallites. This happens because during synthesis, graphene collapses into other carbon allotropes due to its large edge to surface ratios. Synthesis of graphene finished the common belief that two-dimensional crystals cannot exist.

## 2.1. Synthesis of Graphene

Thin film can be synthesized by following two methods:

- Top - Down method
- Bottom - Up method

Top-down fabrication is a subtractive process starting from bulk materials to small size structures. Bottom-up fabrication is an additive process that starts with precursor atoms or molecules to make nanomaterials. The most common top-down fabrication method is mechanical exfoliation from bulk graphite.

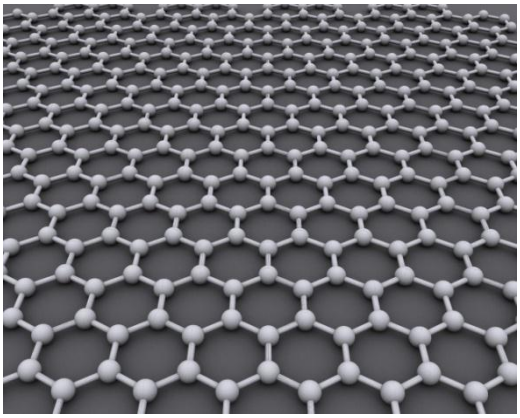

***Figure 2: Graphene based structure***

## 2.2. Top-down methods

### 2.2.1.Micromechanical cleavage

Micromechanical cleavage process can be explained by a graphite lead pencil. Writing with a graphite pencil creates graphene sheets spread over the paper. However, this method leaves many sheets of graphene with uncontrollable thickness at random places. Hence, it is very difficult to locate such monolayers of graphene sheets. This problem was for the first time resolved in 2004 by producing graphene by micromechanical exfoliation [61]. It is nothing but repeated peeling of a small amount of highly oriented pyrolytic graphite by means of an adhesive tape. This approach is good for the production of pure, mobile promising of optoelectronic graphene sheets. This method is the best choice for fundamental research to obtain single layer graphene (SLG). However, for large-scale industrial purposes, this method is quite impractical. The production of graphene in large scale is necessary for the industrial application. Another method of the fabrication of graphene in the top-down manner is liquid phase exfoliation. [86]

### 2.2.2.Liquid-phase exfoliation

This is a wet chemical dispersion process in either aqueous [62] and non-aqueous solvents [63] followed by ultra-sonication. Dispersion by mild sonication in water with sodium deoxycholate is widely used followed by a sedimentation-based ultracentrifugation that can result in single layer graphene sheets. Liquid phase exfoliation is also used to produce graphite-intercalated compounds [64] and expandable graphite

[65]. Graphite flakes are typically in a solution. A long sonication time is needed to break the van der Waals force in graphite. However, from this method, small flakes can also be produced. Graphite flakes and graphite ribbons with the extent of some nanometers can be obtained by liquid phase exfoliation [66]. This offers stability and there is no need for an expensive growth substrate.

### 2.2.3.Carbon segregation

This method is nothing else but the segregation of carbon from a different surface. For example, carbon can be segregated from silicon carbide [67, 68, 69] (SiC) or metal substrates [70, 71, 72, 73, 74] followed by high temperature annealing. High quality graphene was deposited on a SiC substrate and in argon atmosphere [75]. The quality is enhanced when treated with Hydrogen [76]

### 2.2.4.Chemical synthesis

Graphene layers or carbon nanosheets have been produced by chemical synthesis [77]. From the organic synthesis, graphene like polyaromatic hydrocarbons have been produced [78]. Chemical synthesis is used for the fabrication of larger layers. Furthermore, atomically precise large layer graphene can be obtained from this method. Chemical synthesis is the method by which ordered layers with precise control of orientation and spacing [79] are achieved. Hence, this method is also good for the production of graphene because of the good parameter control, especially for tuning the optoelectronic properties.

### 2.2.5.Transfer Printing

Transfer printing is very common in semiconductor manufacturing. Xiaogan Liang et al. [81] fabricated high-quality graphene by transfer printing method. In this method, firstly, one has to lithographically pattern pillars onto a stamp, then apply the stamp (with pressure) to a fresh graphite surface, and then lift it off. Now the pillar has to be stamped on to the desired surface (ex $SiO_2$ surface) [80, 81]. Kim et al. used a dry method based on a poly di methyl siloxane stamp to transfer patterned films [82]. Reina et al. reported [80] the transfer of single layer graphene and few layers graphene from $SiO_2$/Si to other

substrates. A layer of poly methyl methacrylate (PMMA) was coated on graphene deposited on $SiO_2$, then subsequently detached by partial $SiO_2$ etching.

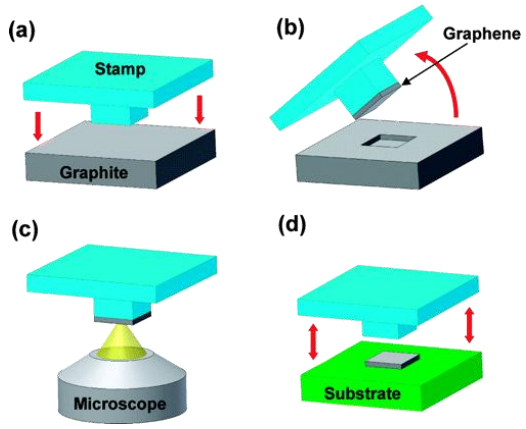


***Figure 3: Synthesis of graphene by transfer printing***

The PMMA/graphene membrane was then placed over the target substrate, and PMMA was dissolved with acetone. Bae et al. [85] scaled the process to layer-by-layer transfer onto plastic substrates. A water layer [86] was placed between the PMMA/graphene foil and the substrate so that, the PMMA could move. By this method, any substrate can be used and the position of the placement can be defined independently.

## 2.3. Bottom- Up methods

### 2.3.1.Chemical vapor deposition

The bottom-up approach starts with carbon atoms and tries to assemble graphene sheets. Chemical vapor deposition (CVD) and molecular beam epitaxy (MBE) are two typical bottom-up approaches. Single layer graphene and few layers graphene can now be grown on various substrates by feeding hydrocarbons at a suitable temperature [71, 79, 82, 84, 85 86, 87]. In addition, plasma-enhanced CVD can be applied on substrates without a catalyst [87]. The films, which are grown by CVD, are generally multi-layer graphene. However, Raman spectra of multi-layer graphene and single layer graphene are observed to be similar [83]. Graphene has been synthesized by CVD and additionally an annealing step by many researchers [83, 88, 89, 90, 91]. The number of layers and the sheet sizes can be controlled easily.[92] However, the electron mobility of epitaxial graphene are comparatively lower than that of exfoliated graphene.[93] Furthermore, isolating single

sheets is difficult and additional lithography is required to pattern electrostatic gates on top of the epitaxial graphene. Transition-metal-catalyzed graphene growth was demonstrated to yield macroscopic single-crystalline graphene domains with very low defect density and outstanding thickness control [91]. It is still a challenge to find a way to transfer the graphene layers to an insulating surface. Those recent successful demonstrations of the fabrication of large graphene layers by CVD/epitaxial CVD growth pave ways to mass-produce graphene. However, the advances are still far from finished. A true leap forward should be the atomically precise synthesis of graphene nanostructures by 'bottom up' approaches. In summary, exfoliation remains the preferred method for most of the experimental research groups around the world. Recent successful fabrication of large graphene layers by CVD/Epitaxial CVD growth opened ways to mass-produce graphene. These various methods have led to high-quality single-crystalline graphene systems, which can be used for further fundamental research, as well as large-scale graphene wafers, which can be employed in device fabrication and integration.

## 2.4. Properties of Graphene

The single layer of carbon atoms, which forms a benzene ring structure, is named Graphene. Graphene can be used to explain the properties of carbon-based material like carbon nanotubes, large fullerenes, carbon walls etc.

### 2.4.1.Electronic Properties

Graphene is a semimetal or zero band gap semiconductor. Graphene has high electron mobility 28,000 $cm^2V^{-1}$ $S^{-1}$. Experimental reports show that electrons and holes have the same mobility in graphene. Therefore, it can continuously tune the charge carriers type from electron to hole. At low temperatures and high magnetic fields, the exceptional mobility of graphene has been observed according to the quantum Hall effect for both electrons and holes [95, 96]. Due to its unique band structure, the graphene quantum Hall effect shows that Hall Effect in graphene occurs at half integers of $4e^2/h$ rather than at the typical integers of $4e^2/h$. The corresponding resistivity of graphene is $10^{-6}$ $\Omega \cdot cm^{-1}$, which is less than the resistivity of silver. Because graphene has no band gap, the corresponding resistivity change is small.

## 2.4.2.Mechanical properties

Atomic force microscopy is commonly used to measure the strength of graphene. Graphene is pressed by a small tip, which is made of a hard material like diamond. Interestingly graphene is harder than diamond and more or less 300 times harder than steel. The tensile strength of graphene exceeds 1 TPa. Even though graphene is so robust, it is also very stretchable. It can be stretched up to 20% of its initial length. Graphene can be a super strong composite material in the near future.

## 2.4.3.Optical properties

Graphene, despite being the thinnest material ever made, is still visible to the naked eye. Approximately, 2.3 % visible light cannot pass through a single layer of graphene. When graphene is deposited on a silicon wafer (having a thin layer of silicon dioxide), the visibility of graphene is enhanced. The three-layer structure (graphene, silicon dioxide and silicon wafer) makes complex interference effects when light passes through it. Depending on the silicon dioxide layer thickness, some colors of light are enhanced and others are suppressed. This is somehow like a rainbow effect which can be visible together with graphene films.

## 2.4.4.Chemical properties

Graphene shows the tendency of absorption and desorption of various molecules like $NO_2$, OH just like graphite. The absorbents generally act as donors hence graphene remains always a conductor. This nature of graphene can be used as a sensor for chemicals. Also, with weak absorbents, graphene functionalized with some chemical group like $OH^-$ or $F^-$ forms graphene oxide or fluorinated graphene. It is noticed that single layer graphene is more reactive than multi or bi-layer graphene, the edges are being reactive than the center part of the film. Unless, the graphene is not being with very harsh reactive conditions, graphene is normally inert material.

# 2.5. Applications of graphene

The applications of graphene have been proposed in many fields. Examples are touch screen displays, LCDs, single molecule sensors, and hard composite material.

The excellent electronic, mechanical and optical properties of graphene attract the attention in flexible electronics like touch screen displays. Bae et al. [85] have produced roll-to-roll production of graphene sheet that will be used as a transparent electrode. Graphene is one of the strongest and stiffest known materials and has very lightweight. It suggests that graphene can be mixed with plastics such as epoxy to make composites, which have good specific physical properties (i.e. strength per unit mass). As graphene is electrically conductive, it can also be used for electro mechanical properties. The graphene plastic composite will be electrically conductive and mechanically strong. Therefore, it will be a good replacement of metals. Conductive plastics are very demanding and are used mostly for the protection of carbon fiber aircraft wings against lightning strikes. They also prevent sparks due to static electricity in the fuel lines and tanks of vehicles. These are some suggestions for the use of graphene. Graphene is an emerging material having outstanding properties. It can decorate the world by very high perfection by means of smallest size, lightweight, excellent electromechanical features and good optical vision.

# Summary

Graphene, which is the basic building block of all kinds of carbon nanostructures, has very unique properties due to its charge transport. The very attractive properties of Graphene (like high charge mobility, ultra hardness, chemically inertness) make the graphene-based nanostructures worth investigating. The synthesis of graphene described in this chapter is very similar to the synthesis of other two-dimensional carbon nanostructures like carbon nanowalls etc. The charge transport of multi-layer graphene sheets is different from single and multi-layer graphene sheets. CNWs are nothing else but the multi-layer graphene sheets standing vertically on the substrate having lots of defects and vacancies.

# References


61. Novoselov KS, Geim AK, Morozov SV, Jiang D, Zhang Y, Dubonos SV, et al. "Electric field effect in atomically thin carbon films" Science 2004; 306 (5296): 666–9
62. Sutter PW, Flege J-I, Sutter E A "Epitaxial graphene on ruthenium" Nature Materials 7: 2008,406–411
63. Lotya, M, Hernandez Y, King P J, Smith RJ, Nicolosi V, et al. "Liquid phase production of graphene by exfoliation of graphite in surfactant/water solution" Journal of the American Chemical Society 131: 2009, 3611–3620
64. Hernandez Y, Nicolosi V, Lotya M, Blighe FM., Sun Z, De S et al. "High-yield production of graphene by liquid-phase exfoliation of graphite" Nature Nanotechnology 3: 2008, 563–568
65. Green AA, Hersam MC "M. C. Solution phase production of graphene with controlled thickness via density differentiation" Nano Letters 9: 2009, 4031–4036
66. Valle C, Drummond C, Saadaoui H, Furtado C A, He M, Roubeau O et. al. "Solutions of negatively charged graphene sheets and ribbons" Journal of the American Chemical Society 130 : 2008, 15802–15804
67. Li X, Wang X, Zhang L, Lee S, Dai H "Chemically derived ultra smooth graphene nano-ribbon semiconductors" Science 319: 2008, 1229–1232
68. Berger C, Song Z, Li T, Li X, Y A, Feng OR "Ultrathin epitaxial graphite: 2D electron gas properties and a route toward graphene-based nanoelectronics" Journal of Physical Chemistry B 108: 2004, 19912–19916
69. Acheson EG "Production of artificial crystalline carbonaceous materials; article of carborundum and process of the manufacture there of carborundum" US patent 1896, 615-648
70. Badami D V "Graphitization of α-silicon carbide" Nature 193: 1962, 569–570

71. Eda G, Fanchini G, Chhowalla M "Large-area ultrathin films of reduced graphene oxide as a transparent and flexible electronic material" Nature Nanotechnology 3: 2008, 270-274
72. Vijayaraghavan A, Sciascia C, Dehm S, Lombardo A, Bonetti A, Ferrari A C et al. "Dielectrophoretic assembly of high-density arrays of individual graphene devices for rapid screening" ACS Nano 3; 2009, 1729–1734
73. Oshima C, Nagashima A "Ultra-thin epitaxial films of graphite and hexagonal boron nitride on solid surfaces" Journal of Physics: Condensed Matter 9: 1997, 1–20
74. GamoY, Nagashima A, Wakabayashi M, Terai M, Oshima C "Atomic structure of monolayer graphite formed on Ni(111)" Surface Science 374: 1997, 61–64
75. Virojanadara C, Yakimova R , Zakharov A A, Johansson L I "Large homogeneous mono-/bi-layer graphene on 6H–SiC (0 0 0 1) and buffer layer elimination" Journal of Physics D: applied physics 43 :2010, 374010
76. Isett L C, Blakely J M "Segregation isosteres for carbon at the (100) surface of nickel" Surface Science 58: 1976, 397- 414
77. Emtsev KV, Bostwick A, Horn K, Jobst J, Kellogg GL, Ley L, et al. "Towards wafer-size graphene layers by atmospheric pressure graphitization of silicon carbide" Nature Materials 8: 2009, 203-207
78. Riedl, C, Coletti C, Iwasaki T, Zakharov A A, Starke U "Quasi-free-standing epitaxial graphene on SiC obtained by hydrogen intercalation" Physical Review Letters103: 2009, 246804
79. Choucair M, Thordarson P, Stride J A "Gram-scale production of graphene based on solvothermal synthesis and sonication" Nature Nanotechnology 4: 2009, 30-33
80. Reina A. Son H, Jiao L, Fan B, Dresselhaus MS, Liu ZF "Transferring and identification of single-and few-layer graphene on arbitrary substrates" Journal of Physical Chemistry C 112 2008, 17741-17744
81. Liang X, Fu Z, Chou S Y "Graphene transistors fabricated via transfer-printing in device active-areas on large wafer" Nano Letters 7(12): 2007, 3840-3844

82. Wang X. Zhi L, Tsao N, Tomović Ž, Li J, Müllen K "Transparent carbon films as electrodes in organic solar cells" Angewandte. Chemie. 47 : 2008, 2990-2992
83. Wu J, Pisula W, Mullen K "Graphenes as potential material for electronics" Chemical Review 107: 2007, 718-747
84. Kim K S, Zhao Y, Jang H, Lee S Y, Kim J M, Kim KS et al. "Large-scale pattern growth of graphene films for stretchable transparent electrodes" Nature 457: 2008 706-710
85. Bae S. Kim H , Lee Y , Xu X , Park Jae-Sung , Zheng Y , et al. "Roll-to-roll production of 30-inch graphene films for transparent electrodes" Nature Nanotechnology 4 : 2010, 574-578
86. Bonaccorso F, Sun Z, Hasan T , Ferrari A C "Graphene photonics and optoelectronics" Nature Photonics 4: 2010, 611-622
87. Karu A E, Beer M "Pyrolytic formation of highly crystalline graphite films" Journal of Applied Physics 37: 1966, 2179-2181
88. Oshima C, Nagashima A "Ultra-thin epitaxial films of graphite and hexagonal boron nitride on solid surfaces" Journal of Physics: Condensed Matter 9: 1997, 1-20
89. Wang J, Zhu M , Outlaw RA , Zhao X , Manos DM, Holloway Br C "Synthesis of carbon nanosheets by inductively coupled radio-frequency plasma enhanced chemical vapor deposition" Carbon 42 : 2004, 2867- 2872
90. Yu Q, Lian J, Siriponglert S, Li H, Chen YP, Pei S "Graphene segregated on Ni surfaces and transferred to insulators" Applied Physics Letters 93: 2008, 113103
91. Hernandez Y, Nicolosi V, Lotya M, Blighe F M, Sun Z, De S, et al. "High yield production of graphene by liquid phase expholiation of graphite" Nature Nanotechnology 3: 2008, 563 - 568
92. Yuana GD, Zhang WJ, Yang Y, Tang YB, Li YQ, Wang JX etal "Graphene sheets via microwave chemical vapor deposition", Chemical Physics Letters 467: 2009, 361-364

93. Berger C, Song Z, Li T, Li X, Ogbazghi A Y, Feng R, et al. “Ultrathin epitaxial graphite: 2D electron gas properties and a route toward graphene-based nanoelectronics” Journal of Physical Chemistry B 108: 2004, 19912-19916
94. Novoselov K S, Jiang Z, Y Zhang, Morozov SV, Stormer HL, Zeitler U et al. “Room-Temperature Quantum Hall Effect in Graphene” Science 315: 2007, 1379
95. Zhang Y, Tan YW, Storme HL, Kim P “Experimental observation of the quantum Hall effect and Berry's phase in graphene” Nature 438: 2005, 201-204

# 3. Experimental Techniques

This chapter presents the basic science of fabrication and measurement techniques used for CNW synthesis. It begins with a description of the deposition and characterization methods of CNWs followed by basic details of CNWs electric field emission measurements. Synthesis of CNWs by CVD deposition and characterization techniques like Raman spectroscopy, scanning electron spectroscopy (SEM), X-ray Photon spectroscopy (XPS) are briefly explained.

## 3.1. Synthesis methods

### 3.1.1.Chemical vapor deposition

Chemical vapor deposition is a chemical process which is used to produce thin solid films. In this process, the gaseous molecules (which are called precursors) are introduced in a chemical reaction and then solid material growths at the surface form a film (powder etc). CVD is used in very wide areas like the production of powder, fibers and coatings. Very wide research on CVD has proved that it can produce mostly any kind of material like metals, non-metals, compounds of carbon and silicon like oxides, nitrides, and borides.

When the chemical process is proceeded with a plasma, it is called plasma enhanced CVD. Plasma is generated in an electromagnetic field which is set between two electrodes (top electrode and ground substrate). An electron collision takes place with gas molecules and forms ions and reactive neutrals. The total charge neutralizes with all reactive elements and sustains plasma inside the reactor. Plasma enhanced CVD is very useful for low substrate temperatures. In brief, CVD can be designed according to need but the basics of CVD are the dispensing gases, the temperature control and the produced bi-products. Sustaining the plasma is additional in plasma CVD.

## 3.1.2.ICP-CVD

There has been a growing interest in inductively coupled plasmas (ICP) because of the necessity for high-density plasma sources for plasma-aided manufacturing of thin films. This kind of CVD is designed to use an inductive circuit element near to discharge region. It helps in producing more ions inside the plasma. A spiral like conductor is used as the inductive circuit element. The inductor is tuned by an electrical reactance, in the way that a special electrical resonance RF frequency is obtained. From this resonance circuit, a huge amount of RF current is produced in the inductive element. From this RF current RF magnetic field generates, and this field penetrates the discharge region [99]. It can be explained by the Faraday's law,

$\Delta E = -dB/dt$,

where E is the electric field, B is the flux density. According to Faraday's law, time-varying RF magnetic flux density (B) induces a solenoidal RF electric field (E).

Hence, the solenoidal electric field accelerates free electrons in the discharge and sustains the plasma. It is reported that a weak, capacitively coupled electric field discharge in inductively coupled plasma sources at low absorbed powers is also observed during this process [96-98]. With increasing the RF power the luminosity and density increases at high pressures above $\sim 3\times 10^{-2}$ mbar (which is due to the inductive coupling or the H-discharge [99]). The two kinds of coupling (capacitive or inductive, E or H) have their own particular properties, hence it has been a matter of debate since the inductive plasma was discovered [98]. However, some attempt to minimize the capacitive coupling (negative side effect) has been implemented like by placing shields between the inductive coupler and the discharge wall. Because inductive couplers have high electrical potentials hence, it is not 100% inductively coupled plasma. However, high density plasma which is partially inductively coupled is called inductively coupled plasma CVD [99].

**Key features**

- Independent control of ion energy and ion current density
- Typical process pressure: $1.3 \times 10^{-3} - 1.3 \times 10^{-2}$ mbar
- Plasma density: circa $5 \times 10^{11}$ particles /$cm^2$

- Plasma in contact with the substrate
- Low energy ion current during deposition
- Ion current (plasma density) dependent on ICP power
- ESS (electrostatic screen) for a purely inductive plasma

**Typical applications of ICP CVD:**

- Low temperature deposition for lift off technology
- Low temperature deposition of very high quality $SiO_2$
- Low temperature deposition of poly Si
- ICP is fully automatic (2 RF automatic units)

## 3.1.3.Synthesis process of CNWs by ICP-CVD

CNWs have been synthesized by many kinds of CVD like microwave plasma enhanced CVD, capacitively coupled plasma enhanced CVD, hot filament CVD, etc. Mostly reporters used reactive organic gases as source of carbon. Almost all kinds of substrates have been used to deposit CNWs by CVD. Here, we briefly describe the CNW deposition on silicon and stainless steel substrates by using aluminium acetyl acetonate as the precursor. Inductively coupled plasma enhanced chemical vapor deposition was used to deposit CNWs. The schematic diagram is shown in Figure 6. The deposition chamber consists of a cylindrical reactor chamber holding a substrate holder which is directly connected to the heater. Plasma is sustaining inside this chamber, which is surrounded by an inductive-coil antenna. The working pressure is maintained approximately at $10^{-2}$ mbar in the chamber. Solid precursor aluminium acetylacetonate is used as a source of carbon and aluminium for CNWs deposition.

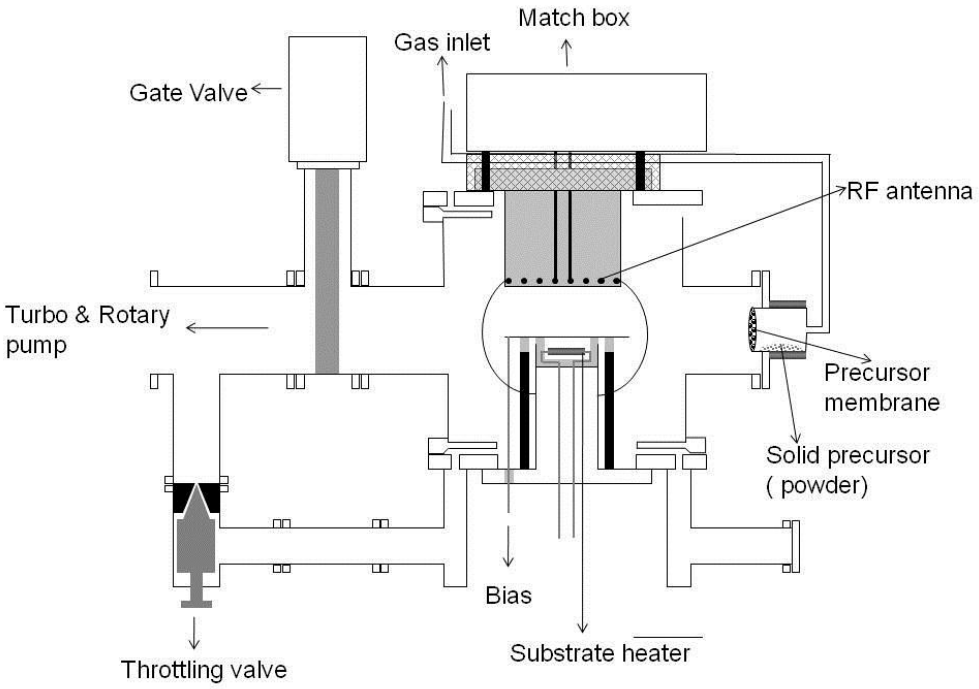


***Figure 4: A schematic diagram of ICP-CVD used for CNWs deposition***

***Figure 5: A picture of ICP CVD***

## 3.1.4. Additional attachment for metal organic precursor intake

An additional attachment to this reactor was required to introduce a metal organic precursor inside the plasma. A stainless steel- ceramic tube of diameter (~ 5 cm) was attached to a window of the reactor chamber. One side of this tube was covered with a

membrane of steel (hole size ~ 0.02 mm) and on the other side, the solid precursor has been fed into this tube. Argon gas is passed through this tube to the chamber.

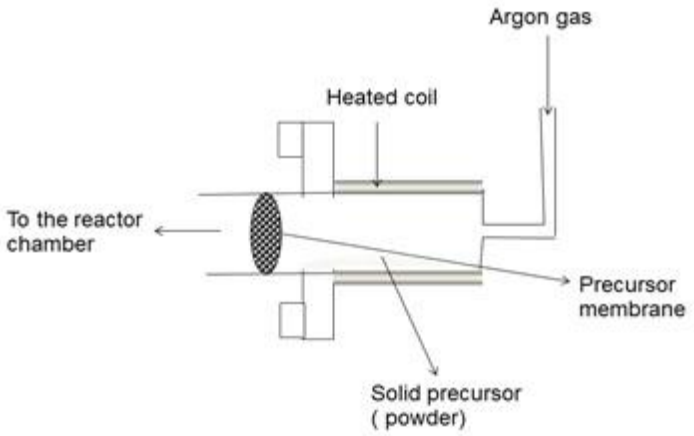


***Figure 6: A schematic diagram of the additional attachment for aluminium acetylacetonate intake***

The inlet of the precursor together with the argon gas was set in the center of substrate holder and in the middle point in the reactor chamber so that the uniformity of film is not affected. The precursor tube and the gas line were heated up to a temperature of 140$^{o}$C and this was maintained beginning 30 min before starting the deposition temperature, and 30 min before starting deposition so that the vapor pressure of precursor can flow with the argon gas uniformly inside the chamber.

## 3.1.5.Substrate preparation

In this work, silicon substrates (with a silicon dioxide layer) and stainless steel substrates were used. To ensure the quality and uniformity of CNWs deposition, substrates were thoroughly cleaned to remove all contaminants such as absorbed molecules, particulates and organic impurities. These contaminants may give rise to poor adhesion, bad uniformity and can degrade the device performance. The wafer was soaked in methanol for 10 minutes with ultrasonic bathing. This step removed the organic residues on the substrate. As methanol can also leave its own residues on the substrate, an iso propanol (IPA) immersion for another 10 minutes is required with ultrasonic bathing. The wafer of silicon and the steel substrates were then dried by nitrogen gas.

## 3.1.6.Growth conditions

Before starting the deposition, a clean substrate is placed on the substrate holder. More than one substrate can also be placed on the holder. The chamber is closed and pumped by a rotary pump followed by a molecular pump till it reaches $10^{-6}$ mbar. At the precursor tube, the heating is started up to 140$^{o}$C and the substrate can also be heated as required. The machine is designed to heat the substrate up to 900$^{o}$C substrate temperature.

All depositions are carried out at $10^{-2}$ mbar pressure. By varying the argon gas flux, the pressure can be fixed to $10^{-2}$mbar by adjusting gas intake inside the chamber controlled by mass flow controller (MFC). Plasma power is varied from 100W to 800W and argon gas flow rate is varied from 27 sccm up to 55 sccm. Deposition is carried out at all substrate temperatures from room temperature up to 800$^{o}$C. In case of deposition under oxygen plasma, oxygen is directly introduced into the reactor chamber. It does not pass through the precursor tube like the argon gas. The aluminium acetylacetonate (Al $(acac)_3$) precursor is sublimated in an evaporator at a constant temperature of 150$^{o}$C and then transported to the reaction chamber with an argon flow of 27 sccm. For this experiment, argon gas was fixed at 27 sccm and oxygen gas was varied from 20 sccm to 40 sccm. All deposition experiments were carried out at a pressure below $10^{-2}$ mbar. The films were deposited at different substrate temperatures between 500$^{o}$C and 800$^{o}$C and with varying pulsed DC biasing voltage from 10V to 100V at 3A current. Additionally, the plasma power was varied from 400 W to 800 W for some experiments.

# 3.2. Structured CNWs by laser

Microscopic field emission investigations suggest that high electric field enhancement occur at the conducting graphene layers. In spite, of their random growth, CNWs with high aspect ratio and sufficient electric conductivity might be useful for simple FE device in diode configuration especially when practical substrate material can be used. For gate control devices, however, either structured growth or post structuring of CNWs is required.

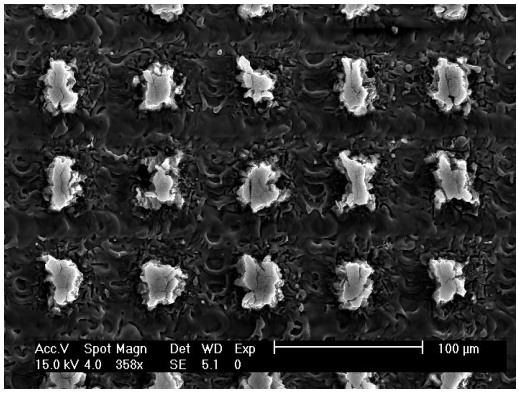


***Figure 7: SEM images of the laser-structured CNW patch array.***

Therefore, laser structured CNWs on steel and Si substrates are fabricated. This is explained in detail in chapter 5. After the deposition of CNWs (described above), these were then patterned with a diode-pumped solid-state laser (EdgeWave) using a galvano scanner (SCAN-LAB) and a theta objective (LINOS) for writing and focusing. The laser was operated at a wavelength of 532 nm, a pulse length of 10 ns and a pulse frequency of 50 kHz.

During patterning, the focused laser spot with a $1/e^2$ diameter of about 30 µm was moved across the sample surface at a writing speed of 30 cm/s. The average laser power was set to 1.15 W (Si) and 2.08 W (stainless steel), respectively. Quadratic grid patterns with a pitch of 60 µm were fabricated over an area of 5x5 $mm^2$. The resulting CNW patch arrays are shown in Figure 7 [115]. The detailed description of electron emission of laser structured CNWs is given in chapter 5.

# 3.3. Characterizations methods

## 3.3.1.Electron microscopy

An electron microscope is a type of microscope that produces an electronically-magnified image of a specimen for detailed observations. The electron microscope uses a particle beam of electrons to illuminate the specimen and create a magnified image of it. The microscope has a greater resolving power (magnification) than a light-powered optical microscope, because it uses electrons that have wavelengths about 100,000 times shorter than visible light (photons), and can achieve magnifications of up to 1,000,000x, whereas light microscopes are limited to 1000x magnification. The electron microscope uses

electrostatic and electromagnetic "lenses" to control the electron beam and focuses it to form an image. Electron microscopes are used to observe a wide range of biological and inorganic specimens including microorganisms, cells, large molecules, biopsy samples, metals, and crystals. Industrially, the electron microscope is primarily used for quality control and failure analysis in semiconductor device fabrication [101].

#### 3.3.1.1. Scanning electron microscope

The scanning electron microscope (SEM) is used to study the surface of materials rather than their internal arrangement. This instrument differs from all other conventional microscopes, using light or electrons, in forming its image progressively and not all at once. Electro-optically, the SEM has little in common with the TEM, apart from the use of an electron gun and a condenser lens system to produce a focused electron beam. These two/three lenses are the only in the column and after the specimen, there is an electron collector. As illustrated in Figure 13 , a very fine beam of electrons (energies up to 30 keV) is focused at the surface of the specimen in the microscope. The beam scans across it in a pattern of parallel lines. A number of phenomena occur at the surface under electron impact. The intensity of emission of both secondary and backscattered electrons is very sensitive to the angle at which the electron beam strikes the surface. For scanning electron microscopy, the emission of secondary electrons with energies of a few tens of eV is very essential. Equally important is the remission or reflection of high-energy backscattered electrons from the primary beam. The emitted electron current is accumulated and amplified. A standard instrument can usually reach a resolution of less than 10 nm. Scanning electron microscopy is performed to analyze the microstructures in plain view. A Philips XL 30 microscope equipped with a field emission gun (FEG) operating at an acceleration voltage between 3 and 5 kV, a working distance of typically 10 mm, and secondary electron image mode was used.The carbon nanowalls films were characterized by using scanning electron microscope for studying morphology and structure of films.

### 3.3.1.2. Transmission electron microscope

The transmission electron microscope (TEM) is a light microscope, in which a short wavelength electron illumination is used [101]. The main difference between a light microscope and a TEM microscopy is the electron lenses which are used in the TEM. The rest of it has exactly the same lens arrangement as its light counterpart (Figure 8) . It has been developed further to make use of the special properties of electron illumination like the higher resolution, but also the ability to carry out various forms of elemental and crystallographic micro analysis. The simplest electron microscope has two image-forming lenses and is an exact analogy of the compound light microscope.

The illumination coming from an electron gun is concentrated on the specimen by a condenser lens. After passing through the specimen, the electrons are focused by the objective lens into a magnified intermediate image. This image is further enlarged by a projector lens and the final image is formed on a fluorescent screen (photographic film or a CCD (charge-coupled device) camera). Nowadays, TEMs can reach atomic resolution using voltages of 200 kV and higher. The inner morphology of the tubular carbon structures discussed in this thesis and their strutural morphology were imaged by such a high-resolution TEM .

A typical SEM and TEM image of the CNWs fabricated by ICP-CVD are shown in Figure 9. CNWs stand vertically as supported by a network structure. The density and height of CNWs depend on the deposition time. When the deposited time is more than three hours, film starts peeling from the substrate. It clearly shows that a CNW sheet is a graphite flake with some disorder and defects.

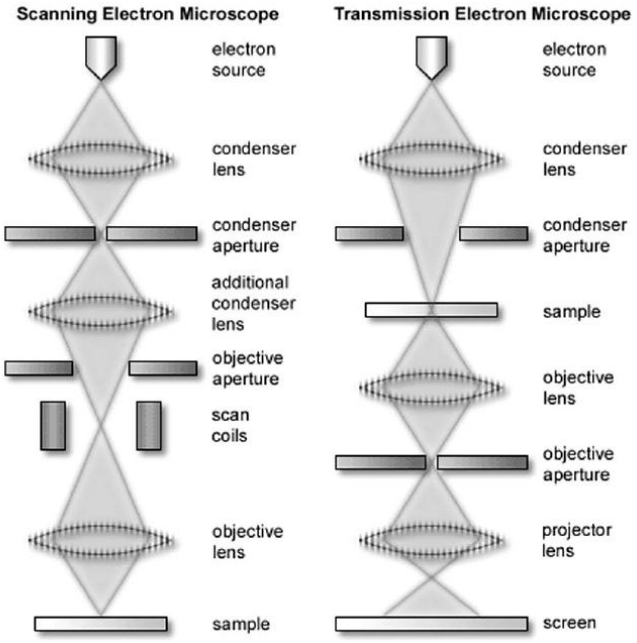


***Figure 8: Electron path in a scanning and transmission electron microscope***

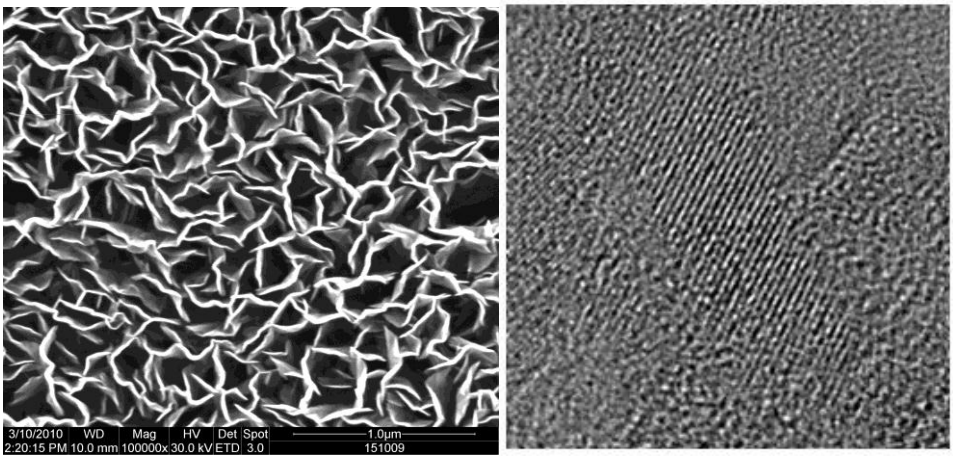


***Figure 9: SEM image of carbon nano walls deposited by ICP-CVD, TEM image shows the nano graphitic line [102]***

# 3.3.2.Spectroscopy

The study of interaction of electromagnetic radiation with matter is studied by spectroscopy. Spectroscopy can be classified according to different types of electromagnetic radiations interacting with matter. Spectroscopy is the most powerful tool for the study of atomic and molecular structures. In general, an excitation source such as

X-rays, electrons or synchrotron radiation will eject an electron from an inner-shell orbital of an atom. Detection of ejected photoelectron by X-rays is called X-ray photoelectron spectroscopy (XPS) or electron spectroscopy for chemical analysis. Detection of ejected electrons from higher orbitals to conserve energy during electron transitions is called auger electron spectroscopy.

Spectroscopic studies are designed so that the radiated energy interacts with specific types of matter and are carried out under the following two heads:

**Atomic spectrocopy:-** This spectroscopy is concerned with the interaction of electromagnetic radiation with atoms, which are commonly in their lowest energy state, called ground state.

**Molecular spectroscopy:-** This spectroscopy deals with interaction of electromagnetic radiation with molecules. This results in transition between rotational and vibrational energy levels in addition to electronic transitions.

Other types of spectroscopy are distinguished by specific applications or implementations.

## 3.3.3.Raman spectroscopy

Raman Spectroscopy is a spectroscopy technique based on inelastic scattering of monochromatic light (laser). Inelastic scattering is nothing but the frequency of photons in monochromatic light is changed by interaction with the sample. The sample absorbs the photons of the laser light and re-emits it. In comparison to the original laser light frequency the reemitted frequency changes (shifted up or down) which is basically called the Raman Effect. This change or shift provides information about transitions in molecules i.e. vibrational or rotational ones. Raman scattering is an optical process involving the simultaneous emission or absorption of a phonon associated with the scattering of a photon.

### 3.3.3.1. Discovery of Raman effect

The Raman effect is an alternative and simple method other than band spectra for obtaining vibrational and rotational frequencies of molecules. A valuable adjunct to

electronic and infrared spectra is the Raman effect, discovered by Sir Chandrasekhara Venkata Raman (1928) [103]. According to Raman, if any substance, gaseous liquid or solid is exposed to radiation of definite frequency, then the light scattered at right angles contains frequencies different from the incident radiation, and carries the characteristics of the substance which is under examination.

Suppose $\nu_i$ and $\nu_s$ are the frequency of incident and scattered light, respectively, then the difference $\Delta\nu = \nu_i - \nu_s$ is known as Raman frequency. When the scatter of light is observed with the help of a spectrophotometer, it is found that spectrum is made of lines of the incident light together with a series of lines on either side of them. This series of lines in the scattering of light is known as Raman spectra. In the spectra of scattered radiation, the Raman lines appear in the spectrum on either side of the line of incident radiation, with higher as well as lower frequencies. The Raman lines on the lower frequency side are called stokes lines, i.e. where $\nu_i > \nu_s$ and on the higher frequency sides are termed anti stokes lines, i.e when $\nu_s > \nu_i$ [101].

# 3.3.3.2. Explanation of light scattering by molecules

The scattering of light by molecules can be explained by making use of the electromagnetic theory. The incident light wave represented by an electric field E induces a dipole moment in the molecules. The induced moment P given by $P = \alpha E$ where $\alpha$ is the polarisability of the molecule. The theory of Raman effect of scattering largely depends upon this factor. Raman also regarded that in Rayleigh's scattering no frequency change was caused, but only some of the already existing frequencies were selected, whereas in Raman effect new lines of different frequencies appeared even when a single frequency was scattered [104].

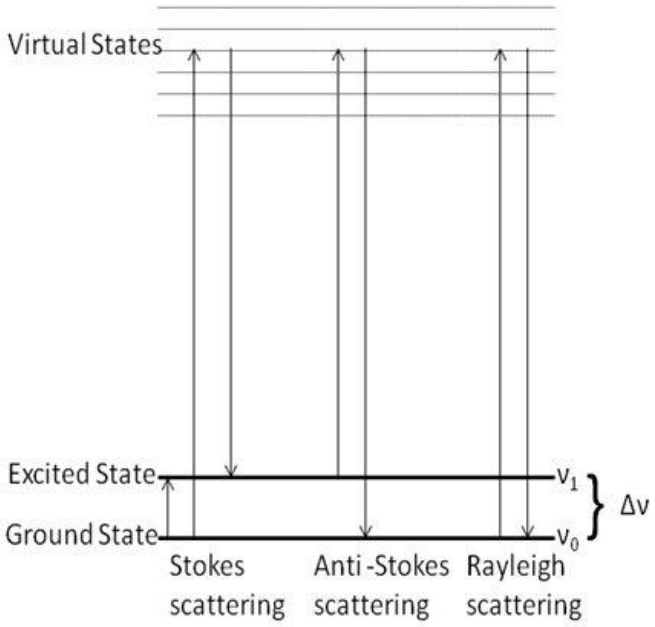


***Figure 10: Energy levels in Raman scattering***

Atoms and molecules which are polarised in an electric filed re-emit radiations, if the field is varied periodically. If the variation in distances between atoms in the scattered molecules are negligible, then the frequency of incident and scattered radiations will be the same and the scattering will be Rayleigh's scattering.

Figure 11 shows the transitions are possible between the vibrational levels in a polyatomic molecule. Raman scattering results from an interaction between the incident photons and the vibrational energy levels of the molecules. The interaction is the transfer of a portion of the energy of the photon to the molecule or vice versa. Thus $\nu_R = \nu_i \pm \Delta\nu$ where subscript ($_R$) represents the Raman radiation, ($_i$) the incident radiation and $\Delta\nu$ the Raman shift. The dashed lines in Figure 11 indicate unstable virtual energy levels. In Stokes transition, the energy is taken from the incident radiation by the sample, and hence most intense Raman lines are obtained. Under these conditions $\nu_R = \nu_i - \Delta\nu$, if a significant number of molecules are already in the $\nu_i$ state, and Stokes lines can be obtained when $\nu_R = \nu_i + \Delta\nu$ Hence,While considering laws of absorption, it has been assumed that not transmitted light must be absorbed, provided the medium does not contain any foreign particle which would scatter the radiation. In fact, there is always some scattering, but the effect is very small when it occurs at the molecule level. This molecule or Rayleigh scattering takes place without any change in wavelength, although

the amount of scatterings depends on wavelength. The blue colour of the sky is due to Rayleigh scattering.

Scattering with a change of wavelength can also occur and is called Raman scattering. Rayleigh and Raman scattering arise from the same type of interaction between the radiation and the molecule. This interaction induces an oscillating dipole moment in the molecule, which is proportional to the electric field. The proportionality constant is called the polarisation of the molecule.

The main difference in Rayleigh scattering and Raman effect is that in Rayleigh scattering, the molecule has not yet gained or lost energy and there is no difference in wavelength between incident and scattering radiation. Although scattering takes place in all directions, in Raman effect, the molecule may not return to its original energy state, but may not lose or gain energy so that emitted radiation has a different wavelength.

If the molecule is originally in the ground state and drops back to an excited vibrational state, the scattered radiation will have a longer wavelength, and the shift corresponds to the vibration energy of the excited state. These Raman lines are called Stokes lines. Similar phenomenon will happen when the molecule is originally in the excited state and falls back to the ground state. At room temperature most of the molecules will be in the ground state, the Stokes lines will be of higher intensity than the anti-Stokes lines.

# 3.3.3.3. Raman spectra observation in CNWs

Raman spectroscopy is a fast and non-destructive method for the characterization of carbon materials. All carbons show common features in their Raman spectra in the 800–2000 $cm^{-1}$ region, the so-called *G* and *D* peaks, which lie at around 1560 and 1360 $cm^{-1}$ respectively for visible excitation [105-109]. The *T* peak at around 1060 $cm^{-1}$ is only seen for UV excitation [105-109]. The *G* peak is due to the bond stretching of all pairs of $sp^2$ atoms in both rings and chains. The *D* peak is due to the breathing modes of $sp^2$ atoms in rings **[**105,110-113]. The *T* peak is due to the C-C $sp^3$ vibrations. Raman spectra can be used to distinguish the different types of amorphous carbons and to derive their structural and mechanical properties. The Raman spectra are dominated by the $sp^2$ sites. Thus, the clustering and disorder of the $sp^2$ phase is the main factor affecting peak positions, width,

and intensity. In principle, the $sp^2$ clustering can vary independently of the $sp^3$ content. The other two key Raman parameters to monitor carbon bonding are the intensity ratio of the *D* and *G* peaks, $I_D/ I_G$, and the full width at half maximum of the *G* peak, FWHM/*G*. In amorphous carbons $I_D/ I_G$ is a measure of the size of the $sp^2$ phase organized in a ring [105].

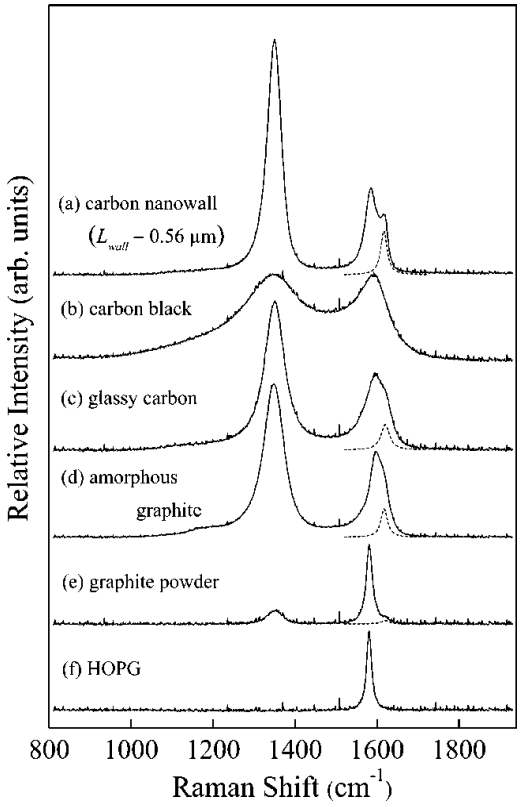


***Figure 11: Raman spectra of the carbon nanowalls, graphite like carbons, graphite powder, amorphous graphite, glassy carbon, amorphous carbon. Dashed lines represent a Lorentzian fit to a D' band*** *(Fig Ref to [114])*

If $I_D/ I_G$ is negligible, then the $sp^2$ phase is mainly organized in chains, or even if rings are present, the bonds are not fully delocalized on the rings. Raman spectroscopic measurements for the carbon nanowalls deposited by ICP-CVD using metal organic precursor were carried out using an Ar laser operating at 514.5 nm. Spectra exhibited *G* and *D* bands at 1580 cm$^{-1}$ and 1350 cm$^{-1}$, respectively. It is found that the bandwidth of the *G* band is relatively narrow, even when the peak intensity ratio of *D* band to *G* band is significantly high. These spectral features of CNWs are distinguished from those of typical graphite-like carbons reported so far. From the comparison of these spectral features, it is shown that CNWs are composed of small crystallites with a high degree of

graphitization. The Raman spectra of carbon nanowalls are discussed thoroughly in this thesis (chapter 4).

## 3.3.4.X-Ray photon spectroscopy

X-Ray photon spectroscopy is a quantitative spectroscopic technique which gives information about the elemental composition inside the sample. XPS spectra is obtained by bombardment of X-rays on the sample and simultaneously measuring the kinetic energy and number of electrons that are escaping the surface of the sample.

XPS was developed in the mid 1960s by K. Siegbahn and his research group. K. Siegbahn was awarded the Nobel prize for physics in 1981 for his work in XPS. The phenomenon is based on the photoelectric effect outlined by Einstein in 1905 where the concept of the photon was used to describe the ejection of electrons from a surface when photons impinge upon it.

For XPS, Al K alpha (1486.6eV) or Mg K alpha (1253.6eV) are the photon energies of choice. Other X-ray lines can also be chosen such as Ti K alpha (2040eV). The XPS technique is highly surface specific due to the short range of the photoelectrons that are excited from the solid. The binding energy of the peaks are characteristic of each element. The peak areas can be used (with appropriate sensitivity factors) to determine the composition of the surface of the material. The shape of each peak and the binding energy can be slightly altered by the chemical state of the emitting atom. Hence, XPS can provide chemical bonding information as well. XPS is not sensitive to hydrogen or helium, but can detect all other elements.

**Physical Principles**

Photoelectron spectroscopy is based upon a single photon in an electron out process and from many view points this underlying process is a much simpler phenomenon than the Auger process. The energy of a photon of all types of electromagnetic radiation is given by the Einstein relation, $E= h \nu$ where h- Planck constant and $\nu$ is the frequency of the radiation : [101]

Photoelectron spectroscopy uses monochromatic sources of radiation (i.e. photons of fixed energy).

In XPS, the photon is absorbed by an atom in a molecule or solid, leading to ionization and the emission of a core (inner shell) electron. By contrast, in UPS the photon interacts with valence levels of the molecule or solid, leading to ionisation by removal of one of these valence electrons.

The kinetic energy distribution of the emitted photoelectrons (i.e. the number of emitted photoelectrons as a function of their kinetic energy) can be measured using any appropriate electron energy analysor and a photoelectron spectrum can thus be recorded. The process of photo ionization can be considered in several ways. One way is to look at the overall process as follows: $A + h\nu \rightarrow A^+ + e^-$

Conservation of energy then requires that:

$E(A) + h\nu = E(A^+) + E(e^-)$

.

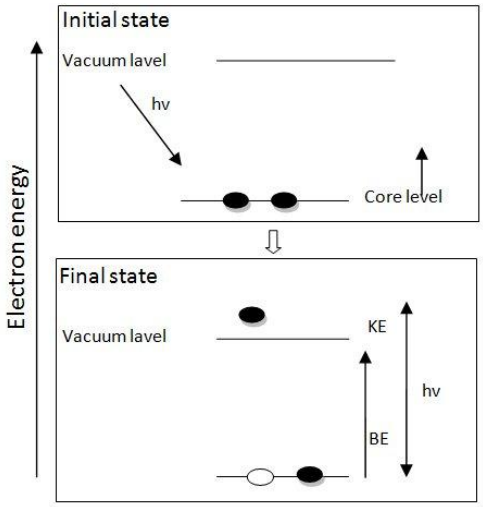


***Figure 12: Photo ionization- Principle of photon spectroscopy***

Since the electron's energy is present solely as kinetic energy (KE) this can be rearranged to give the following expression for the KE of the photoelectron:

$KE = h\nu - ( E(A+) - E(A) )$

The final term in brackets, representing the difference in energy between the ionized and neutral atoms, is generally called the binding energy (BE) of the electron. This then leads to the commonly quoted equation, $KE = h\nu - BE$

An alternative approach is to consider a one-electron model along the lines of the following pictorial representation; this model of the process has the benefit of simplicity but it can be rather misleading.

The BE is now taken to be a direct measure of the energy required to just remove the electron concerned from its initial level to the vacuum level and the KE of the photoelectron is again given by:

$KE = h\nu - BE$

It should be noted that the binding energies (BE) of energy levels in solids are conventionally measured with respect to the Fermi-level of the solid, rather than the vacuum level. This involves a small correction to the equation given above in order to account for the work function ($\varphi$) of the solid, but for the purposes of the discussion below this correction will be neglected.

## 3.3.5.Energy dispersive X-ray spectroscopy

Energy-dispersive X-ray spectroscopy (EDS or EDX) is an analytical technique used for the elemental analysis. It is one of the variants of X- ray fluorescence spectroscopy that relies on the investigation of a sample through interactions between electromagnetic radiation and matter, analysing X-ray emitted by the matter in response to being hit with charged particles. Its characterization capabilities are due in large part to the fundamental principle that each element has a unique atomic structure allowing X-rays that are characteristic of an element's atomic structure to be identified uniquely from one another. To stimulate the emission of characteristic X-rays from a specimen, a high-energy beam of charged particles such as electrons or photons, or a beam of X-rays, is focused into the sample being studied. At rest, an atom within the sample contains ground state (or unexcited) electrons in discrete energy levels or electron shells bound to the nucleus. The incident beam may excite an electron in an inner shell, ejecting it from the shell while creating an electron hole where the electron was. An electron from an outer, higher-

energy shell then fills the hole, and the difference in energy between the higher-energy shell and the lower energy may release in the form of an X-ray. The number and energy of the X-rays emitted from a specimen can be measured by an energy-dispersive spectrometer. As the energy of the X-rays is characteristic of the difference in energy between the two shells, and of the atomic structure of the element from which they are emitted, this allows the elemental composition of the specimen to be measured.

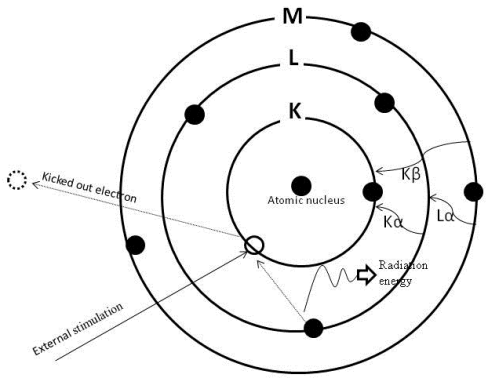


***Figure 13: Principle of EDX***

**Accuracy of EDX**

The accuracy of an EDS spectrum can be affected by many factors. Windows in front of the detector can absorb low-energy X-rays (i.e. EDS detectors cannot detect elements with atomic number less than 4, that is H, He, and Li) [98]. Over-voltage settings in EDS alter the peak sizes raising over-voltage on the SEM shifts the spectrum to larger energies, making higher-energy peaks larger and lower-energy peaks smaller. Some elements will have overlapping peaks (e.g., Ti Kβ and V Kα, Mn Kβ and Fe Kα).[98] The accuracy of the spectrum can also be affected by the nature of the sample. X-rays can be generated by any atom in the sample which has been sufficiently excited by the incoming beam. These X-rays are emitted in any direction, and so they may not all escape the sample. The likelihood of an X-ray escaping the specimen, and thus being available to detect and measure depends on the energy of the X-ray and the amount and density of material it has to pass through. This can result in reduced accuracy in homogeneous and rough samples.

## 3.3.6.Secondary Ion Mass spectroscopy

Principle of the secondary ion mass spectroscopy (SIMS) is based on interaction of the primary ion beam with the sample (under vacuum). This interaction provides sufficient energy to ionize many elements.

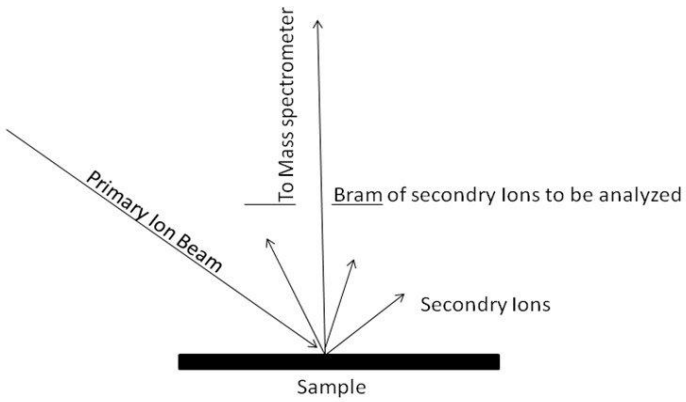


***Figure 14: Principle of SIMS***

If the primary beam is composed of positively charged ions, the resultant ionization favors production of negative ions; primary beams of negative ions favor generation of positive ions. Although most atoms and molecules removed from the sample by the interaction of the primary beam and the sample surface (referred to as sputtering) are neutral, a percentage of these are ionized. These ions are then accelerated, focused, and analyzed by a mass spectrometer.

SIMS instruments use an internally generated beam of either positive or negative ions (primary beam) focused on a sample surface to generate ions that are then transferred into a mass spectrometer across a high electrostatic potential, and are referred to as secondary ions.

## 3.3.7.X-Ray Diffraction Methods

With the help of X-rays, it is now possible to determine the special arrangement of the structural units of a substance in the crystalline state and hence X-rays can be employed in investigating the interior of a crystal. The most important feature of the crystals of a

substance is that the interfacial angles remain constant although the shapes and sizes of individual crystals differ considerably. Making use of this fact, Havy (1784) suggested that crystals are built up of small units having the same interfacial angles as the crystal. The distance between the atoms in crystals have been found to be roughly equal to $10^{-8}$ cm. So optical and elctronic microscopy cannot be used in this field. It was suggested by Von Laue (1912) that it might be possible to direct X-ray on crystals because:

- The crystals act as a three dimensional natural grating for X-Rays.
- X- rays act as part of the electromagnetic radiation.
- X-ray are actually the radiation of very small wavelength probably of the order of $10^{-4}$cm

Since its discovery in 1912 by Von Laue [115] X-ray diffraction has provided a wealth of important information to science and industry. For example, much of the spacing of atoms in crystalline material has been directly deduced from diffraction studies. These studies proved to be of immense importance in understanding the physical properties of metals, polymeric materials and other solids.

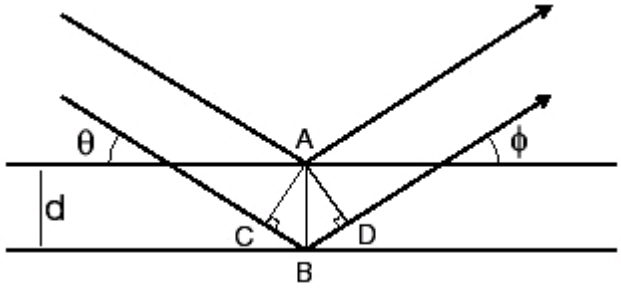


***Figure 15: Diffraction of X- rays by crystals***

X-ray diffraction provides a convenient and practical means for the qualitative identification of crystalline compounds. This application is based on the fact that the X-ray diffraction pattern is unique for each crystalline substance and so chemical identity cannot be assumed. Qualitative identification of structures can be made by comparison of the interplanar spacing values of the specimen pattern with an index of standard patterns.

**Braggs Law**

When electrons moving at high speeds are directed to a metal target, a small percentage of their kinetic energy is converted into X-rays. The X -rays emitted by the target consist of a continuous range of wavelength in the continuous spectrum that is inversely proportional to the applied voltage which accelerates the elctrons towards the target.

When a beam of X-rays is allowed to fall on a crystal surface at some angle θ, each atom acts as a source. The scattered radiation is of the same wavelength. Thus when an X-ray beam strikes a crystal surface at an angle θ, a portion is scattered by the layer of atoms at the surface and unscattered portion of the beam, penetrates to the second layer of atoms where again a fraction is scattered and the remaining passes on to the third layer. Bragg [116] developed a useful relation between the wavelength of the X-ray and the spacing between the lattice planes.

As the atomic in a crystal are orderly arranged, a beam of X-rays is reflected from a plane of atoms similar to the reflection of light from a plane mirror.

The most important requirement of diffraction are:

- The spacing between layers of atoms must be roughly the same as the wavelength of the radiation.
- The scattering centers must be spatially distributed in a highly regular way.

Bragg treated the diffraction of X-ray by crystals as shown in the Figure 15 . Considering a beam of monochromatic X-rays, which strikes on a set of parallel and equidistant planes called lattice or Braggs planes in the crystal structure at an angle θ, scattering occurs as a result of interaction of the radiation with atoms located at A and B. If the distance CB + BD = nλ, where n is an integer 1,2,3 etc, known as the order of reflection, the scattering radiation will be in phase AD, and the crystal will appear to reflect the X- radiation.

$CB + BD = 2d \sin \theta$

where d is the interplanar distance of the crystal. Thus the conditions for constructive interference on the beam at an angle θ are,

$n\lambda = 2d \sin \theta$

This equation is known as Braggs's equation. Since sin θ can not exceed unity, the minimum spacing for which the reflection can be observed is $d = \lambda/2$. Thus X-rays appear to be reflected from the crystal only if the angle of incident satisfies the condtion that sin $\theta = n\lambda / 2d$ at all other angles destructive interference occurs.

# Summary

In this chapter, we summarized the fabrication and characterization techniques used for CNWs sample preparation. Briefly, the method of structuring of CNWs by laser and measurement of electron emission is explained in this chapter. From the next chapter, we will start to discuss the physics of CNWs, which includes characterizations of CNWs and the application in electric field emission properties.

# References


96. Denneman J W "Determination of electromagnetic properties of low pressure electrodeless inductive discharge" Journal of Physics D: Applied Physics 23 : 1999 , 293
97. Amorim J, Maciel H S and Sudano , "High density plasma mode of an inductively coupled radio frequency discharge" Journal of Vacuum Science and Technology B 9: 1991, 362
98. MacKinnon K A, "On the origin of electrode less discharge" Phil. Mag. 8 1929 605
99. Hopwood J, "Review of inductively coupled plasmas for plasma processing" Plasma Sources Science and Technology 1: 1992,109
100. Cohen SA: "An Introduction to Plasma Physics for Materials Processing", in Plasma Etching- an Introduction, edited by D.M. Manos and D.L. Flamm, Academic Press, Inc., Boston/San Diego/NewYork, 215
101. Watt I M, "The principles and practice of electron microscopy", second edition 1997, published by Press Syndicate of University of Cambridge.
102. Jain H.G, Karacuban H, Krix D,Becker H-W, Nienhaus H, Buck V, "Carbon nanowalls deposited by inductively coupled plasma enhanced chemical vapor deposition using aluminium acetylacetonate as precursor", Carbon 49: 2011, 4987-4995.
103. Sir CV Raman. The New Physics (Talks on the Aspects of Science), New York: Philosophical Library, 1951
104. Ferrari AC, Robertson J "Raman Spectroscopy in Carbons: from nanotubes to Diamond "Philosophical Transactions of Royal Society A, London, 362 : 2004, 2267
105. Ferrari AC and Robertson J "Interpretations of Raman spectra of disordered and amorphous carbon" Physical Review B 61: 2000, 14095
106. Piscanec S, Mauri F, Ferrari AC, Lazzeri M, Robertson J, "Ab initio resonant Raman spectra of diamond-like carbons" Diamond and Related Materials 14: 2005, 1078
107. Gilkes K W R, S. Prawer, K. W. Nugent, J. Robertson, H. S.Sands, Y. Lifshitz, and X. Shi, "Direct quantitative detection of the sp3 bonding in diamond-like carbon

films using ultraviolet and visible Raman spectroscopy" Journal of Applied Physics 87: 2000, 7283

108. Merkulov V I, Lannin J S, Munro CH, Asher SA, Veerasamy VS, Milne WI, "UV Studies of Tetrahedral Bonding in Diamond like Amorphous Carbon" Physical Review Letters 78: 1997, 4869

109. Tuinstra F Koenig J L "Raman Spectrum of Graphite" Journal of Chemical Physics 53: 1970, 1126

110. Castiglioni C, Donato ED, Tommasini M, Negri F, Zerbi G, "Multi-wavelength Raman response of disordered graphite materials: models and simulations" Synthesis of Metals 139: 2003, 885

111. Piscanec S, Lazzeri M, Mauri F, Ferrari AC, Robertson J, "Kohn Anomalies and Electron-Phonon Interactions in Graphite" Physical Review Letters 93: 2004, 185503

112. Mapelli C, Castiglioni C, Zerbi G, Mullen K "Common force field for graphite and polycyclic aromatic hydrocarbons" Physical Review B 60: 2000, 12710

113. Kurita S, Yoshimura A, Kawamoto H, Uchida T, Kojima K, Tachibana M, "Raman spectra of carbon nanowalls grown by plasma-enhanced chemical vapor deposition" Journal of Applied Physics 97 2005, 104320-5

114. Casiraghi C, Ferrari A C, Robertson J "Raman spectroscopy of hydrogenated amorphous carbons" Physical Review B 72 :2005, 085401

115. Laue von M (1914). "Concerning the detection of x-ray interferences". Nobel Lectures, Physics 1901–1921. Retrieved 2009-02-18

116. Bragg WH (1908). "The nature of γ- and X-rays". Nature 77:1915: 270

# 4. Physics of CNWs

The chapter discusses the results of the characterized CNW films. SEM and Raman studies show that CNWs are graphitic nanostructures with the edges comprised of stacked planar graphene sheets standing vertically on a substrate. TEM will discuss that the sheets form a wall structure with thickness in the range of a few nanometers to a few tens of nanometers, and with a high aspect ratio and have some crystalline patches of aluminium carbide inside the CNWs matrix. Furthermore, chemical analysis is discussed by secondary ion mass spectroscopy (SIMS), electron dispersive X-ray spectroscopy (EDX) and nuclear resonance analysis (NRA). The elemental composition is discussed by X-ray photon spectroscopy (XPS).

## 4.1. Surface morphology

### 4.1.1.SEM observations

SEM images of typically CNWs films are shown in Figure 16. The films were grown by inductively coupled plasma enhanced chemical vapor deposition by using a metal organic precursor as a source of carbon and aluminium.

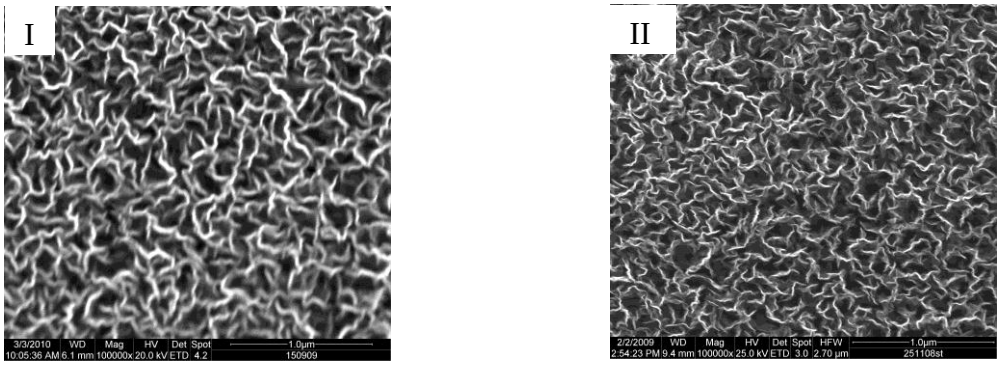


***Figure 16: Typical SEM image of CNWs films grown by fixing 800 W power and 665$^{o}$C substrate temperature I) 45 sccm Ar gas flow, II) 50 sccm argon gas flow***

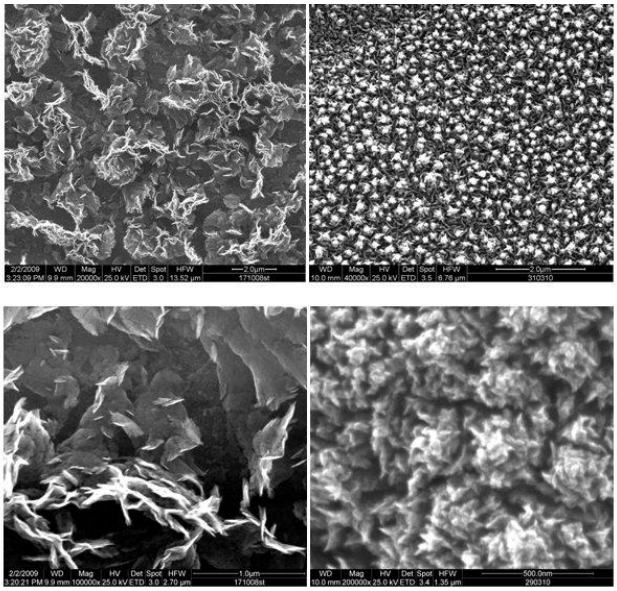

***Figure 17: SEM image of CNWs with different morphologies deposited by inductively coupled plasma enhanced CVD***

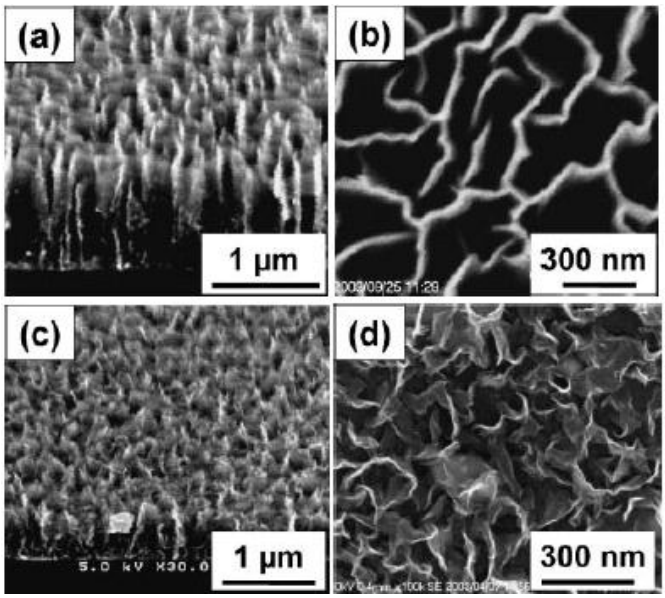


***Figure 18: Typical SEM images of CNW film (a) Side view and (b) top view of CNW film grown using $C_2F_6/H_2$ system for 8h (c) Side view and (b) top view of CNW film grown using $CH_4/H_2$ system for 8h Deposited by electron beam excited plasma*** *(Fig adopted from Ref [112])*

These images indicate the vertical growth of the two-dimensional carbon sheets on the substrates; the morphology and structure of CNW film depend on the source gases, pressure, process temperatures as well as the type of plasma used for the growth of

CNWs. Figure 17 shows the SEM image of different morphologies. In addition to the vertically standing maze-like structure, are aligned flower type structure, a highly branched type, and a porous type structure have been fabricated. The similar results are reported by using electron beam excited plasma enhanced chemical beam vapor deposition [117] which is shown in Figure 18 [118]. The morphology of CNWs films highly depends on the deposition parameters and the type of plasma being used for the coatings.

#### 4.1.1.1. Effect of substrate temperature on surface morphology

Temperature is a key parameter for carbon nanostructure synthesis. The temperature can be provided by an external source or by the plasma itself or by combining both. It is reported that a temperature above 500$^{o}$C is in demand for obtaining nanostructure materials [119,120]. Compared with CVD, where thermal activation is necessary to sustain the catalytic decomposition of the precursor, in case of plasma methods, the decomposition is performed by electron collision or excitation transfer. Thus, in the case of plasma methods, the precursor decomposition is performed by electron collision or excitation transfer. Hence, a lower thermal activation threshold for the growth is required. Several different methods have been used to grow CNWs at substrate temperature above 400$^{o}$C. Vertically aligned CNWs (thickness 10 to 30 nm, height 600 nm) are synthesized using capacitively coupled plasma enhanced CVD at 500$^{o}$C [121]. Low pressure RF PECVD [120], Helicon plasma enhanced CVD [123], Microwave plasma enhanced CVD [124], and HFCVD [125, 126] methods have succeeded to grow the CNWs at 400$^{o}$C-700$^{o}$C substrate temperatures. Lowering the substrate temperature is a requirement for nanostructure materials which are not compatible with high temperature, for example, growth on polymeric substrate or low melting point glasses in the semiconductor industry.

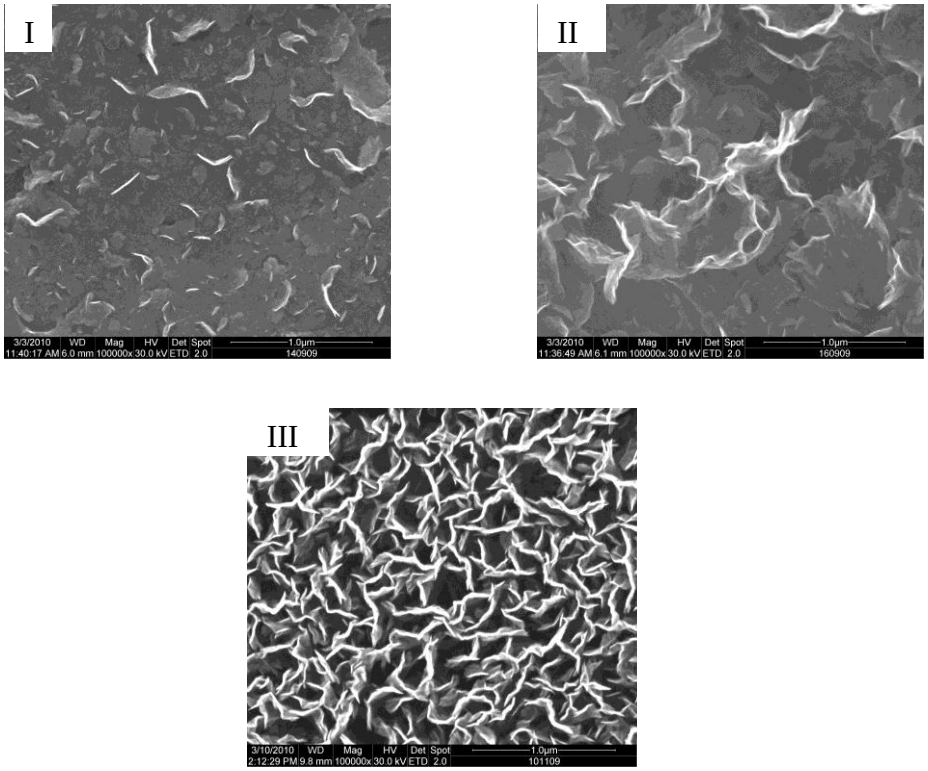


***Figure 19: SEM images of films deposited at various substrate temperature (I) 250$^{o}$C (II) 450$^{o}$C (III) 665$^{o}$C at fixed plasma power 500 W and 45 sccm argon gas flow***

The correlation of wall size with respect to argon flow and substrate temperature at fixed plasma power 500 W (Figure 19 ) and 800W (Figure 20) are shown. The number density of the walls increases with increasing the substrate temperature. However, variable plasma parameters are complex. Hence, the choice of reduced parameters is desirable for the study devoted to finding the correlation between the material properties and the plasma characteristics. Shimbukuro et al. [127] reported that substrate surface temperature is an important parameter in the preparation of CNWs by hot wire chemical vapor deposition. To find the effect of substrate temperature on surface morphology of CNWs, Ar gas is fixed at 45 sccm, plasma power is tuned between 500 W and 800 W, and varying the substrate temperature (Figure 19 and Figure 20). The higher temperature is required to obtain the smaller wall size.

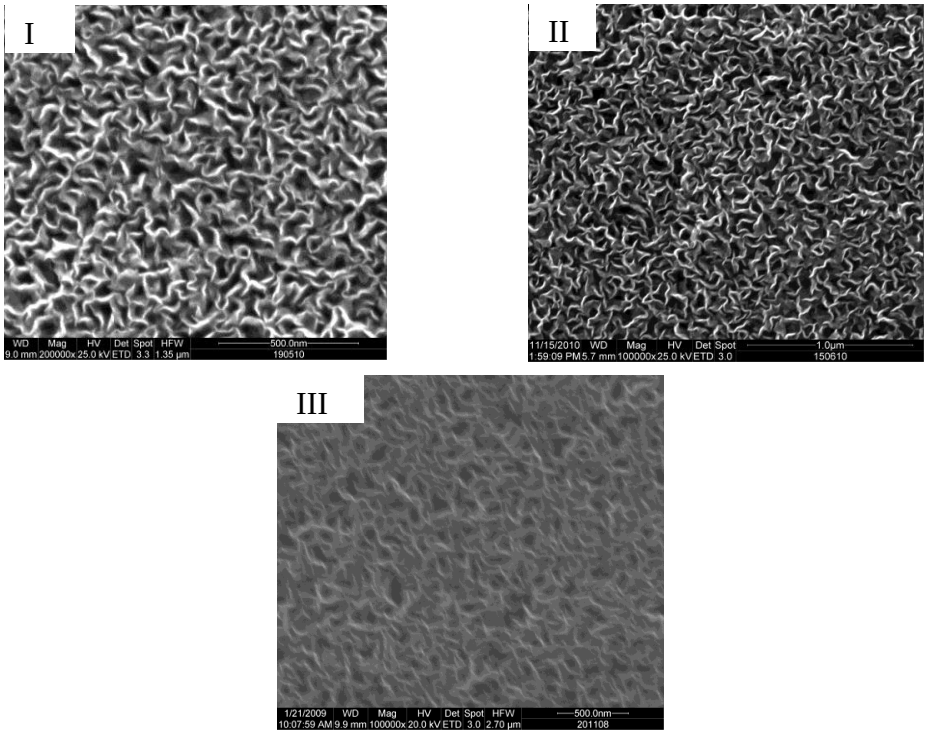


***Figure 20: SEM images of films deposited at various substrate temperature (I) 250$^{o}$ C (II) 450$^{o}$C (III) 665$^{o}$C at fixed 800W and 45 sccm argon gas flow***

It is also possible to deposit CNWs even at 250 $^{o}$C *(*Figure 20-*(I))* (this is the temperature where substrate is heated only by plasma not by additional substrate heater) on steel and silicon substrates (Figure 21). It is clear from the Figure 22 that the wall sizes of CNWs are influenced by varying the substrate temperature (decreases with increasing temperature). Hence, the minimum size of walls can be found at high temperature. However, in section, it is discussed that high flow rate of argon gas influences more than higher substrate temperature for producing smaller size of walls.

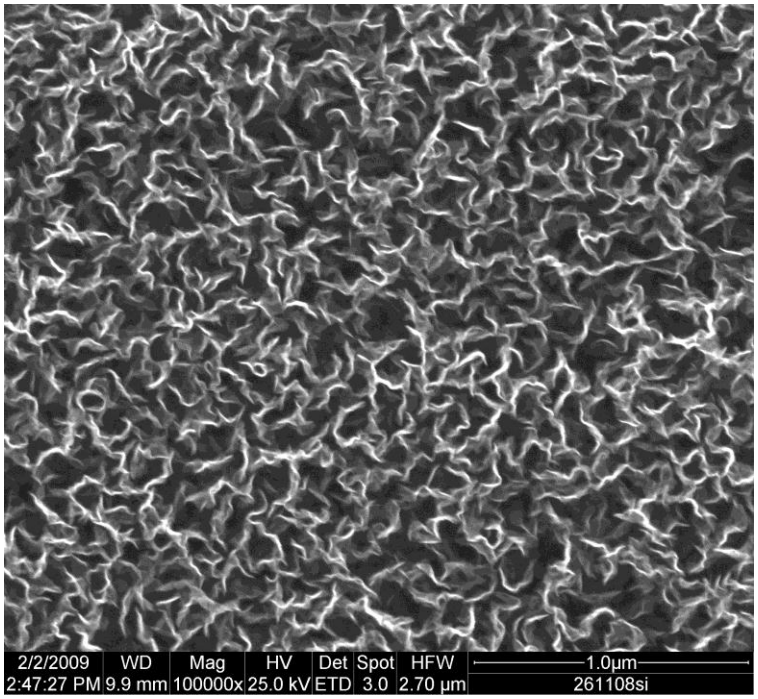


***Figure 21: CNWs film deposited on silicon substrate at plasma power 800 W, 665$^{o}$C substrate temperature***

Compared to MWPECVD and RF-PECVD, HFCVD is reported to be more suitable for smaller and thus denser nanowalls. [128] Using a $C_2H_2$-3%-15%- /$H_2$ mixture as source gases, in this temperature range, the size and density of the nanoflakes decreases and increases, respectively, as the temperature increases. At 700°C substrate temperature, the thickness and lateral size decrease to about 5 nm and 80 nm, respectively, and produce dense films.

In this study, it is seen that the walls size of CNW can be controlled by the substrate surface temperature. In the preparation at higher substrate temperature, the activation of surface reactions would also increase the nucleation density of CNWs. Then, the growth of CNWs with a large wall size may be prevented.

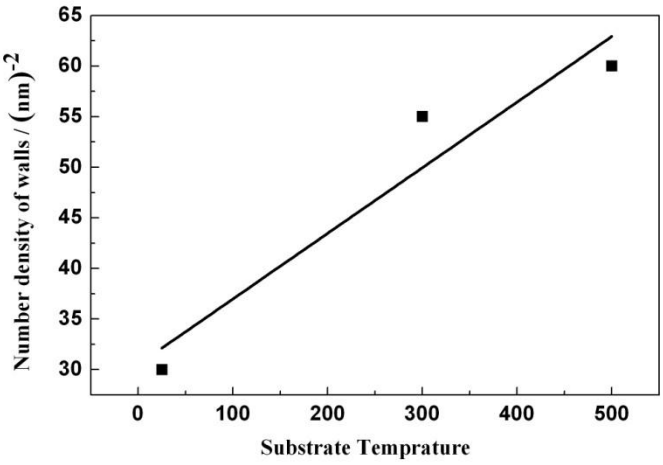


***Figure 22: Number density of walls with respect to substrate temperature***

## 4.1.1.2. Effect of argon gas flow on surface morphology

As shown in earlier sections that it is possible to deposit CNWs at low temperature. At 665$^{o}$C substrate temperature, the smallest wall sizes were found. In this section, the effect of Ar flow will be discussed. CNWs are synthesized by varying argon flow rate at constant substrate temperature of 665$^{o}$C. The effect of aluminium inclusion in the structures of CNWs is studied. In Figure 23, three samples from all deposited films were taken and named as film (a), film (b) and film (c). SEM microstructures show the variation in size of walls at various flow rates of argon gas. In Figure 23 (a), the most remarkable features of this structure are clearly defined boundaries and relatively constant thicknesses of the film. The wall size measured of this film is ~ 300 nm and number density of walls is ~ 35 (μm)$^{-2}$ which is plotted in Figure 24. As shown in Figure 23(b), when the flow is increased to 45 sccm, the wall size of film decreases to ~ 100 nm and the number density of walls is ~ 87 (μm)$^{-2}$. Similarly, in Figure 23(c), increasing argon gas flow to 55 sccm, reduces the wall size remarkably to 20 nm and increases the number density of walls to ~ 200 (μm)$^{-2}$.

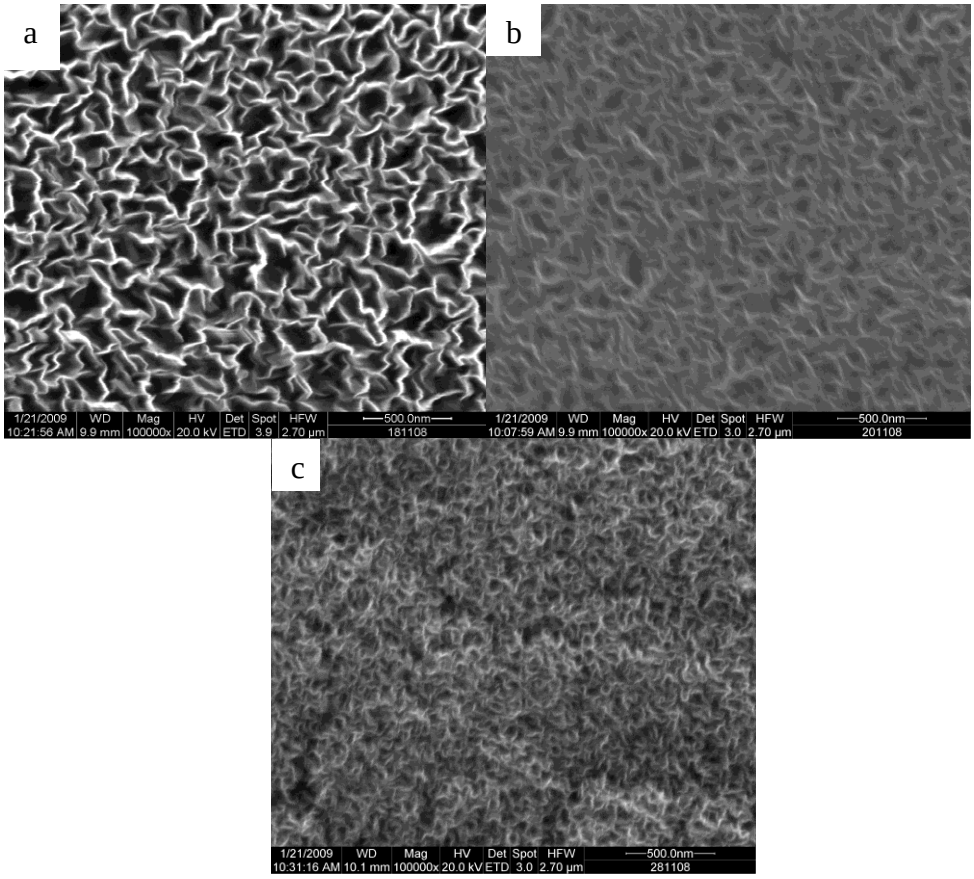


***Figure 23: Comparison of wall sizes at different argon gas flow at constant temperature 665 $^{o}$C. (a ) Ar 27 sccm (b) Ar 45 sccm (c) Ar 55 sccm, films deposited on steel substrate***

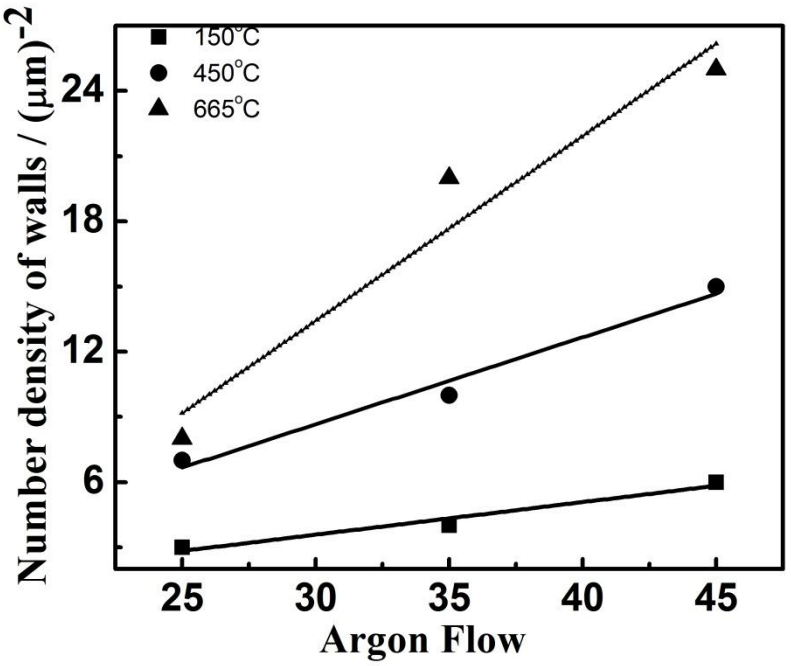


***Figure 24: Number density of walls with respect to argon gas fow. Films are deposited at different substrates temperatures and fixed 800 W***

Similarly at a fixed substrate temperature of 250 $^{o}$C, in Figure 25, films were deposited by varying flow rate of argon gas. The films deposited at higher flow rate of argon gas results in reduced wall sizes.

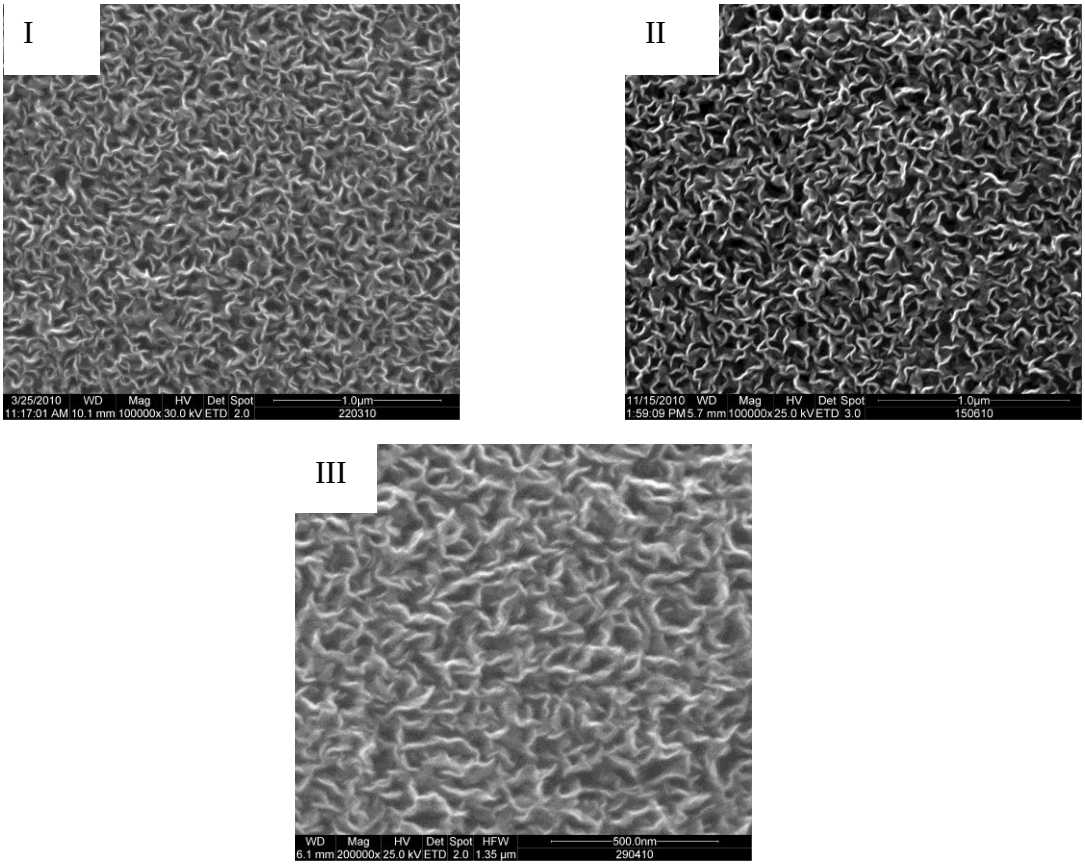


***Figure 25: SEM images of films deposited at various argon flow (I) 35 sccm (II) 45 sccm (III) 55 sccm at fixed plasma power 800 W and 250$^{o}$C substrate temperature.***

# 4.1.2.TEM observations

Figure 26 shows a low magnification TEM image of the typical CNWs growth. The TEM specimen was scraped away from the substrate and ultrasonicated, and then collected on a micro grid. A structure of overlapping plane sheets with a relatively smooth surface was observed in Figure 26(a). A high resolution transmission electron microscopy (HRTEM) image of the edge of CNWs is shown in Figure 26 (c). The high resolution TEM image of the CNW reveals the graphitized structure of the CNWs. These images reveal that the carbon is present as an amorphous matrix in which nanometer sized crystals of ca. 30 nm in diameter are embedded. The diffraction analysis allows the determination of distances of lattice planes. These distances of the lattice planes do not fit the value of metallic aluminium, but can be found in the XRD-spectrum of $Al_4C_3$-powder ("pure", Carl Roth GmbH + Co. KG, Karlsruhe, Germany). From this it can be concluded that the

nanocrystals are $Al_4C_3$. It should be mentioned that oxycarbides [129] could not be detected.

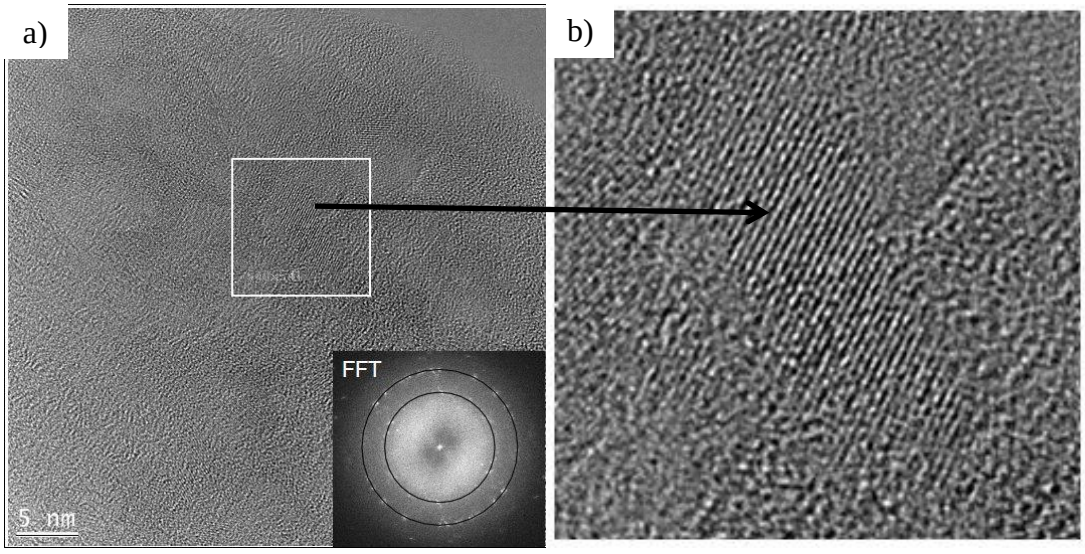


***Figure 26: TEM analysis, a) HAADF-STEM, lamellae consist of amorphous matrix with embedded nano crystals, b) cross sectional SEM image of CNWs, c) Cs corrected HRTEM, distance of lattice plane 0.188 nm, 0.130/ 0.134 nm, (d) a high resolution TEM image of CNWs, showing graphene layers.***

## 4.1.3.Raman spectra of CNWs

The Raman spectroscopy is extensively used for the characterization of carbon related materials including diamond, diamond like carbon, carbon nanotube, and CNWs. The main features in the Raman spectra of carbon are the so called G band and D band peaks, which lie at around 1580-1590 $cm^{-1}$ and 1350-1360 $cm^{-1}$ respectively, for visible excitation. Except for UV excitation, Raman spectra of carbon films are dominated by $sp^2$ sites, because visible excitation always resonates with the $\pi$ states. Thus even for highly $sp^3$ bonds containing amorphous carbon samples, the visible Raman spectra are due to $sp^2$ vibrations [130]. Only for diamond or samples containing a significant fraction of the diamond phase, the diamond $sp^3$ peak at 1332 $cm^{-1}$ is seen. The cross-sectional $sp^3$ C-C vibrational signal is negligible for visible excitation; thus, its Raman signature (eg. nano crystalline diamond) can only be seen for UV excitation. The cross-sectional signal for graphite at 514.5 nm is approximately 55 times higher than that of diamond [131]. The G band at 1580-1590 $cm^{-1}$ is the disorder induced phonon mode, resulting from the relaxation in the momentum selection rules of the Raman scattering process due to the

small domain size in graphite. Typical Raman spectroscopy of the CNWs, deposited at 665$^{o}$C substrate temperature and an argon flow of 27 sccm grown by ICP-CVD is shown in Figure 27. Raman spectra for the CNWs were measured at room temperature using the 514.5nm line of an argon laser. The typical Raman spectrum of such films have been found to have a strong peak at 1590 cm$^{-1}$ (G band) indicating the formation of graphitized structure and another peak at 1360 cm$^{-1}$ (D band) corresponding to the disordering induced phonon mode. It is found that the bandwidth of the G band is relatively narrow compared to usual graphite like carbon [129] even when the peak intensity ratio of D band to G band is significantly high. This spectral feature of CNWs is distinguished from those of typical graphite carbons reported so far [128]. Because the aluminium is not dissolved but precipitated as aluminium carbide, the spectra can be treated as pure carbon spectra. Compared with graphite and CNTs the D band of CNWs is very strong (as shown in Figure 27); it is due to the high edge density, surface oxidation [132], and nanocrystalline structure and to the presence of defects such as distortion, vacancies, and strain in graphitic networks, which are typical features in CNWs. Besides the G peak, a distinct shoulder peak at 1621 cm$^{-1}$ has been observed before [121,134,135] which is attributed to a D´ band which is only observed in some graphite like carbons and associated with the finite size of graphite crystals and graphene edges [136, 137, 138]. The strong D band peak and D´ band peak suggest a more nanocrystalline structure and presence of graphene edges and defects such distortion, vacancies, and straining of the graphitic lattice, which are prevalent features of CNWs. The Raman spectra have a strong and sharp D band peak and shoulder peak which are due to the small graphite domains and the existence of edges of graphene sheets. It was studied that the D´ band shoulder at 1602 cm$^{-1}$ is slightly different to the values given in literature. This can be because of the presence of the aluminium carbide inside the CNWs matrix. It is shown in Table 2, that the G band peak full width half maximum (FWHM), and the peak intensity ratio of the D band to the G band $I_D/ I_G$ correlate with the wall size of the CNWs. The $I_D/ I_G$ ratio depends on the wall sizes. Kurita et al. [133] analyzed the Raman spectra of CNWs of different sizes grown using DC plasma enhanced CVD and found that the relative peak intensity ratio $I_D/ I_G$ of the D band and the G band decreases linearly with increasing the walls size. The width of the G band is relatively narrow, even when $I_D/ I_G$ is significantly high. This feature of CNWs is distinguished from those of typical graphite like carbons

reported so far. From the comparison of these spectral features, they conclude flat nanowalls are composed of small crystallites with a high degree of graphitization. Similar results were found for present CNWs grown by ICP CVD at 27 sccm argon gas flow. A graph between $I_D/ I_G$ ratio and CNWs size is plotted in Figure 28 and the data is given in *Table 1*. The values of $I_D/ I_G$ vary from 1.73 - 2.63 and are increasing with decreasing the wall sizes. Thus, the mean size of walls is gradually decreasing and the carbon material is reducing the size in nanometer. Raman spectra explain more clearly the wall size phenomenon than SEM results; hence $I_D/ I_G$ ration is also an estimation parameter for the analysis of wall sizes of CNWs. As seen in Figure 29, CNWs grown by ICP- CVD by aluminium acetylacetonate source can produce sizes of walls from 20- 500 nm which are the minimum compared to other methods like DC plasma enhanced CVD [133]. CNW grown at various flow rates of argon gas were characterized by Raman spectroscopy to investigate the gas flow rate effect on the structural properties of CNWs.

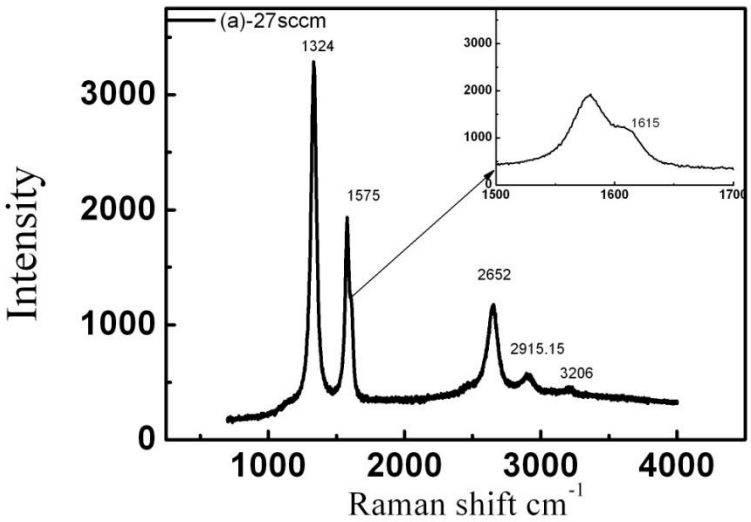


***Figure 27: Raman peaks of films (a), deposited at 27 sccm argon flow, 665$^o$C substrate temperature and plasma power of 800 W.***

Figure 29 shows the Raman spectra of CNWs deposited at constant temperature 665$^o$C and plasma power 800W with different flow rates of the argon gas. Raman spectra of all the CNWs films have a G peak around 1580 cm$^{-1}$ and a D band peak at around 1340 cm$^{-1}$. The G band peak is accompanied by a shoulder peak at 1607 cm$^{-1}$ (D' band peak). As described above the strong D and D' peaks indicate a more nanocrystalline structure and

the presence of graphene edges and defects, which are features of CNWs. Figure 30 shows the ratio of the peak intensity of the D band to that of the G band ($I_D$ /$I_G$).The $I_D$ /$I_G$ ratio decreased with an increase in argon flow rate, argon being the carrier gas for aluminium acetylacetonate. So it is indicated that the addition of argon gas to acetylacetonate is improving the crystallinity of CNWs by suppressing second nucleation, resulting in an improvement of the crystallinity of CNWs films as shown in the SEM and the TEM images of Figure 23 and Figure 26 respectively.

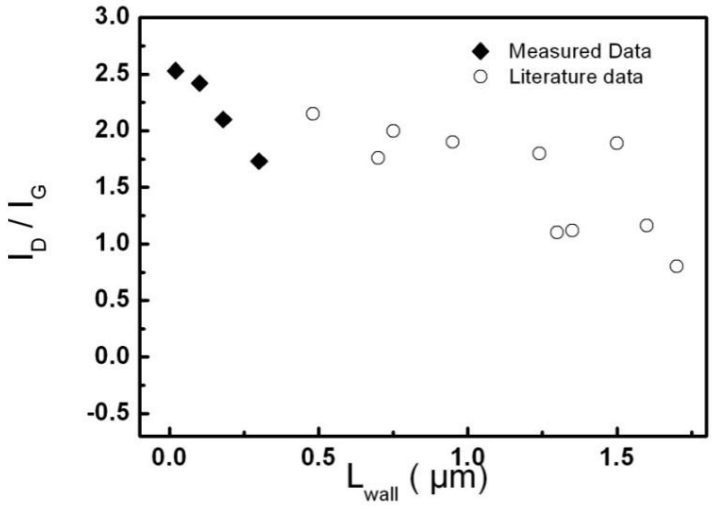


***Figure 28: Graph between wall size and ID/IG ratio. Comparison of wall size of CNWs with the reported data( films deposited by DC enhanced CVD) and present data ( film deposited by ICP-CVD).***

It is found that the bandwidth of the G band is relatively narrow, even when the peak intensity ratio of D band to G band is significantly high. This spectral feature of CNWs is distinguished from those of typical graphite carbons reported so far [133]. Because the aluminium is not dissolved but precipitated as aluminium carbide, the spectra can be treated as pure carbon spectra. Figure 31 shows Raman spectra of both, a CNW sample with $Al_4C_3$ inclusions and a pure $Al_4C_3$ powder sample. It is seen that some characteristic peaks in these spectra can be found at the same wave number positions making it difficult to assign specific peaks to that of $Al_4C_3$ in the CNW measurement. Just as the Raman spectra, additional XRD-measurements confirm the usual graphitic structure of the CNWs as mentioned in reference (Figure 33).

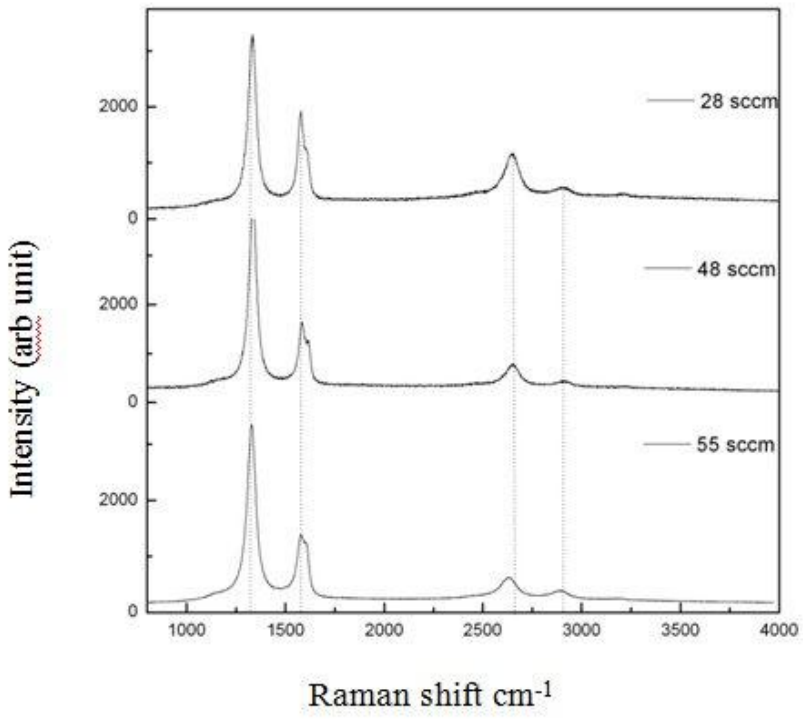


***Figure 29: Comparison of Raman spectra of CNWs at various argon flow rate. All films are deposited at constant substrate temperature 665$^{o}$C and plasma power 800W***

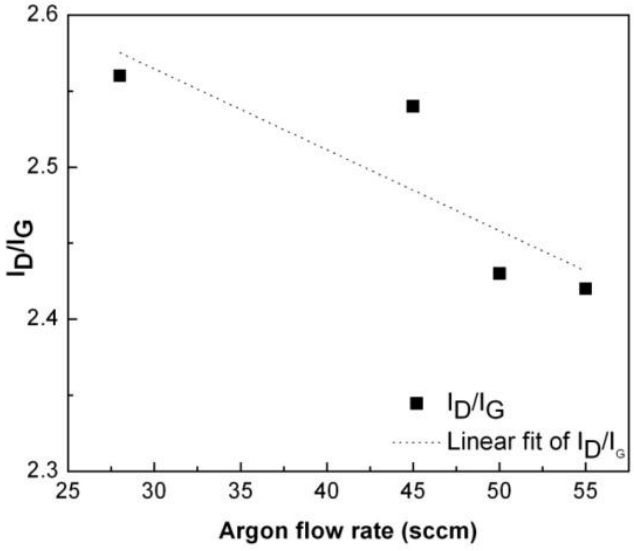


***Figure 30: The peak intensity ratio of the D and the G band as a function of the argon gas flow***

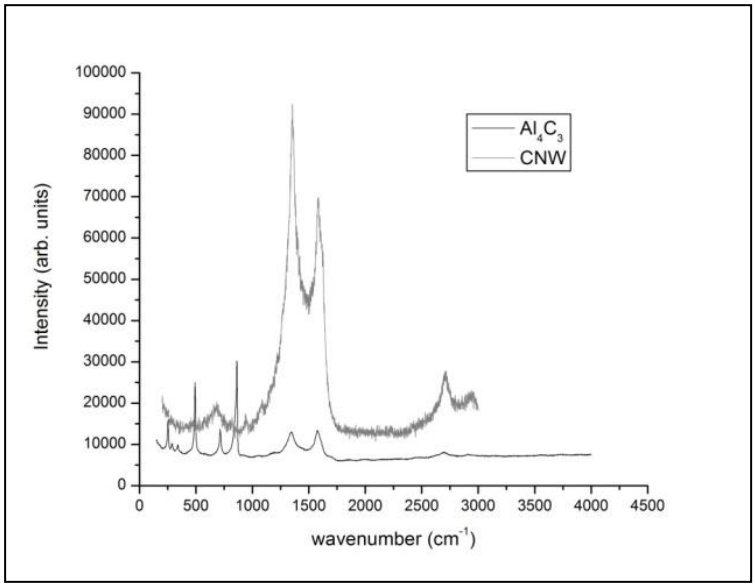


***Figure 31: Raman spectra comparison of $Al_4C_3$ powder sample and CNW sample***

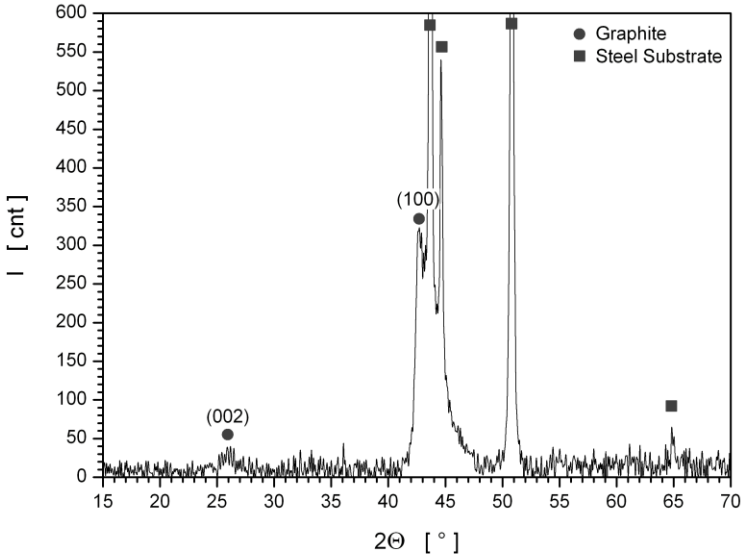


***Figure 32: XRD measurement of a film deposited at 35 sccm argon flow, and 665$^o$C substrate temperature***

The small crystallite size of the graphitic phase measured by XRD (Figure 32) is consistent with the high $I_D/I_G$ intensity ratio measured by Raman spectroscopy. Furthermore, the narrow FWHM (G) - one of the most important Raman spectral features in CNWs [133] indicates a high degree of graphitization in the films. Thus, it cannot be assured that the aluminium catalyzes the growth of the CNWs. On one hand, the TEM

analysis shows an amorphous carbon structure surrounding the $Al_4C_3$ nanoparticles suggesting that the formation of the $Al_4C_3$ leads to an amorphisation of the matrix in the vicinity of the precipitates. On other hand, similar structures can be produced using metalorganic-Ti-precursors like $Cp^*TiMe_3$ (Pentamethyl-cyclopentadienyltitan(IV)-trimethyl, $[(CH_3)_5C_5Ti(CH_3)_3]$. The electrical resistivity (at 137 K), determined using a four probe STM (Omicron) with a tip distance of 10 µm, was 800 Ohm $*$ $cm^{-1}$ giving no hint of Al functionings as a dopant.

## 4.1.4. Effect of argon gas flow on surface stoichiometry

### 4.1.4.1. EDX Analysis

Figure 33 shows an EDX pattern of CNWs deposited on a stainless steel substrate. The EDX shows the presence of carbon, aluminium, oxygen and Fe as well as chromium and nickel which are generally present in stainless steel substrates. Figure 34 shows the EDX pattern of the film after normalizing the substrate components like Fe, Cr, and Ni. A typical extraction of chemical composition datas from a CNW/stainless steel sample made by using the EDX method is shown in Table 2.

EDX measurements (Figure 34) show that the atomic content of aluminium gradually increases with increasing argon flow. Also, the carbon content decreases with argon flow rate. The atomic content of aluminium is 0.9% when deposited at 28 sccm argon gas flow. With increasing flow rate of up to 45 sccm and 55 sccm, the atomic content increases up to 1.27% and 2.63% respectively. Hence, the aluminium concentration in the CNW sample increases with increasing the argon gas flow rate.

***Table 2: Quantitative analysis of chemical composition by EDX***

| Element | Wt % | At % |
|---|---|---|
| **C K** | **43.43** | **70.89** |
| O K | 9.53 | 11.68 |
| **AlK** | **2.03** | **1.48** |
| CrK | 8.43 | 3.18 |
| FeK | 33 | 11.58 |
| NiK | 3.58 | 1.19 |
| Total | 100 | 100 |

The effect of argon gas flow on the structure of CNW it has already been discussed that the wall size of CNWs decreases with increasing the argon gas flow. EDX also suggests that with increasing flow rate of argon, aluminium concentration increases and the wall size (SEM) of the CNWs decreases. Hence at high percentage of aluminium in the films, minimum size of walls. From the TEM analysis, aluminium forms aluminium carbide crystals embedded inside the CNW matrix. The two possibilities are there, either aluminium acts as an impurity inside the CNW matrix, aluminium behaves like a catalyst. The amount of aluminium in the films is very small (less than 3%), so it can also behave as an impurity inside the films. The impurities reduce the size of grains and create defects such as distortion, vacancies, and straining dislocations. Small wall sizes, defects like distortions and vacancies are the properties of the CNWs which have been observed. Hence, aluminium carbide patches may be considered like the impurities which decrease the size of the CNW walls. It is unclear if aluminium is functioning as a dopant.

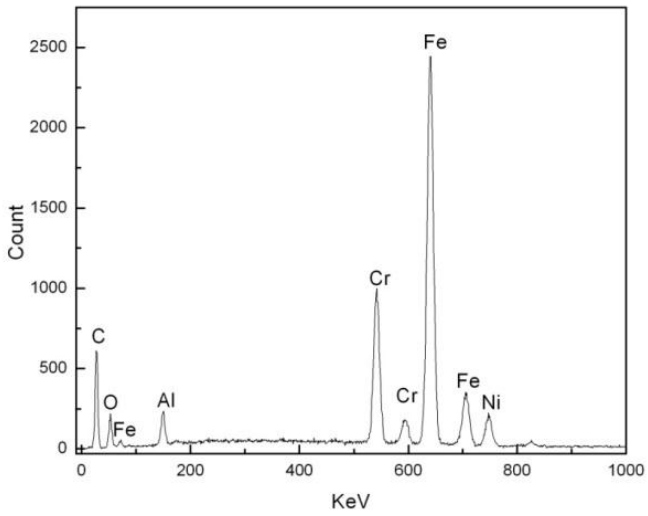


***Figure 33: EDX pattern of CNWs deposited on a stainless steel substrate.***

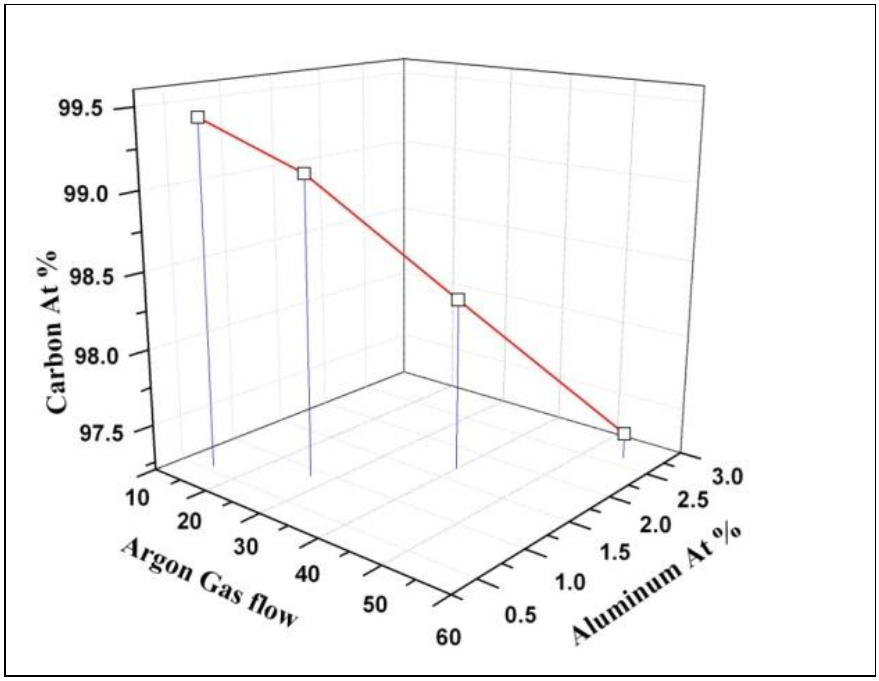


***Figure 34: Carbon and aluminium content in atomic weight % changing with argon gas flow for typically deposited CNWs. Data are extracted from EDX quantitative measurements.***

Because the electrical resistivity (at 137 K), determined using a four probe STM (Omicron) with a tip distance of 10 µm, was 800 Ohm $*$ $cm^{-1}$ giving no hint of Al functioning as a dopant.

It is common to use catalysts like metals and aluminium oxide in the growth of CNWs/ CNTs [118]. It can't be assured that aluminium catalyzes the growth of the CNWs. As TEM analysis shows an amorphous carbon structure embedding $Al_4C_3$ nanoparticles suggesting that the formation of $Al_4C_3$ leads to an amorphisation of the matrix in the vicinity of the precipitates. Also, similar structures can be produce by using another metal organic Ti-precursor like Cp*$TiMe_3$ (Pentamethyl-cyclo penta dienyltitan (IV)-trimethyl, $[(CH_3)_5C_5Ti(CH_3)_3]$.

## 4.1.4.2. SIMS and NRA Analysis

The secondary ion mass spectroscopy (SIMS) and the NRA are studied. Three films, deposited at constant 665$^oC$ substrate temperature and plasma power (800W) and varying argon flow rate from 28 sccm to 55 sccm were analyzed. SIMS analysis shows (Figure 35) that the atomic content of aluminium inside the films varies with the flow rate of argon gas. Thus, it can be concluded that the aluminium content can be controlled by the argon gas flow. The hydrogen content has been determined from SIMS depth profile. The more accurate information about $H_2$ content is determined by NRA [136]. SIMS and NRA result are shown in Figure 36. The hydrogen content is between 3% and 5% independent from the argon flow. The depth profile shows a rather homogeneous distribution within the film as shown in Figure 37.

.

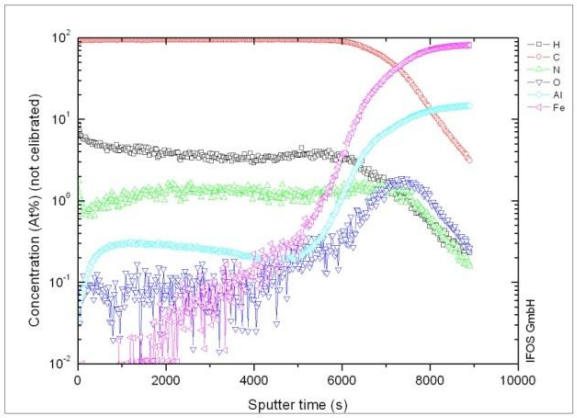


***Figure 35: SIMS measurement of sample (a)***

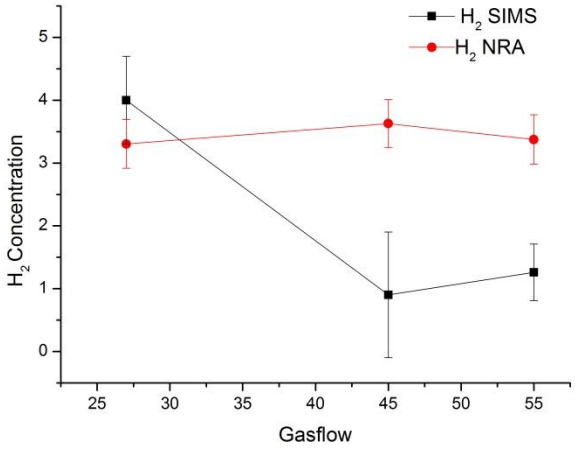


***Figure 36: Variation of hydrogen percentage with gas flow by SIMS and NRA measurements***

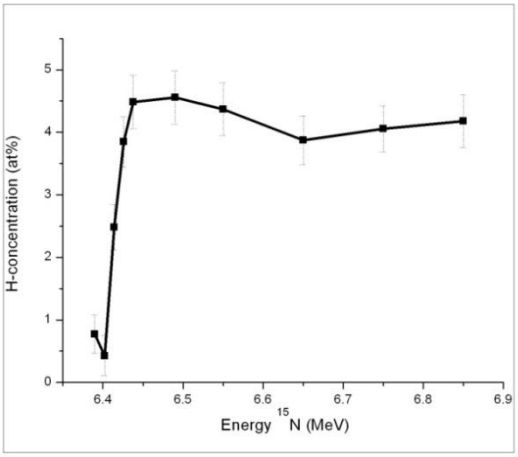

*Figure 37: NRA depth profile*

## 4.1.4.3. XPS Analysis

Al 2p peaks as a function of the precursor flow rate are shown in Figure 38. The continuous lines show the experimental data while the fits are drawn as dashed lines. The asymmetry of the peaks indicates the existence of two aluminium species in the samples: $Al_4C_3$ and $Al_2O_3$. The spin-orbit split ($\Delta$=0.4 eV [137]) of the Al 2p line could not be resolved within the resolution of our equipment. The Al 2p line was fitted using two peaks spaced 1.6 eV apart (see the inset of Figure 38), the 74.6 eV peak being due to aluminium carbide and the peak at 76.2 eV being attributed to spurious aluminium oxide. The signal is clearly dominated by aluminium carbide (80-90% of the integrated peak area). No significant variation of the binding energy was found in comparing the different films indicating similar aluminium environments for all precursor concentrations. The total area of the Al 2p peak correlates well with the concentration of aluminium due to the variation of the argon flow found by SIMS Figure 39 shows a comparison of the emission from the C 1s state between two CNW samples prepared at increasing argon flows.

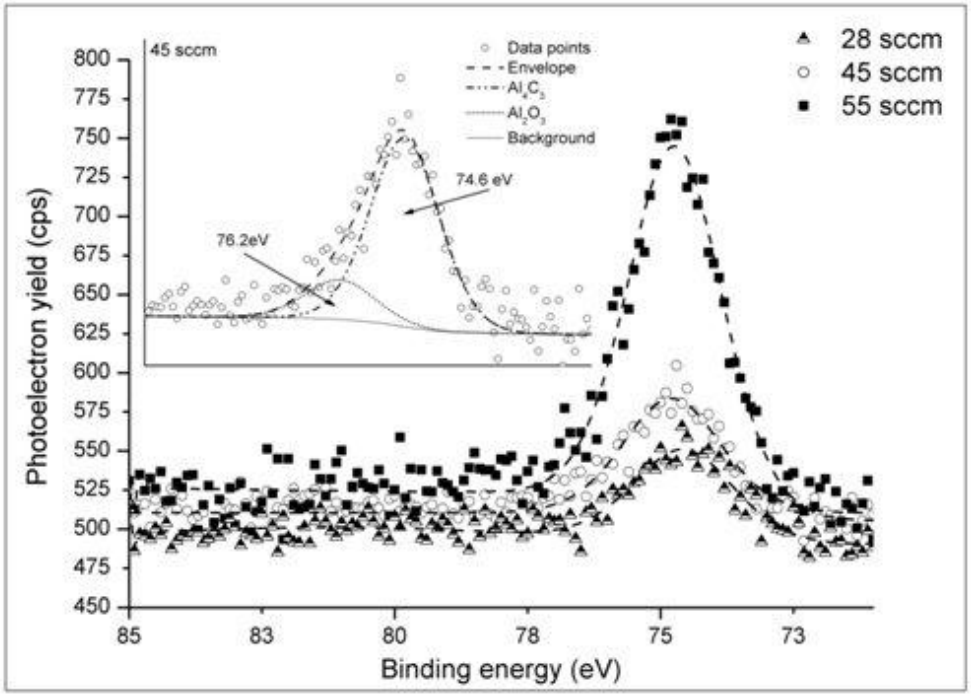

***Figure 38: Comparison of Al 2p XPS spectra for different flow rates***

The structure and the position of the C 1s peak at 284.7 eV show the graphitic nature of the carbon forming the CNW in the film. No additional influence of the precursor concentration on the peak shape and hence the carbon bonding structure could be found.

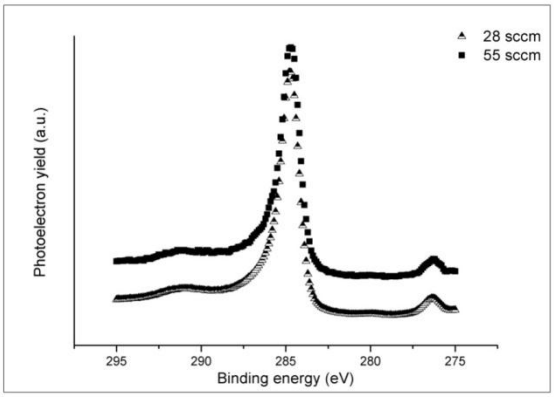


***Figure 39: Comparison of C 1s peaks for two different flow rates***

Taking the position of the C 1s peak as a reference point for the spectra, good agreement between the results reported in this study and $Al_4C_3$ reference spectra can be established. In Table 3, XPS analysis is compared with data from previously reported work [138, 139] on aluminium-carbon interfaces. A relative spacing between the C 1s position and the low binding energy component of the Al 2p line of $\Delta$=210.1 eV is found, which agrees well with the data reported by Maruyana et al. [138] and Hua et al. [139] and confirms our assignment of this peak to the $Al_4C_3$ species. Our interpretation is additionally supported by the spacing between the $Al_4C_3$ and $Al_2O_3$ features which agrees with the one reported in the literature.

***Table 3:Comparison of XPS-data evaluated in present work and previous works***

| Element | Present work | Maruyama et al. [138] $\Delta$=E(C1s)-E(Al2p) | Hua et al. [139] (distance to data acquired in the present work) |
|---|---|---|---|
| C 1s /eV | 284.7 | 284.1 | 284.4 |
| $Al_4C_3$ / eV | 74.6 | 73.6 | 74.2 |
| | $\Delta$ =210.1 | $\Delta$ =210.5 | $\Delta$ =210.2 |
| $Al_2O_3$ /eV | 76.2 | 75.2 | - |
| | $\Delta$ =208.5 | $\Delta$ =208.9 | |

# Summary

This chapter explains the physics of CNWs produced by ICP−CVD using a metal organic precursor on different substrates like silicon or steel. The chapter introduces the production of CNWs without using an additional catalyst or reactive gases. It can be deposited at various substrate temperatures ($225^oC$-$665^oC$). The work can be summarized as follows:

- SEM studies explain that the sizes of carbon walls are influenced by various plasma parameters like substrate temperature, argon flow, and plasma power.
- EDX and SIMS show that the aluminium content inside the film can be controlled by the flow of argon gas and it significantly influences the size of walls as well.
- Raman analysis shows the typical CNWs peaks with high ID/ IG ratio, which is so far reported, the smallest size of CNW.
- TEM images conclude that there are some crystallite inclusions inside the graphitic matrix. It is evident from XPS that the crystalline inclusion is nothing else but aluminium carbide ($Al_4C_3$).

# References


117. Mori T, Hiramatsu M, Yamakawa K, Hori M "Fabrication of carbon nanowalls using electron beam excited plasma- enhanced chemical vapor deposition" Diamond and Related Materials 17 : 2008, 1513-17
118. Hiramatsu M, Hori M "Fabrication of carbon nanowalls using novel plasma processing" Japanese Journal of Applied Physics 45: 2006, 5522-27
119. Malesevic A, Vizireanu S, Kemps R, Vanhusel A, Haesendonck C.V, Dinescu G "Combined growth of carbon nanotubes and carbon nanowalls by plasma-enhanced chemical vapor deposition" Carbon 45: 2007, 2932-37
120. Vizireanu S, Stoica S.D, Luculescu C, Nistor LC, Mitu B "Plasma technique for nano structured carbon materials synthesis. A case study: carbon nanowall growth by low pressure expanding RF plasma" Plasma Source Science Technology19: 2010, 034016
121. Hiramatsu M, Hori M "Fabrication of vertically aligned carbon nanowalls using capacitively coupled plasma enhanced chemical vapor deposition assisted by hydrogen radical injection" Applied Physics Letters 84: 2004, 4708-10
122. Jain H.G, Karacuban H, Krix D,Becker H-W, Nienhaus H, Buck V "Carbon nanowalls deposited by inductively coupled plasma enhanced chemical vapor deposition using aluminium acetylacetonate as precursor" Carbon 49: 2011, 4987-95
123. Sato G, Morio T, Kato T, Hatakeyama R "Fast growth of carbon nano walls from pure methane using helicon plasma- enhanced chemical vapor deposition" Japanese Journal of Applied Physics 45: 2006, 5210-12
124. Wu Y, Qiao P, Chong T, Shen Z "Carbon nanowalls growth by microwave plasma enhanced chemical vapor deposition" Advanced Materials 14 : 2002, 64- 67
125. Shang N. G, Au F.C.K, Meng X.M, Lee.C.S, Bello I, Lee S.T "Uniform carbon nanoflake film and their film emission" Chemical Physics Letters 358: 2002, 187-191
126. Dikonimos Th, Giorgi L, Giorgi R, Lisi N, Salernitano E, Rossi R "DC plasma enhanced growth of oriented carbon nano walls films by HFCVD" Diamond and Related Materials 16 : 2007, 1240-1243
127. Shimabukuro S, Hatakeyama Y, Takeuchi M, Itoh T, Nonomura S "Preparation of carbon nanowall by hot wall chemical vapor deposition and effect of substrate

temperature and filament temperature" Japanese Journal of Applied Physics 47: 2008, 8635-40

128. J. M. Lihrmann "High-temperature behavior of the aluminium oxycarbide $A1_2OC$ in the system $AI_2O_3$-$Al_4C_3$ and with additions of aluminium nitride" Journal of American Ceramic Society72: 1989, 1704-09

129. Ferrari AC "Raman spectroscopy of graphene and graphite: Disoders, electron-phonon coupling , doping and nonadiabatic effects" Solid State Communication 143: 2007, 47-57

130. Wada N gaczi Pj, Solin SA "Diamond like 3 fold coordinated amorphous carbon" Journal of Non- Crystalline Solids 35-36: 1980, 543-548

131. Ni ZH, Fan HM Feng YP Shen ZX, Yang BJ, Wu YH "Raman spectroscopic investigation of carbon nanowalls" Journal of Chemical Physics124 : 2006, 204703-5

132. Kurita S, Yoshimura A, Kawamoto H, Uchida T, Kojima K, Tachibana M "Raman spectra of carbon nanowalls grown by plasma-enhanced chemical vapor deposition" Journal of Applied Physics 97: 2005, 104320-5

133. Malesevic A, Vizireanu S, Kemps R, Vanhusel A, Haesendonck C.V, Dinescu G "Combined growth of carbon nanotubes and carbon nanowalls by plasma-enhanced chemical vapor deposition" Carbon 45 : 2007, 2932-37

134. Nemanich RJ, Solin SA "First and second order raman scattering from finite size crystals of graphite" Physics Review B 20: 1978; 392-401

135. Yu J, Zhang Q, Ahn J, Yoon SF Rusli, Li YJ, Gan B, Chew K, Tan KH "Field emission from patterned carbon nanotubes emitters produced by microwave plasma chemical vapor deposition" Diamond Related Materials 10: 2001, 2157-60

136. Lanford W.A "Analysis for hydrogen by nuclear reaction and energy recoil detection" Nuclear Instrument and Methds B 66: 1992, 65-82

137. Crist B V "Handbook of Monochromatic XPS Spectra, The Elements of Native Oxides" Wiley 2000

138. Maruyama B, Ohuchi FS, Rabenberg L "Catalytic carbide formation at aluminium-carbon interfaces" Journal of Materials Science Letters 9: 1990, 864-66

139. Hua L, Dian-hong S, Xin-fa D, Qi-kun X, Froumin N, Polak M "Study of the Al/Graphite interface" Chinese Physics 10: 2001, 832-35

# 5. Electron Emission in CNWs

There are various materials, which have proven their application as electric field emitters. The carbon gives the possibility to form various phases of carbon structure. Diamond/graphite composite materials have good field emission properties and have received enduring attention due to the strong potential of this material. It can be employed as the cold cathode material in flat-panel displays and other electronic emitting devices. In the very beginning, research was focused on diamond [140, 141]. Special surface treatments of diamond to the (1 1 1) crystal plane produce a property called "negative electron affinity" NEA [142]. Basically it says that electrons may be emitted from this (111) crystal plane surface into vacuum without having any barrier, with the condition that the conduction band has been populated. If electrons can be supplied, diamond should emit electrons at very low applied fields. The property of negative electron affinity (NEA) that can be displayed by diamond form of structure is not the only reason for low electron emission application [143]. Moreover, films properties are found to depend on the crystalline structure of grain boundaries, which determine the electrical and optical characteristics of the films [144,146]. When the system (thin films) moves towards nanostructure size, the grain size reduces. With the reduction in grain size, graphitic inclusions and H content inside the grain boundaries increase. Inside the grain boundaries, the interconnected network is formed by $sp^2$ bounded carbon. In the interconnected network, electrons are free to move inside the carbon structure (nano). This phenomenon makes a carbon nanostructure like a conduction promoter [146]. However, the reports on whether hydrogen incorporation within the structure will increase or decrease conductivity are controversial [145, 146]. Carbon nanotubes and nanocrystalline diamond with some graphitic inclusion have shown low onset fields, and a homogenous emitter distribution with large number densities [147]. Microscopic field emission (FE) investigations suggested that a high electric field enhancement occurs at the conducting graphene layers between diamond crystallites [148]. In spite of their random growth, vertically oriented carbon nanowalls (CNWs) with high aspect ratio and sufficient electric conductivity might be useful for simple FE devices in diode configuration (e.g. flat lamps), especially if practical substrate materials could be used. For gate-controlled

devices, however, either structured growth or post-structuring of CNWs is required. The investigations of emission from CNWs for the application as cold cathode have been discussed. First results on laser-structured CNWs on Si and stainless steel substrates are described in this chapter and reported [149].

# 5.1. Emission by Integral measurement system with luminescent screen (IMLS)

The first experiment of emission has been done by integral measurement system with luminescent screen (IMLS). Main aims of investigation were:

- To make a conclusion about usability of such sample as a cold cathode.
- To estimate onset field, maximal integral current capability, density of emitters, total uniformity and stability of emission.

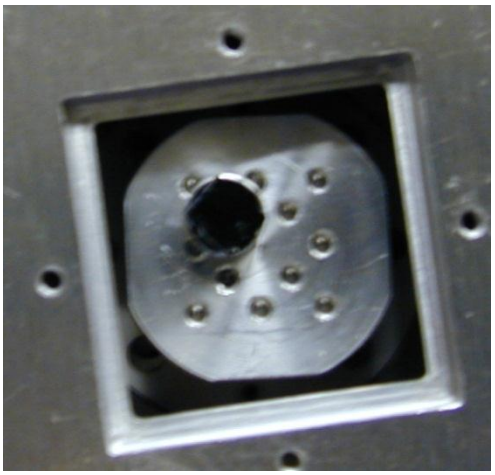

***Figure 40: The position of the sample (≈6.3x4.2 mm$^2$) in IMLS***

For this experiment, the sample has been attached to the aluminium cathode-holder by means of a SEM button and aluminium foil to provide good electrical contact. The position of camera frame is the same in Figure 40 and during measurements. The edges of the sample on the round holder are marked with the white rectangle in Figure 40. Obviously, the sample is diagonally oriented about 45º. During the IMLS measurements cathode-screen spacing was about 300 µm. Base pressure in chamber was about $1.5 \cdot 10^{-6}$ mbar. Partial sulphur pressure controlled by quadropole mass-spectrometer to avoid the destruction of phosphor screen was in the range $0.2\text{-}0.22 \cdot 10^{-11}$ mbar.

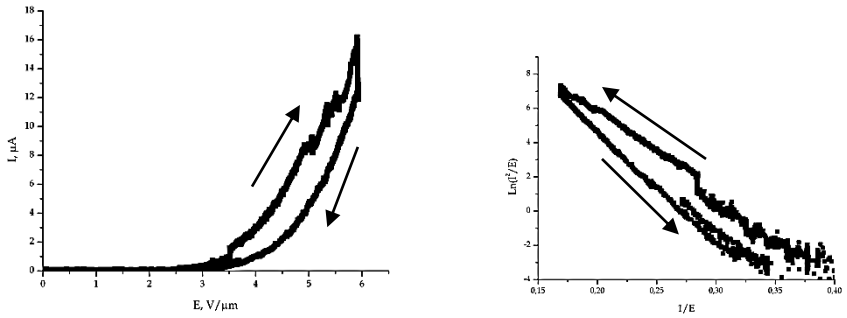


***Figure 41: I(E)-curve and FN-plot observed during first dc-test.***

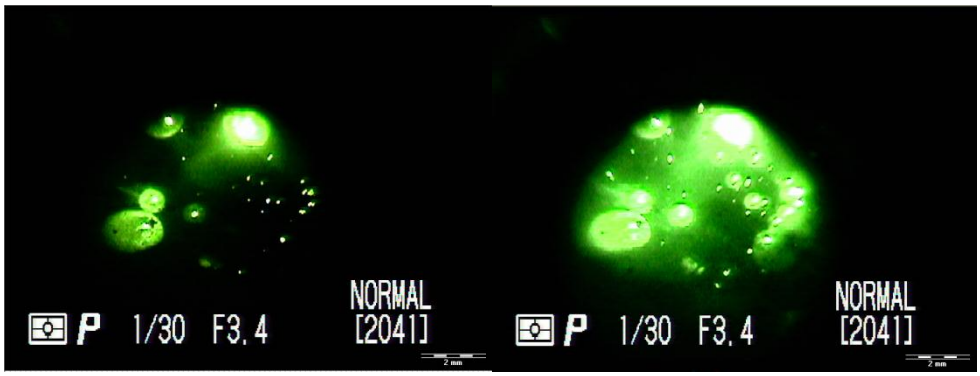


***Figure 42: Emission images acquired during first dc-test: Left at 5.2 μA, 4.5 V/μm; Right at 16 μA, 5.8 V/μm***

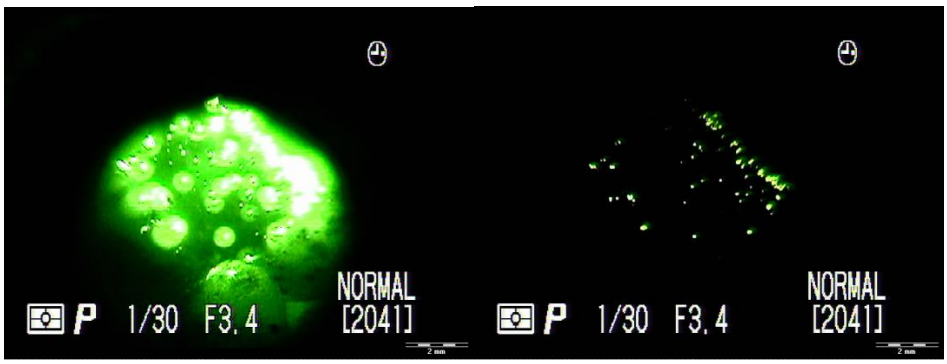


***Figure 43: Emission images observed (a) during pulsed processing (81 μA @ 10.4 V/μm) and (b) after processing (2.5 μA @ 4.8 V/μm). Current was measured at flat part of pulse. Duty cycle was 2:20 ms***

The IMLS experiment included two direct current (dc) tests and one pulsed test. In Figure 41, the I-E curve and FN plot has been observed during first DC text. I(E)-curve has a hysteretic character and stabilized emission behavior of the sample during down-cycle.

Integral field enhancement factor was reduced from 5350 (increase of voltage) to 4100 (decrease).

Figure 42, shows the ascending of field was stopped at 5.8 V/μm to avoid the destruction of the phosphor screen due to some strong emitting spots. It can be explained by partial destruction of strongest emitters what corresponds to decreasing of integral β. An averaged density of emitters of about 200 per $cm^2$ at 4.5 V/μm was observed in first DC test (Figure 42). Pulsed processing effect has been observed in Figure 43. With increasing the field, emission increases and at the highest field the strongest emitters were destructed. Also the emission was redistributed. Integral field enhancement factor (Figure 44) was decreased from 3780 down to 2950 during the processing. An averaged density of emitters of about 950 per $cm^2$ at 10.4 V/μm was observed. In Figure 45, FN-plot integral field enhancement factor is about 3000 is calculated. From this first experiment it was summarized that the sample showed onset field about 3.7 V/μm (for 1 μA), total current up to ~20 μA in dc and 80 μA in pulsed tests. The emission homogeneity over whole area of the sample is moderate and has been improved by pulsed processing. The destruction of strong emitters during IMLS measurements has led to stabilization of emission behavior and increasing of onset field from 3.7 up to 4.5 V/μm. Integral field enhancement factor was decreased from 5350 to 3000 during experiment. An averaged density of emitters was 200 and 300 per $cm^2$ (for ~4.6 V/μm) in first and second DC test, shown in Figure 42 and Figure 46 respectively, and was increased up to 950 per $cm^2$ (at 10.4 V/μm) in pulsed test. Investigated type of nanosheets-sample can be used as a cold cathode. To reach more uniform emission, structuring the CNWs has been used.

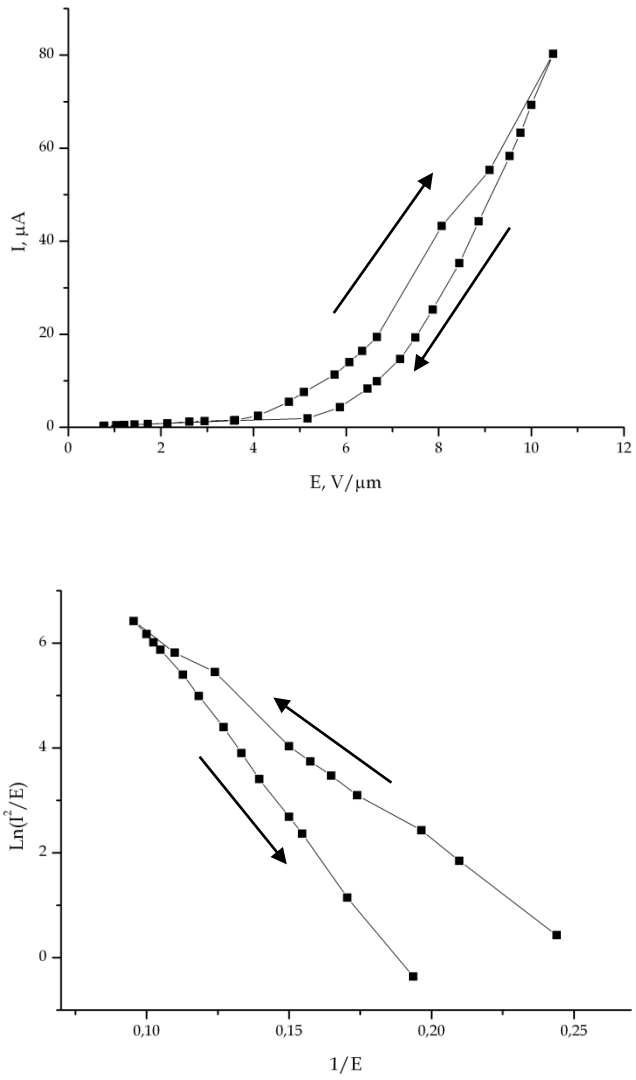


***Figure 44: I(E)-curve and FN-plot (pulsed processing test)***

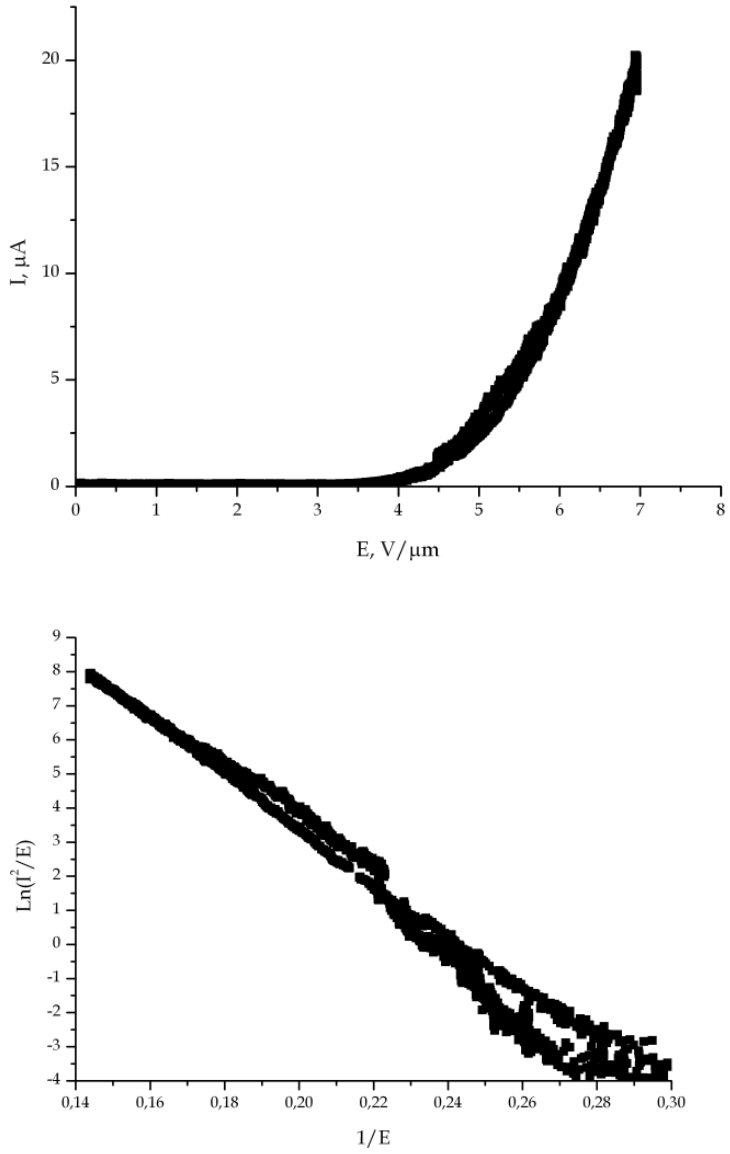


***Figure 45: I(E)-curve and FN-plot observed during second DC test.***

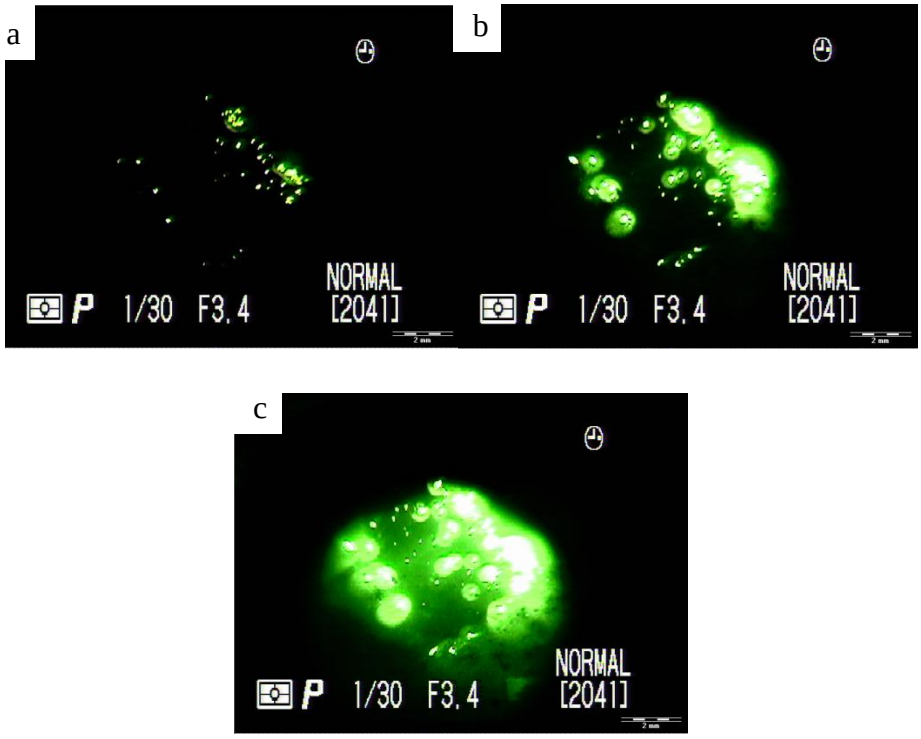


***Figure 46: Emission images acquired during the 2nd dc-test at (a) 2.2 μA, 4.6 V/μm, (b) 6.7μA, 5.8 V/μm and (c) 20 μA, 7 V/μm. Density of emitters at 4.6 V/μm is ~300 per cm$^2$***

# 5.2. FESM investigation of structured CNW-block cathode

## 5.2.1.Structuring/Patterning of carbon nanowalls

As described in earlier section, CNWs can be used as an cold cathode. For the uniform emission structuring of CNWs is required. Laser structuring has been used to pattern carbon nanowalls, which are coated on silicon and stainless steel samples. Diode pumped solid-state laser has been used for such patterning. The laser was operated at a wavelength of 532 nm, at a pulse length of 10 ns, and at a pulse frequency of 50 kHz. During patterning, the focused laser spot with a $1/e^2$ diameter of about 30 µm was moved across the sample surface at a writing speed of 30 cm/s. The average laser power was set to 1.15 W (Si) and 2.08 W (stainless steel), respectively. Quadratic grid patterns with a pitch of 60 µm were fabricated over an area of 5x5 mm$^2$. In Figure 47, a patch of CNWs arrays is shown. The cathode contains arrays of CNW-blocks of around 20 x 20 µm with 60 µm

pitch and around 20 µm of height (Figure 48 a, b) (prepared blocks) are used for testing in a field emission scanning microscopy (FESM).

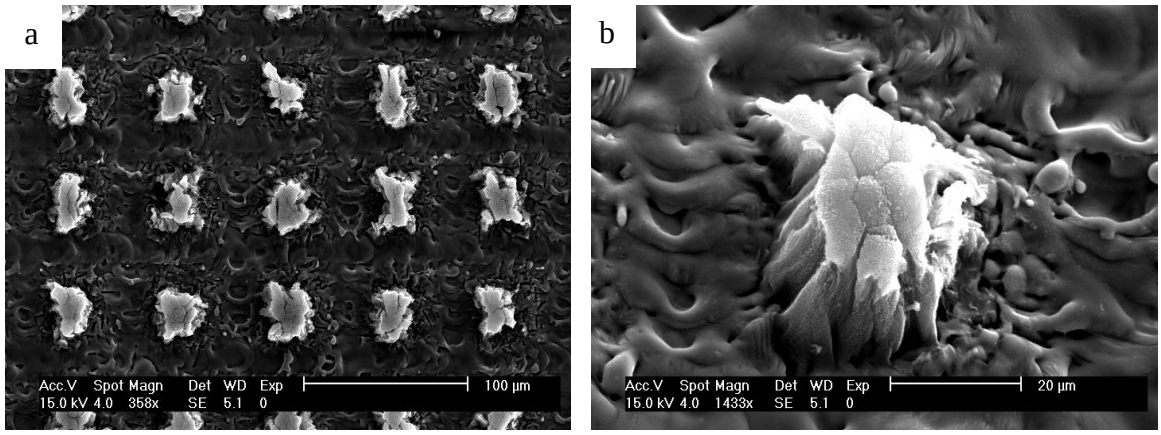


***Figure 47: SEM images of untested CNW- blocks on a silicon substrate. Different shapes of the CNW-blocks lead to different field emission results (FE). a) top view b) 30º tilt view***

# 5.3. FESM of carbon nanowalls

The FE properties of the laser-structured CNW cathodes were measured with a field emission scanning microscope (FESM) at a vacuum of $10^{-9}$ mbar using a tungsten anode of truncated cone shape with adjusted diameter ($\varnothing_a$=30 µm) at a gap $\Delta z$ [140]. In order to investigate the FE mechanism and achievable current limit of the CNWs, local current-voltage measurements were performed on selected patches (e.g. the numbered ones in Figure 49 d). The local field was always calibrated by means of V(z) plots [145]. From a detailed top view SEM image of the CNW-block, it looks cracked ,(Figure 48 left) as well as looks like inhomogeneous CNW spherical aggregates (Figure 48 right). Therefore, the current jumps and different FE properties are possible during the measurements. In order to investigate the homogeneity and the alignment of an emission from the cathode, seven (two) voltage scans at fixed field emission current (at 1nA) were performed in different areas of the cathode with $Ø_{anode}$ = 30 µm (3 µm).

Medium Figure 49 (a, b) and high (Figure 49 c) resolution voltage maps show that most emitting areas of the cathode emit at a field of 10-20 V/µm. Voltage maps of the cathode showed fairly visible alignment of emission and nearly a 100 % of emitting CNW-blocks but with moderate homogeneity.

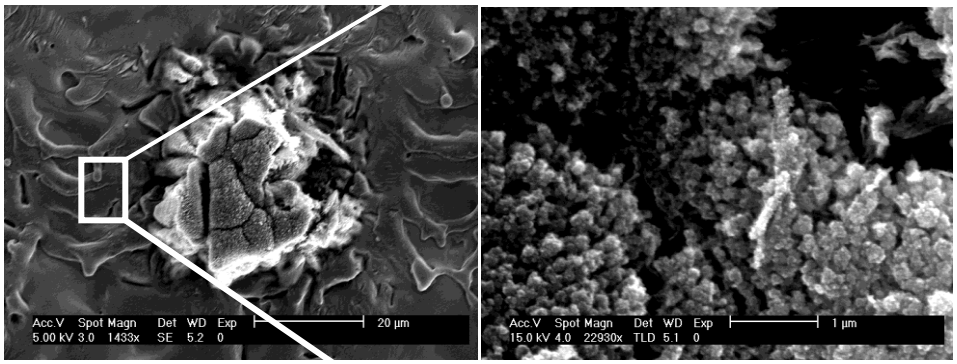


***Figure 48: Top view SEM image of untested CNW-block: CNW- block looks shattered into many pieces (on the left) and CNW spherical aggregates (on the right)***

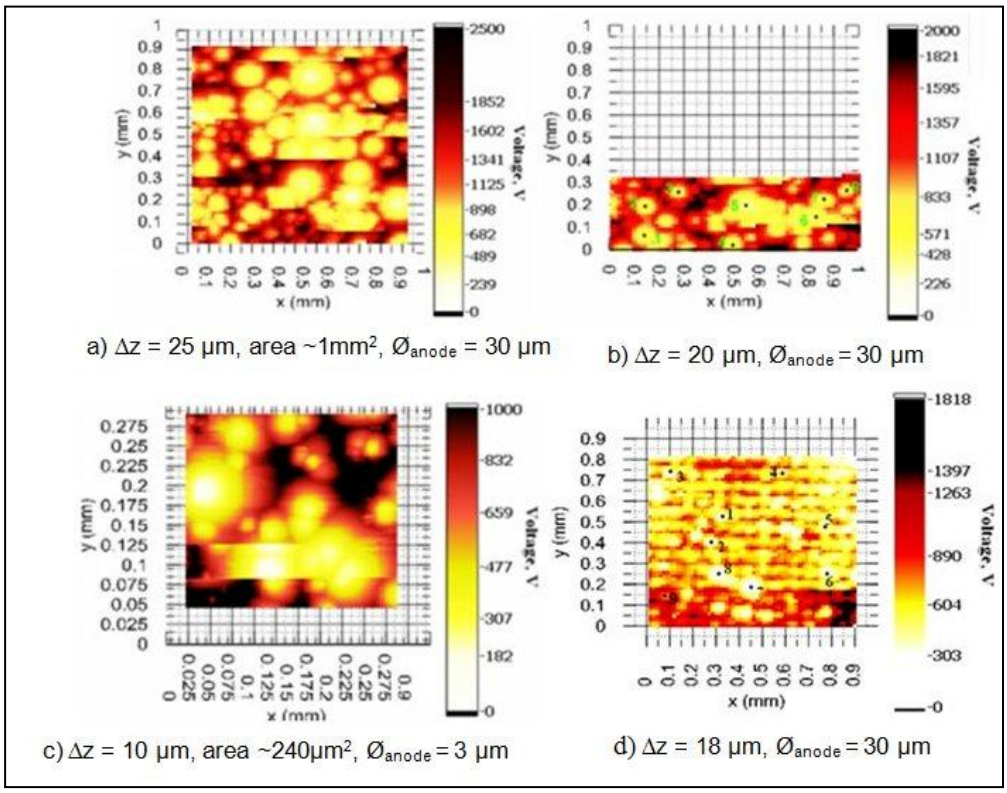


***Figure 49: Voltage maps at 1 nA fixed FE current scanned with Ø$_{anode}$ = 30 µm (a, b, d) and Ø$_{anode}$ = 3 µm (c). Scan (b) was automatically stopped because of a current jump***

There are some strong emitters, which lead to a scattering of the onset field of the CNW-blocks and less homogeneous emission. It is due to a different geometry of blocks Figure 47 (a) and their rectangular shape. As shown in these figures, aligned FE was obtained from nearly all CNW patches at Eon (1nA) = 10-20 V/µm on both substrates. The

homogeneity of the FE, however, appears rather limited due to the varying shape of the individual CW patches. In Figure 50, SEM image of the part of the cathode after the voltage scans. It can be seen that a lot of CNW-blocks have been partially destroyed by current jumps.

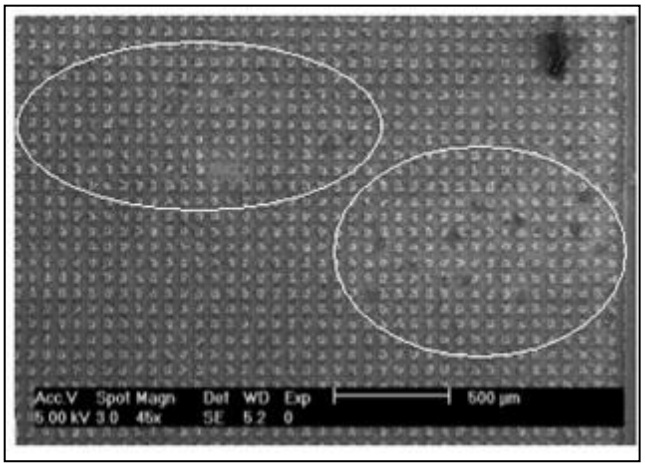


***Figure 50: SEM image of a part of the cathode where a few voltage scans at 1 nA fixed FE current were done. There are many CNWs-block that have been partially destroyed during the scan due to current jumps***

In order to investigate FE properties of individuals CNW-blocks, local measurement on 8 blocks with the diameter of the anode being $Ø_{anode}$ = 30 µm have been performed from a previous voltage map (Figure 49b) (numbers correspond to the numbers in Table 4.) Each CNW-block was measured in the loop with step by step increase of the current. Processing at constant voltage was carried out when the current value reaches at $I_{proc}$. Positions of the needle were estimated by means of the optical system and coordinates of the stepping motor. Local distance $\Delta z$ has been measured by U(z) plot for each emitter. All measurement results are shown in Table 4.

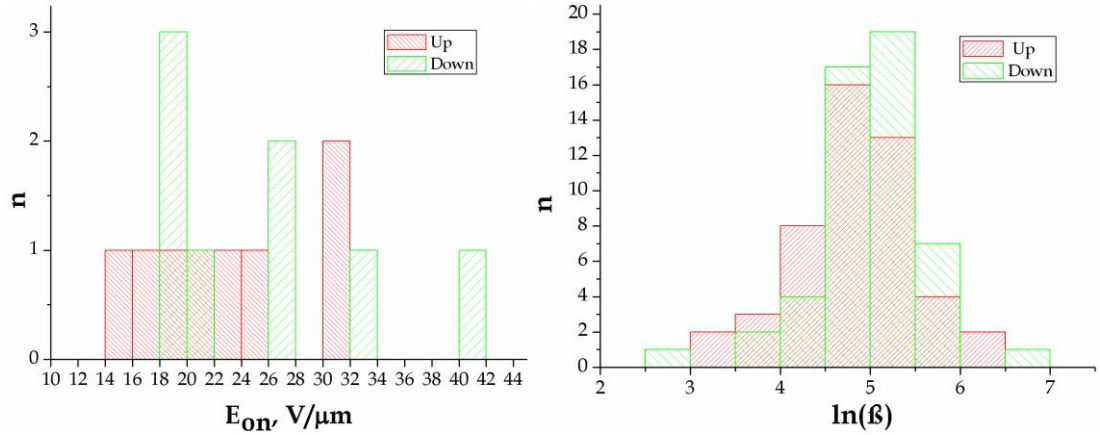


***Figure 51: Histograms of the onset field (at 1nA FE current).(mean value up = 22 V/µm (down = 25 V/µm)) (on the left) and the field enhancement factor (mean value ln($ß_{up}$) = 4.84 (ln($ß_{down}$) = 5.01) or $ß_{up}$ = 126 ($ß_{down}$ = 149)) (on the right)***

Measured with $Ø_{anode}$= 30 µm, the value of the onset field for CNW-blocks scatters from 14 to 32 V/µm (from 18 to 42 V/µm) during up (down) cycle (Figure 51 left). Changes of $E_{on}$ after up cycling and processing indicate changes by the FE current on the emitter geometry. The Field enhancement factor, extracted from different parts of all FE plots of all CNW-blocks (assuming a work function of 4.9 eV) shows a Gaussian like distribution (Figure 51 right) changes by the FE. Local measurements show the expected hyperbolic correlation between onset field and field enhancement factor (Figure 52). For CNWs on Si a hyperbolic correlation between $E_{on}$ (1nA) and the field enhancement factor β (assuming a work function of 4.9 eV) resulted. Typical observed FN plots of measured CNW-blocks are given in Figure 53 - Figure 57. Most of FN has shown FN-like distribution (Figure 53- Figure 54) at low external field and a saturation region at a higher field (Figure 55, Figure 56). The saturation could be due to adsorbents on the emitter tip and/or emission from the Si-substrate (p-type). Usual Fowler-Nordheim-like behavior was always observed. Slightly higher β values for down than for up cycles might be caused by adsorbent effects. In comparison, the measured $E_{on}$(1nA) values for CNWs on stainless steel were on average somewhat higher and less correlated to the β values. A large scattering was also obtained for the maximum current values $I_{max}$ (~1-100 µA) of the CNW patches on both substrate materials (Figure 58). As shown in these figures, fairly aligned FE was obtained from nearly all CNW patches at $E_{on}$(1nA) = 10-20 V/µm on both substrates.

**Table 4: Results of local measurements by $Ø_{anode}$ = 30 µm**

| *№* | | *Δz, µm* | *↑$E_{on}$, µm* | *↓$E_{on}$, µm* | *↑β* | *↓β* | *$I_{proc}$, µA (at U,V)* | Comments |
|---|---|---|---|---|---|---|---|---|
| 1 | 1 | 26.62 | 26.61 | 25 | 100<br>236 | 196<br>113<br>96 | 1<br>(975) | Current fluctuation during processing between 600nA and 1.3µA, |
| | 2 | - | 23.75 | 26.53 | 89<br>115<br>138 | 138<br>85 | 1.5<br>(1050) | Current fluctuation during processing between 1.3µA and 2.5µA, |
| 2 | 1 | 19.35 | 35.65 | 29.97 | 76 | 147<br>135<br>53 | 1<br>(1000) | Current jump from 1 to 2.5 µA and current fluctuation between 1.6 µA and 6.9µA during processing, |
| | 2 | - | 30.99 | 32.51 | 41<br>84<br>72<br>76 | 106<br>90 | 0.7<br>(810) | Current fluctuation between 0.18 and 1.08 µA during processing, |
| 3 | 1 | 28.53 | 31 | 41.25 | 27<br>29<br>94<br>34 | 128<br>19 | 0.2<br>(1560) | Current fluctuation between 0.15 and 1.5 µA during processing |
| 4 | 1 | 23.20 | 29 | 28 | 104<br>118 | 158<br>141 | 0.9<br>(900) | Current fluctuation between 90nA and 500 nA during processing. |
| | 2 | - | 26 | 26 | 98<br>237 | 266<br>186<br>103 | 0.1<br>(810) | Stable, reproducible, current fluctuation between 110nA and 150 nA during processing. |
| | 3 | - | 25 | 26 | 128 | 211 | 0.11 | Current fluctuation between 45 – 190 nA |

| | | | | | | | | |
|---|---|---|---|---|---|---|---|---|
| | | | | | 204 | 154<br>163<br>131 | (812) | during processing, |
| | 4 | - | 26 | 26 | 127<br>107<br>162<br>140 | 125<br>157<br>107 | 0.28<br>(887) | Current fluctuation between 210 – 610 nA during processing. |
| 5 | 1 | 23.86 | 20 | 18 | 204 | 219<br>195 | 3<br>(743) | Deactivation of emission from 3.5µA to 2.5 µA during processing. |
| | 2 | - | 19 | 19 | 201 | 201 | 1<br>(705) | Stable, reproducible, current fluctuation between 1.1µA and 2.25 µA during processing. |
| 6 | 1 | 25.51 | 28 | 21 | 156 | 221<br>266<br>334<br>174 | 5<br>(1060) | Current fluctuation between 4µA and 8.5 µA during processing. |
| | 2 | - | 17 | 18 | 74<br>290<br>356<br>195 | 221<br>229 | 5<br>(843) | Deactivation during processing from 5µA to 2 µA. |
| | 3 | - | 18 | 17 | 123<br>218<br>205 | 248<br>330<br>278 | 20<br>(980) | Current fluctuation between 17.5µA and 22.5 µA during processing |

| | | | | | | | | |
|---|---|---|---|---|---|---|---|---|
| | | | | | 223 | | | |
| | 4 | - | 17 | 20 | 207<br>289<br>535 | 221 | 50<br>(1110) | Current fluctuation between 45µA and 52 µA during processing. |
| 7 | 1 | 26.11 | 32 | 20 | 128 | 128<br>228<br>171 | - | Current jump from 2µA to 60 µA during up cycle, visible light has been observed during processing at 60 µA. |
| | 2 | - | 20 | 21 | 174<br>114 | 107<br>188 | 70<br>(1320) | Deactivation during processing from 70µA to 58 µA, visible light. |
| 8 | 1 | 29.11 | 33 | 23 | 125<br>89<br>57 | 316<br>46 | 50<br>(1650) | Activation during processing up to 62µA. |
| | 2 | - | 23 | 19 | 36<br>114<br>330 | 144<br>691<br>146<br>65 | - | Unstable FN- plot, maximum achieved current value $I_{max}$ = 280 µA during up cycle. |
| | 3 | - | 15 | 18 | 87<br>435 | 125<br>187<br>59 | 250<br>(1900) | Activation during processing up to 290µA. |

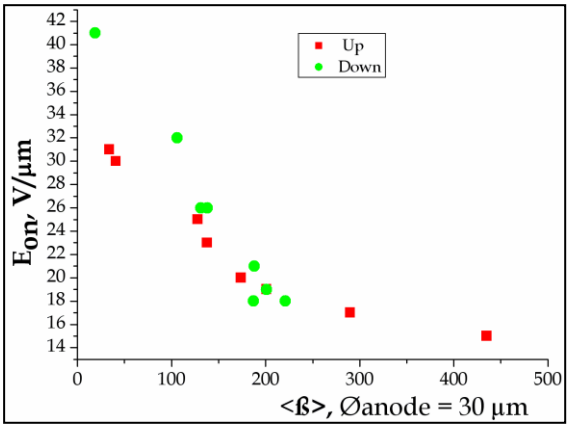


***Figure 52: Onset electric field $E_{on}$ (for 1nA) as a function of the field enhancement factors $ß_{eff}$ of all measured emitters***

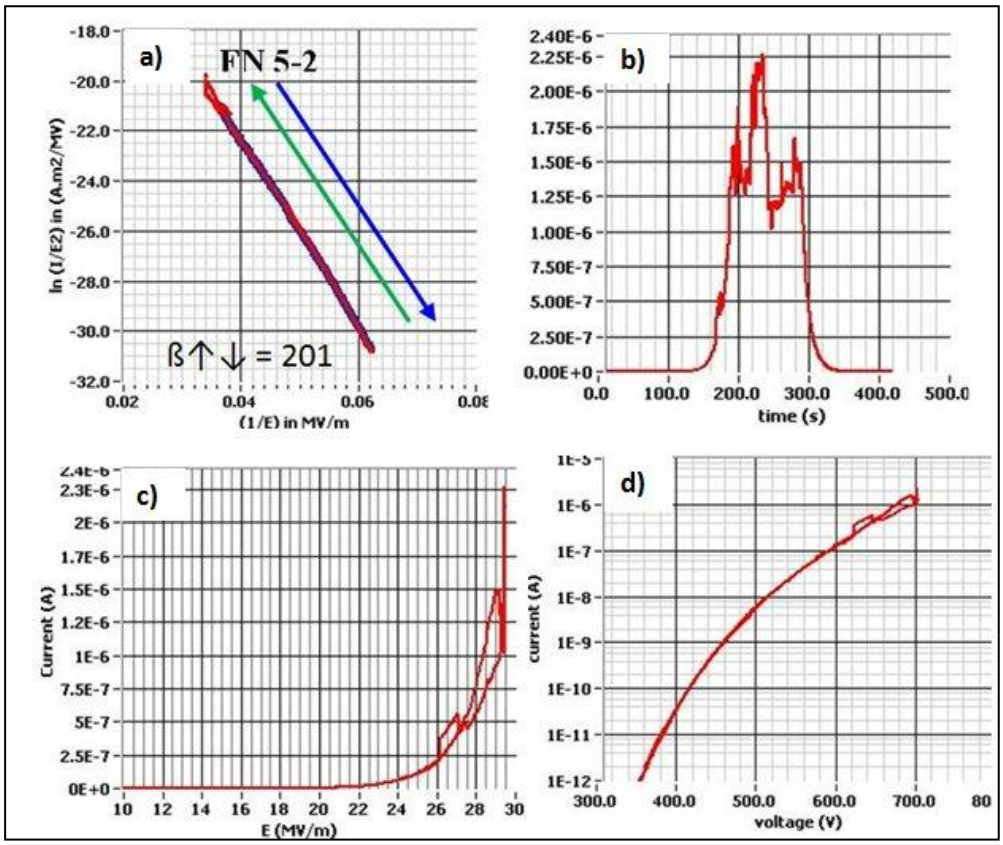


***Figure 53: FN – plot (a) and corresponding I(t) – (b), I(E)– (c) and I(U) – (d) plots of local measurement***

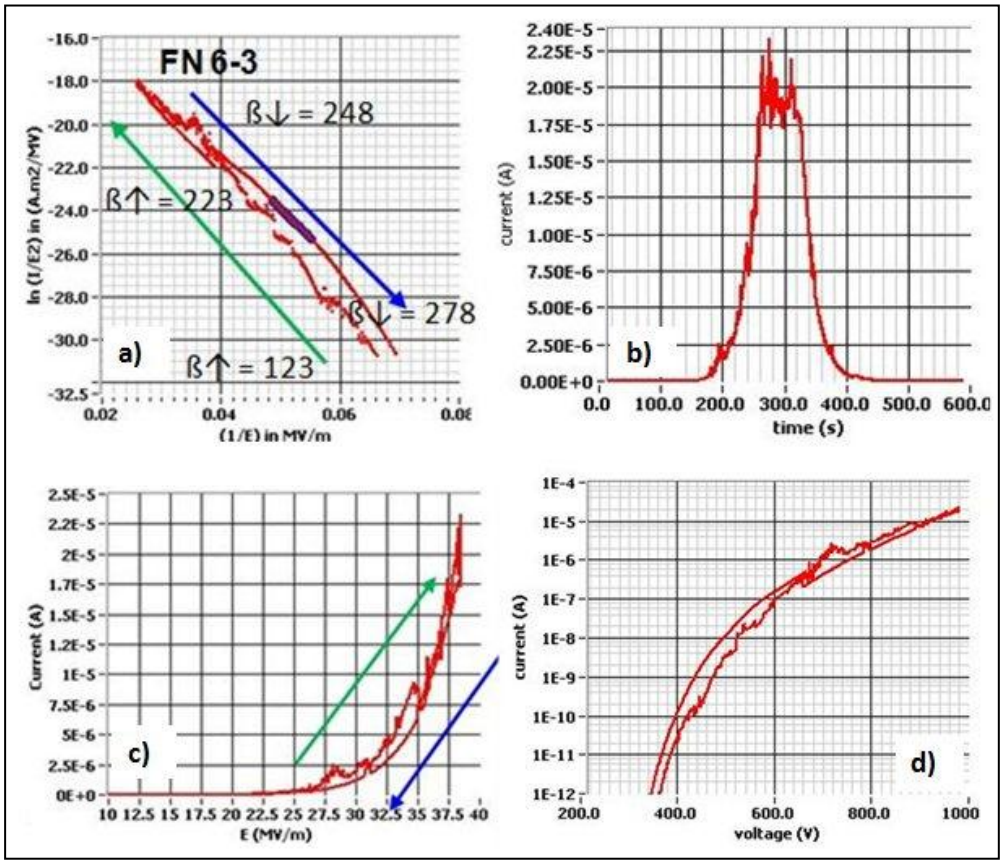


***Figure 54: FN – plot (a) and corresponding I(t) – (b), I(E)– (c) and I(U) – (d) plots of local measurement.***

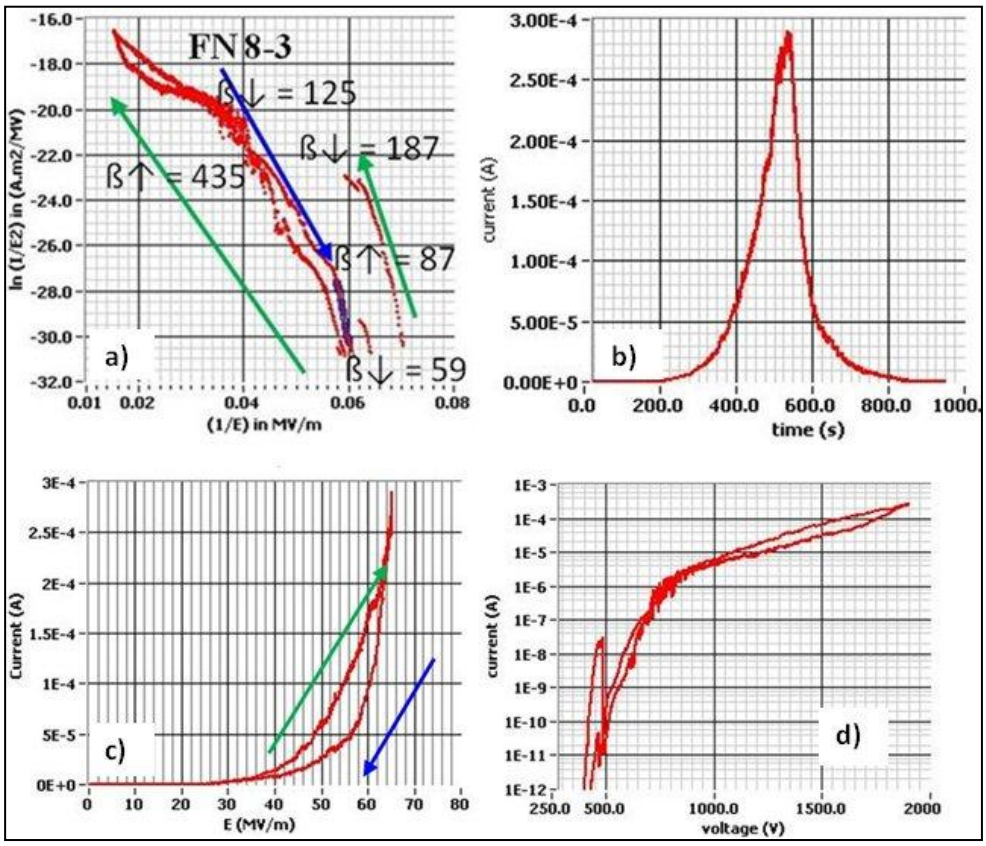


***Figure 55: FN – plot (a) and corresponding I(t) – (b), I(E)– (c) and U(t) – (d) plots of local measurement***

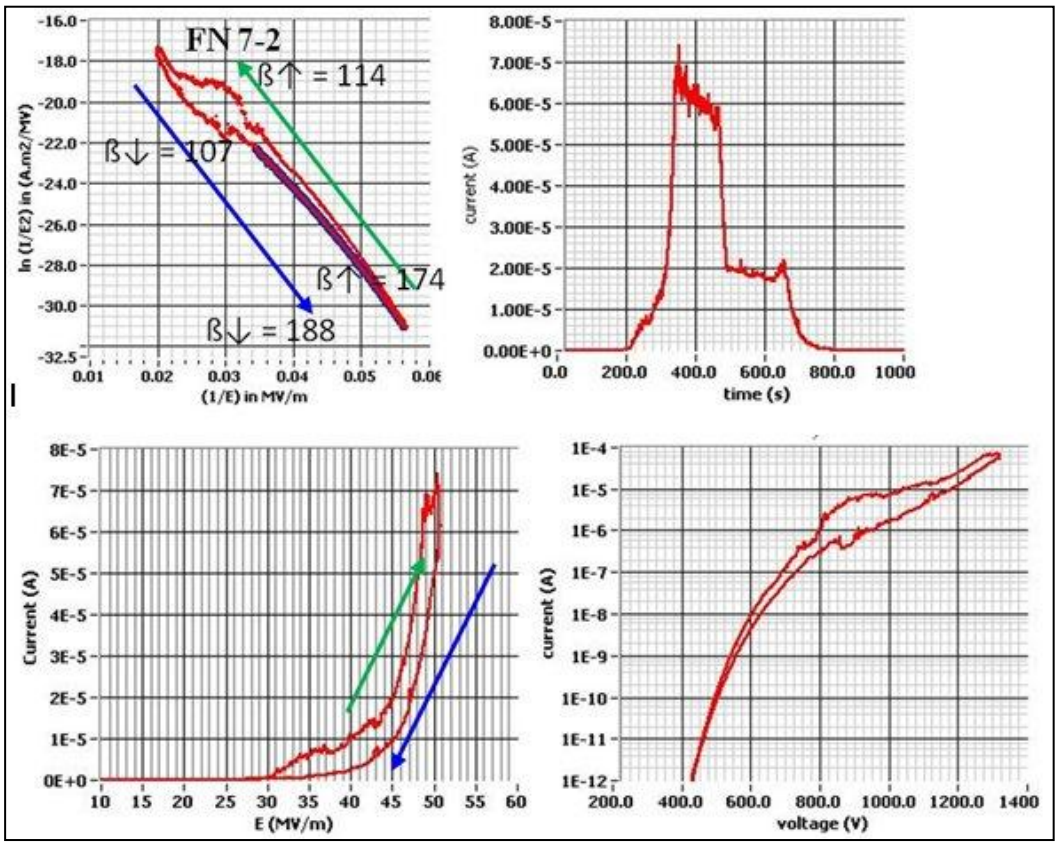


***Figure 56: FN – plot (a) and corresponding I(t) – (b), I(E)– (c) and I(U) – (d) plots of local measurement***

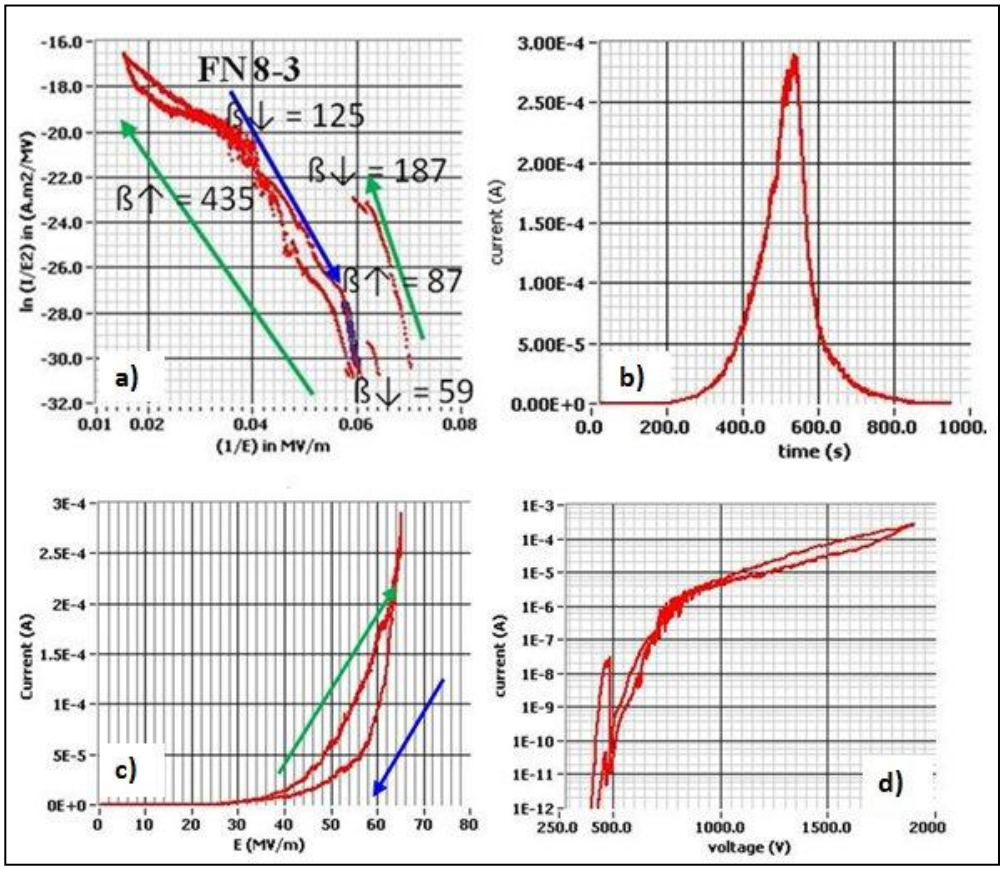


***Figure 57: FN – plot (a) and corresponding I(t) – (b), I(E)– (c) and I(U) – (d) plots of local measurement.***

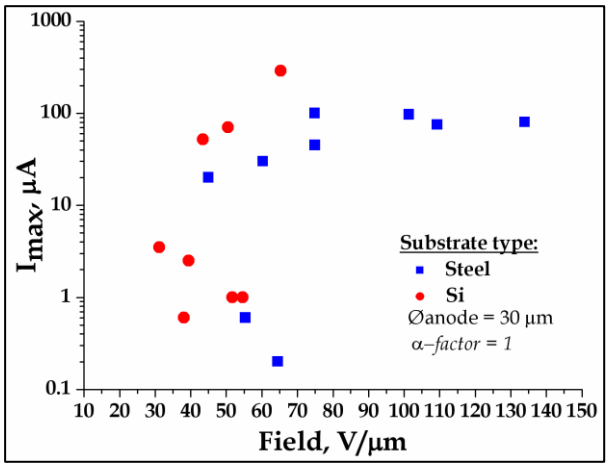


***Figure 58: Maximum achievable current vs. corresponding operation field for single CNW patches on both types of substrates.***

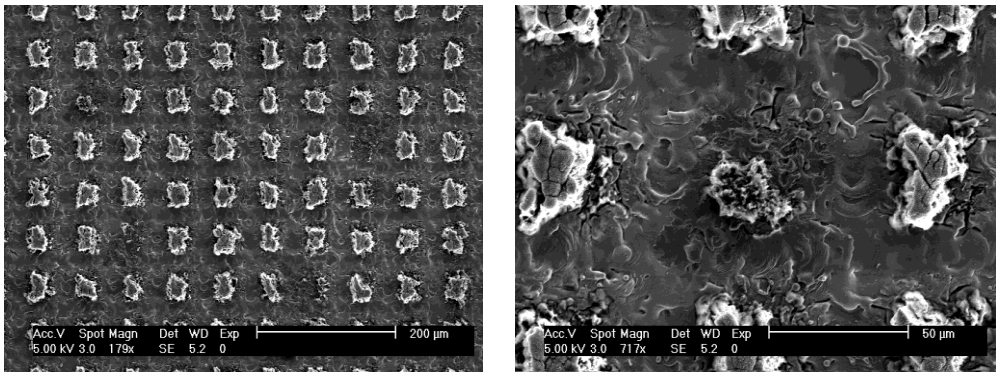


***Figure 59: SEM images of the CNW-blocks array after the local measurements on the left and zooming selected area of the single CNWs-block, which provided a current of about 50-70 µA on the left. The CNW-blocks were strongly modified by the FE current***

The homogeneity of the FE, however, appears rather limited due to the varying shape of the individual CNW patches. Examples of destructions of CNW-blocks by an FE current are shown in Figure 58. It can be seen that partial destruction (observed by FE current) leads to burning of CNWs.

# Summary

Carbon nanowalls are promising as electric field emitters [150]. Laser-structured CNW cathodes have been successfully fabricated on both Si and stainless steel substrates. Following is a brief overview:

- The almost constant value of $\Delta z$ indicates uniform height of CNWs on the substrate.
- The CNW-blocks emitted at an average field level of 22 V/µm for 1 nA current.
- The structured CNW-cathode showed visible alignment and a moderate homogeneous emission. Some degradation of homogeneity can be explained by a variation of the shape of the CNW blocks.
- Local measurements have shown that the achieved current values from a single CNW-block strongly vary between 0.2 – 250 µA. Six from eight emitters have shown a very stable emission current up to 0.75 µA during the first cycles. Stable and reproducible emission up to 20 µA at an applied external electric field of 38 V/µm after several emission cycles has been observed. At higher fields, a partial destruction of the emitters occurred.
- Current saturation effect was observed leading to a horizontal plateau in the I-V curves of CNWs in the µA range.

However, the FE results of these first samples are encouraging, but further optimization is required to exploit their full potential for device applications.

# References


140. Geis MW, Efremow NN, Woodhouse J, McAleese MD, Marchywka M, Socker DG et al. "Diamond cold cathodes" IEEE Electron Device Letters 12: 1991, 456–459
141. Geis M, Twichell JC, Efremow NN, Krohn K, Lyszczarz T "Comparison of electric field emission from nitrogen-doped type Ib diamond, and boron-doped diamond" Applied Physics Letters 68: 1996, 2294–96
142. Himpsel FJ, Knapp JA, van Vechten JA, Vechten DE"Quantum photoyield of diamond (111)–a stable negative affinity emitter" Physical Review B 20: 1979, 624–627
143. Chin chen H, Palnitkar U, Pong W F, Lin I-nan. Singh AP, Kumar R "Enhancement in electric field emission in ultra nanocrystalline and microcrystalline diamond films upon 100 MeV silver Ion radiation" Journal of Applied Physics 105: 2009, 083707
144. Correa EJ, Wu Y, Wen JG, Chandrasekharan R, Shannon MA "Electrical conduction in undoped ultrananocrystalline diamond thin films and its dependence on chemical composition and crystalline structure" Journal of Applied physics 102: 2007, 113706
145. Michaelson S, Ternyak O, Akhvlediani R, Hoffman A, Lafoss A, Arria R et al. "Hydrogen concentration and bonding configuration in polycrystalline diamond films: From micro to nano metric grain size" Journal of Applied Physics 102: 2007, 113516
146. May P.W, Ludlow WJ, Hannaway M, Heard PJ, Smith JA, Rosser KN "Raman and conductivity studies of boron doped microcrystalline diamond, facetted nanocrystalline diamond and cauliflower diamond films" Chemical Physics Letters 446: 2007, 103
147. Obraztsov AN, Zakhidov AA, Volkov AP, Lyashenko DA "Nano-carbon materials for cold cathode applications" Microelectronics Engineering 69 : 2003, 405-411
148. Karabutov AV, Frolov VD, Konov VI, "Diamond/$sp^2$-bonded carbon structures: quantum well field electron emission" Diamond and Related Materials 10: 2001, 840-846

149. Jain HG, Hartmann N, Buck V, Serbun P, Navitski A, Muller G "Electron emission of laser structured carbon nanowalls on Si and stainless steel substrates" Vacuum Nanoelectronics conference 24th international: 2011, 139-140
150. Itoh T, Shimabukuru S, Kawalura M, Nonomura S "Preparation and electron field emission of carbon nanowall by Cat-CVD" Thin Solid films 501: 2006, 314

# 6.Aluminium Oxide Films

It has been reported that carbon nanowalls have been grown under oxygen plasma to improve random orientation for large plane sheets. Takeuchi et al. [151] reported that when carbon nanowalls are deposited in the presence of oxygen plasma, less branching results. Hence, oxygen may improve the orientation of carbon nanowalls. In this work, films were also deposited under oxygen plasma. Films were grown by continued delivery of argon gas through the precursor source (aluminium acetylacetonate) and of oxygen gas by varying their flow rate.

No carbon was observed in the films and instead aluminium oxide was formed. However, an alumina CVD coating by using aluminium acetylacetonate precursor is well known method. Moreover, deposition at low temperatures is still a challenge. Alumina has been at a high demand for the industry for mechanical applications. In this chapter, amorphous and crystalline aluminium oxide films are discussed.

## 6.1. Aluminium Oxide Coatings

Aluminium oxide thin film deposition by CVD has been widely reported. Alumina coatings show various good mechanical properties as well as chemical inertness and high oxidation resistance at high temperatures. Hence, this material is suitable for corrosion protection and as a diffusion barrier [152, 153], as an advanced dielectric [154], for optical coatings [155] and as an electro-chromics [156]. It is clear that the films can have different poly morphs (α, k, δ, γ-$Al_2O_3$) and also amorphous alumina which - depends on the deposition conditions. The thermodynamically stable phase is alpha alumina, much often favored at high temperature and high load applications. However, κ and γ have also proven to be suitable alternatives. For the deposition of alumina various deposition techniques have been used including thermal CVD and PVD. It was reported that polycrystalline δ and γ alumina films can be obtained by CVD and PVD at temperatures greater than 800$^{o}$C and greater than 1000$^{o}$C, respectively. Unfortunately, a high deposition temperature is not favorable for many substrate materials, especially for tooling applications (e.g. steel). The growth temperature of crystalline alumina films can

be reduced by using Plasma-Enhanced-CVD (PECVD) deposition technique. It has proven itself a best alternative, because the use of energetic particles in plasma deposition can dramatically influence the substrate temperature. For example, a significant decrease of growth temperature in the formation of alpha alumina was reported using pulsed magnetron sputtering (>760$^{o}$C) [157]. It is demonstrated that PECVD may be engineered to deliver self-limiting growth of metal oxides using pulse power modulation [157] was developed for the deposition of metal oxide/ alumina films. However, few groups have reported substrate temperatures sufficiently low for deposition on tool steels (500$^{o}$C-900$^{o}$C). α alumina at temperatures lower than 500$^{o}$C is only based on homo-epitaxial and localized epitaxial growth on chromium templates and the deposition rates were not compatible with the requirements of the tool- coating industries. Few groups have reported film formation using plasma enhanced CVD [152]. Due to the insulating properties of alumina utilization of either a high frequency or a pulsed DC discharge is necessary. By driving a discharge amorphous alumina was reported from 200$^{o}$C to 600$^{o}$C [158] growth temperature. The formation of mixtures of γ and α alumina or even pure α alumina utilizing a bipolar pulsed DC generator at 650$^{o}$C substrate temperature was also reported [159]. Hence, the deposition of α alumina coating at low temperatures as well as maintaining the film quality remains a challenge.

## 6.2. Deposition of Alumina

Alumina films were deposited from aluminium acetylacetonate and oxygen as precursors in an ICP- CVD reactor. The aluminium acetylacetonate ($Al(acac)_3$) precursor was sublimated in fluidized bed evaporator at a constant temperature of 150$^{o}$C and then transported to the reaction chamber. For this experiment argon gas was fixed at 27 sccm and oxygen gas was varied from 20 sccm to 40 sccm. The films were deposited at different substrate temperatures between 500$^{o}$C and 800$^{o}$C and with varying pulsed DC biasing voltages from 10V to 100V at 3 amp current. Additionally, the plasma power was varied from 400 Watt to 800 Watt for some experiments.

## 6.2.1.Chemical compositions

Some of the films deposited on silicon were also analyzed using EDX to obtain the chemical composition (Figure 60). The substrates of these films contain no aluminium and chromium which could destroy the findings. The EDX measurements reveal the presence of mainly aluminium (30.30%) and oxygen (56%) in the films. However, the carbon content inside the aluminium precursor is 98% though films are free from carbon contents.

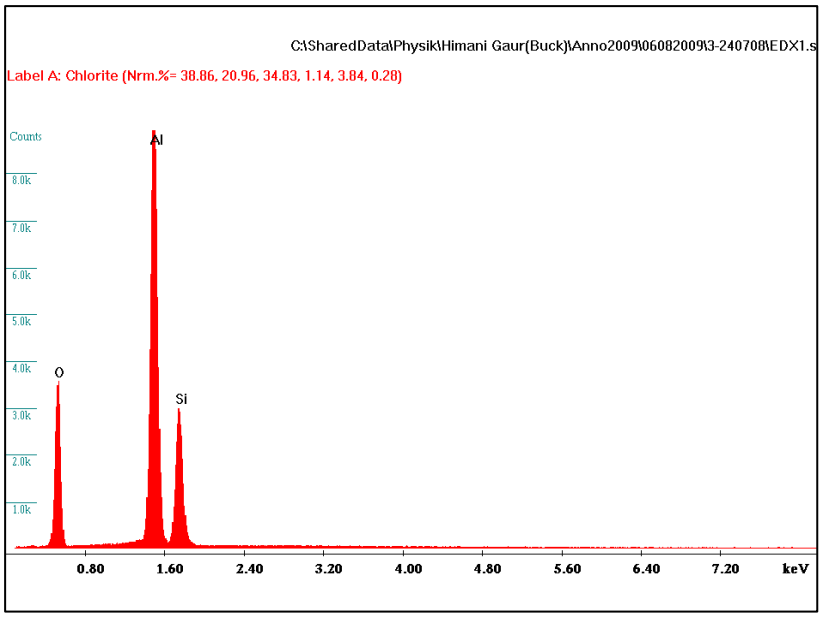


***Figure 60: EDX analysis of the films***

## 6.2.2.Surface morphology and phase analysis

XRD results show that films deposited at lower substrate temperature than 665$^{o}$C were found to be amorphous aluminium oxide films. They were found amorphous at a low flow of oxygen. To achieve crystalline aluminium oxide films were deposited at higher flow rate than 40 sccm. $\gamma$-$Al_2O_3$ phase were found at 40 sccm flow rate and 665$^{o}$C substrate temperature (Figure 61(a)). Furthermore, substrate was biased with pulse DC power and varied from 10 V till 40 V to increase the plasma density and element energy inside the plasma. Figure 61 (b) and Figure 61 (c) show that films are mixtures of poly types ($\alpha$, $\gamma$) of alumina if the substrate was biased by 20 V-40 V pulse DC voltage. The

optimum range of pulse DC biasing voltage for polycrystalline alumina was investigated from 20V to 100V at plasma power 800 Watt. It is described that crystalline alumina films have been deposited at reduced substrate temperatures by ICP-CVD from aluminium acetylacetonate precursor. Further, systematic investigations are necessary to deposit phase pure $\alpha$-$Al_2O_3$ at the lowest substrate temperature possible, and to dope these films. Positive pulse DC substrate biasing has shown a significant improvement of phase formation from $\gamma$ to $\alpha$ constituent. At 20V substrate biasing, the XRD graph (Figure 61) shows the peak of (112) $\alpha$ and small amounts of $\kappa$. However, when positive biasing is increased to more than 20V, the $\gamma$ phase forms at the same plasma parameters

## 6.2.3.In-situ substrate temperature measurement

Low temperature thin film coatings by chemical vapor deposition (CVD) as well as physical vapor deposition (PVD) methods are widely used, nevertheless a deep understanding of the fundamental physical processes during thin film deposition is missing up to now in many areas. Various parameters that need to be considered are shown in Figure 62, where the influencing variables are shown in a flow diagram. To quantitatively understand the connection between the performances of the films and the process parameters of the deposition, it makes sense to subdivide the process into separated successive steps [160] and understand how the specific steps contribute to the properties. Thus, on one hand microscopic film properties depend on the substrate properties (lower branch in Figure 62) and on the other hand on the particle fluxes interacting with the substrate (upper branch in Figure 62).

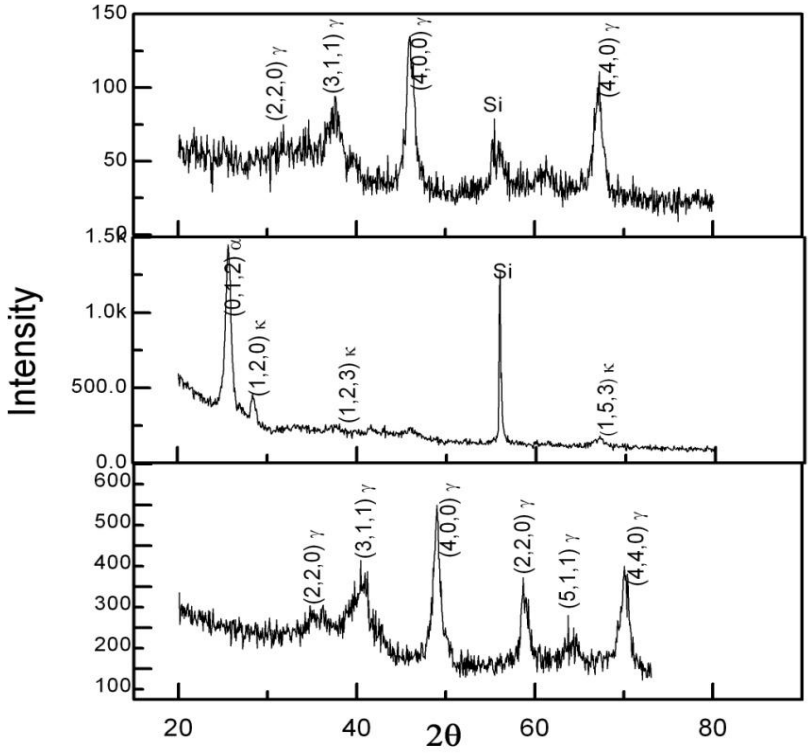


***Figure 61: XRD-patterns of the films grown at 665°C, 800 W plasma power, and varying bias-voltage, 1) No biasing, 2) 20V DC pulse bias, 3) 40V DC pulse bias***

Besides the plasma parameters, the (surface) temperature of the growing film is of the great importance. But the exact determination of this parameter can be very complicated. For example, in conditions where thermocouples and pyrometers cannot really be used, such as at high heat throughput (e.g high rate deposition of diamond) or with "3D substrates" that cannot be tightened to a substrate holder. Obviously, it would be best to measure the temperature precisely within the growing film (or at least directly at the growing film).

In the present study, a new approach is shown to overcome this problem. This approach consists of two parts:

- In-situ surface temperature measurement in hydrogen/oxygen PECVD plasma by using thermo graphic phosphor.
- Alumina deposition in PECVD

The surface temperature in hydrogen/oxygen plasma can be (in principle) optically measured in-situ by using thermo graphic phosphor. Thermo graphic phosphor means if a

small amount of dopant (Cr) in the film is present, which are excitable by a pulsed LED. By this excitation, it produces fluorescence with a constant decay depending on the temperature. This constant decay gives the information about the surface temperature. For this measurement chromium doped alumina (ruby) films prepared by the Sol-Gel method are used here as an example for a thermo graphic phosphor coating. Chromium doped alumina films deposition by PECVD and surface temperature measurement in an argon atmosphere have not been done for this thesis work and proposed for future work. Hence, Cr doped alumina films have been used for surface temperatures in-situ measurement. However, Cr doped films are produced by Sol Gel technique. This approach may help to gain a deeper understanding of the growth mechanism in PECVD processes. However, due to our best knowledge the optical measurement of surface temperatures by thermo graphic phosphor coatings within a plasma environment is shown here for the first time.

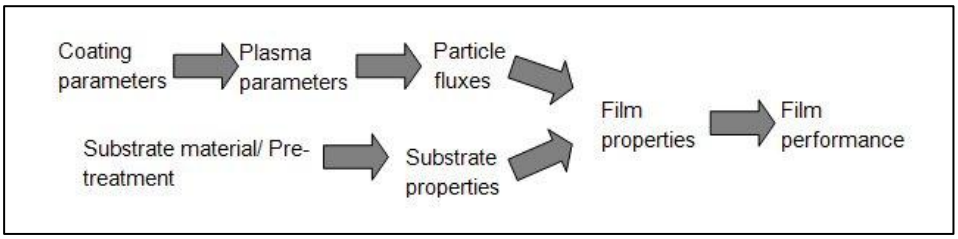


***Figure 62: Scheme of modeling thin films***

## 6.3. Measurement of surface temperature in $H_2$ plasma environment

A relatively new and promising method for measuring surface temperatures under challenging conditions or in radioactive environments like in plasma is the use of thermo graphic phosphor (TP) coatings. Usually, TP's are rare earth doped or transition metal doped ceramic materials, whose phosphorescence decay time, total intensity and spectral distribution, following an excitation, are temperature dependent. So, if a specimen is coated with such a material, its temperature can be determined by measuring and evaluating the luminescence properties after laser light or flash lamp excitation. Thereby, often the temperature dependent decay time of the phosphorescence is evaluated. Recently, Pflitsch et al have shown that thin chromium doped $Al_2O_3$ (ruby) are very promising candidates for that application [162-165], because their phosphorescence

intensity is extremely high and therefore, easy to measure. Furthermore, the phosphorescence characteristics and thus the surface temperatures can be easily determined by exciting the samples with a simple LED setup [165].

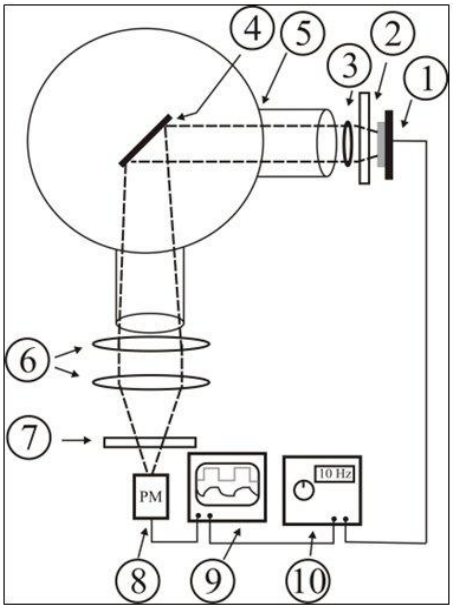


***Figure 63: The experimental setup for phosphorescence lifetime measurement, consisting of 1-LED, 2-Filter, 3-lenses, 4-Specimen, 5- ICP-CVD-reactor, 6-Lenses, 7-Filter (RG6 65), 8-Photomultiplier, 9-Oscilloscope, 10-LED-controller***

In the present study Sol-Gel-technique, prepared thin chromium doped $Al_2O_3$ films were used as a test specimen. The coating procedure is described in detail in reference [14]. The chromium concentration within the films was 1.1 %. It is reported that 1.1% is the most useful dopant-concentration for the application as the surface temperature sensor [164].

Prepared samples were mounted on the sample holder within the ICP-reactor and subsequently optically analyzed by the setup shown in Figure 63. The phosphorescence was excited by a pulsed UV-light LED emitting at 375 nm (maximum power 285 mW). The light was focused on the specimen using two lenses, while a band pass filter (312nm $< \lambda <$ 530nm) was used to block the UV-LED emission in the red spectral region. The phosphorescence emitted by the sample after UV excitation was focused by a condenser through a low ass filter (RG 665) on a photomultiplier. Finally, the electronic signal from the PM tube was then measured and stored by a digital oscilloscope.

## 6.3.1.Spectral Analysis

In order to analyze the emission of running hydrogen/oxygen plasma the following experiment was carried out: The ICP-reactor was floated with constant flows of hydrogen (100 sccm) and oxygen (100 sccm) while the pressure was kept constant at 0.23 mbar.

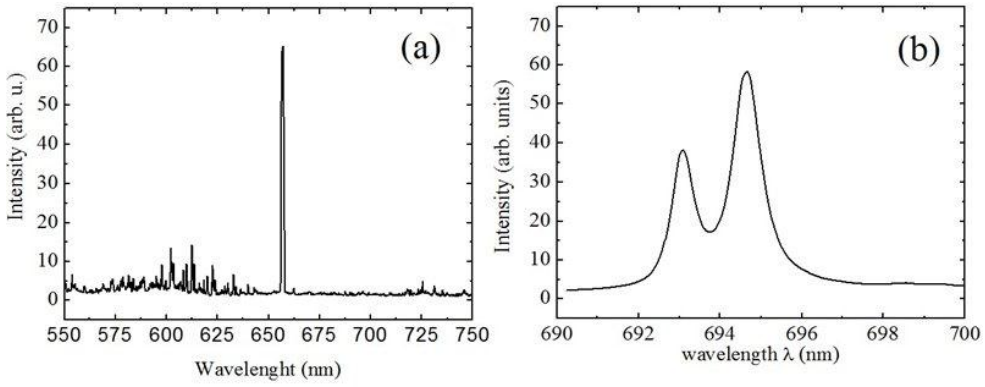


***Figure 64: Spectra of (a) a $H_2$ -$O_2$ mixture plasma ($H_2$:$O_2$=1:1) running at 150 W power and 0.23 mbar, and (b) the phosphorescence of a thin ruby film which was excited by UV-light at 375 nm.***

A plasma was ignited then by using a microwave power supply running at 150 W, and the light emitted was subsequently analyzed by a high resolution spectrometer. A large number of sharp transitions are observed in that spectrum (Figure 64), which is typically for the plasma emission of a hydrogen/oxygen mixture. The strongest emission is observed at 656 nm.

Furthermore, the phosphorescence of several prepared thin ruby films was analyzed. After UV-light excitation, they show two rather sharp phosphorescence emissions at around 693.0 nm and 694.0 nm (Figure 64b), which are the so-called R-lines of ruby. These transitions are measured in the following section for calculating the surface temperature. However, the spectrum of the hydrogen plasma contains no transition in the range between 658 nm and 714 nm, and thus the emitted phosphorescence light of the ruby film used for surface temperature analysis is not disturbed by any plasma emission.

Consequently, it can be measured separately by using adequate optical filters or a monochromator. Nevertheless, it is in principle possible that the phosphorescence of ruby is also excited by the plasma itself; but as the LED-excitation is pulsed and the plasma is

running steadily the phosphorescence induced by the LED-excitation is easily separated from the phosphorescence induced by the plasma; the latter one is just an offset to the signal. In order to measure the phosphorescence lifetime of a thin ruby film mounted within the hydrogen/oxygen plasma environment (150 W power, 0.23 mbar, $H_2$:$O_2$=1:1), the equipment shown in Figure 63 was used.

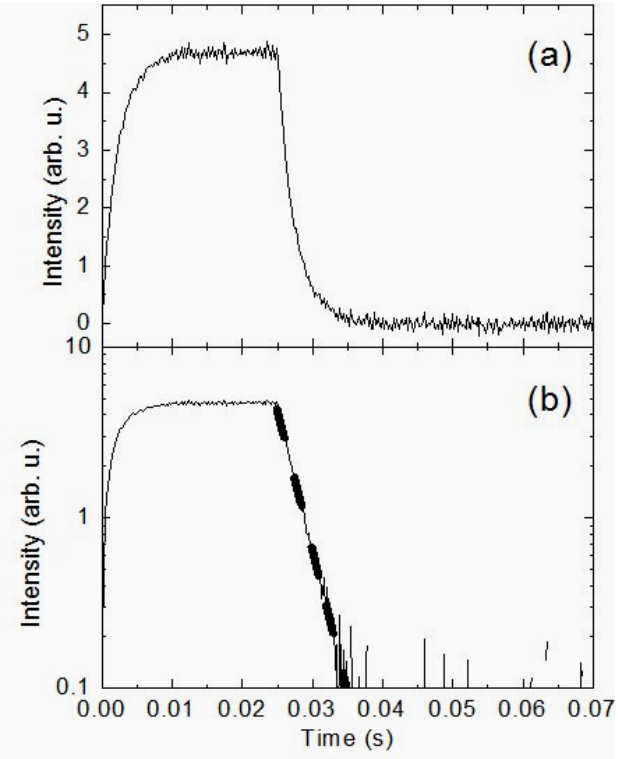


***Figure 65: Phosphorescence of thin ruby films measured in a hydrogen plasma environment as a function of time (a) on a linear scale and (b) on a logarithmic scale. For t between 0.00s and 0.025s the LED was switched on and for t between 0.025s and 0.007s the LED was switched off. The shown curves are the averages over 200 pulses. The dashed curve was fitted to the experimental data.***

In this case, the ruby phosphorescence was excited by LED pulses of 0.025s pulse duration. The resulting phosphorescence intensity is shown in Figure 65 as a function of time, (a) on a linear scale and (b) on a logarithmic scale. For times between 0.00s and 0.025s the LED was switched on; one can observe a steadily increasing phosphorescence intensity, which is then becoming saturated at around 0.01 s. After the LED is switched off (t=0.025 s), the phosphorescence intensity decreases with time. It is easily seen on the linear scale (Figure 65 a) but better on the logarithmic scale (Figure 65 b), that the phosphorescence is decreasing exponentially with time. Thus, an exponential decay can

be fitted to the curve (dashed line in Figure 65b) from which the phosphorescence lifetime is deduced (for further details of the fitting routine see refs [163, 165]).

In the present case the fitted lifetime $\tau$ is 266 μs. The lifetime is strongly temperature dependent and thus the film temperature can be calculated from the lifetime. Calibration experiments which we performed recently [162, 164] reveal a film temperature of about 346°C corresponding to the measured lifetime of 266 μs. Thus the actual surface temperature of the specimen is around 320°C higher than the temperature of the sample holder and surrounding walls of the CVD chamber which are at RT. Obviously, the specimen is heated by the running plasma.

# Summary

Hence it is concluded that aluminium oxide amorphous and crystalline films can be deposited by a using metal organic precursor. Thin films of doped $\alpha$-$Al_2O_3$ can be used as thermo graphic phosphor coatings for optical surface temperature measurement under challenging conditions, such as moving objects or radioactive environments. Here, it is shown that surface temperature can be measured by this approach in a running plasma environment.

In future it is possible to deposit single phase $\alpha$ aluminium oxide films at low substrate temperatures however further research is required to tailor the plasma parameters which match the energy required for the formation of $\alpha$ $Al_2O_3$.

# References


151. Takeuchi W, Takedia K, Hiramatsu M, Tokuda Y, kanu H, Kimura S et al.“Monolithic selfstaining nanographene sheet using plasma enhanced chemical vapor deposition” Physics Status Solidi 207: 2010, 139-143
152. Schneider JM, Sproul WD, Voevodin AA, Matthews A “Crystalline alumina deposited at low temperature by reactive ionized magnetron sputtering” Journal of Vacuum Science and technology A 15: 1997, 1084-1088
153. Serra E, Benamati G, Ogorodnikova OV “Hydrogen isotopes transport parameters in fusion reactor materials” Journal of Nuclear Matter 255: 1998, 105-115
154. Cho B-O, Lao SX, Chang JP “The origin and effect of impurity incorporation in plasma enhanced $ZrO_2$ deposition” Journal of Applied Physics 93: 2003, 9345-9351
155. Martinu L, Poitras D “Plasma deposition of optical films and coatings: A Review” Journal of Vacuum Science and Technology A 18: 2000, 2619-2645
156. Tracy CE, Benson DK “Preparation of amorphous electrochromic tungsten oxide and molybdenum oxide by plasma enhanced chemical vapor deposition”Journal of Vacuum Science and Technology A 4: 1986, 2377-2383
157. Szymanski S F “Effect of wall conditions on the self-limiting deposition of metal oxides by pulsed plasma-enhanced chemical vapor deposition” Journal of Vacuum Science and Technology A 25 : 2007, 1493-1499
158. Lin CH, Wang HL, Hon MH “Preparation and characterization of aluminium oxide films by plasma enhanced chemical vapour deposition” Surface Coatings and Technology 90: 1997, 102-106.
159. Tabersky R, van den Berg H, König U “Plasma chemical vapour deposition of aluminium oxide on hard metals” International Journal of Refractory Metals and Hard Materials 14: 1996, 79-84,
160. V. Buck “Microanalysis and modelling of tribological coatings” Surface and Coatings Technology, 57: 1993, 163–168
161. A. R Barron “CVD of insulating materials” in: W. S. Rees Jr. (Ed), “CVD of Nonmetals”, 262, VCH, Weinheim, 1996,

162. Pflitsch C, Viefhaus D, Atakan B "CVD of Thin Ruby Films on Si(100) and Stainless Steel for Surface Temperature Sensor Applications" Chemical Vapour Deposition 13: 2007, 420

163. Pflitsch C, Siddiqui RA, Atakan B " Phosphorescence properties of sol-gel derived ruby measured as functions of temperature and $Cr^{+3}$ content Applied Physics A 90:2008, 527-532

164. Pflitsch C, Siddiqui RA, Eckert C, Atakan B "Sol-gel deposition of chromium doped aluminium oxide films (ruby) for surface temperature sensor application" Chemistry of Materials 20: 2008, 2773

165. Atakan B, Eckert C, Pflitsch C "Light emitting diode excitation of $Cr^{3+}$: $Al_2O_3$ as thermographic phosphor: experiments and measurement strategy" Measurement Science and Technology 20, 075 (2009)304

# Summary and Future Prospects

Graphene based nanostructures are worth investigating because of its unique properties like high charge mobility and chemically inertness. One of the emerging structures from this family is carbon nanowalls. CNWs can be produced by ICP−CVD using metal organic precursor on a different substrate like silicon and steel. This is the first investigation of the production of carbon nanowalls without using additional catalyst and reactive gases. It can be deposited at various substrate temperatures (RT-800$^{o}$C). As an application, carbon nanowalls are promising as electric field emitters [150]. Laser-structured CNW cathodes have been successfully fabricated on both Si and stainless steel substrates. In brief, the work can be summarized as follows:

- SEM studies explain that the size of the carbon wall is influenced by various plasma parameters like substrate temperature, argon flow, and plasma power.

- EDX, SIMS show that aluminium content inside the film can be controlled by flow of argon gas, and it also significantly influences the size of the walls.

- Raman analysis shows the typical CNWs peaks at high $I_D$/ $I_G$ ratio and is reported as the smallest size of CNW until now.

- TEM images conclude that there are some crystallite inclusions inside the graphitic matrix. It is evident from XPS that the crystalline inclusions are nothing but aluminium carbide ($Al_4C_3$).

- The measured effective electric field of the film is 3.7 V/μm (for 1 μA), hence it has applications as a cold cathode, however, CNW-blocks are emitted at an average field level of a 22 V/μm.

- The structured CNW-cathode showed a visible alignment and a moderate homogeneous emission. There is some degradation of homogeneity that can be explained by the variation of the shape of the CNW blocks.

The interesting investigation was also to produce aluminium oxide films by using the same method described and adding oxygen gas during the deposition. Thin films of doped $\alpha$-$Al_2O_3$ can be used as thermo graphic phosphor coatings for optical surface temperature measurement under challenging conditions, such as moving objects or radioactive environments. Here, it is shown that the surface temperature can be measured by this approach in a running plasma environment.

In future, the structuring of CNWs for device fabrication is possible. The work intends to signify that CNWs can be produced by different metal organic precursors like titanium metal organic precursor etc. To explore the properties of CNWs synthesized by different sources, it will be worth investigating in the field of graphene-based nanostructures. The initial results of field emission of CNWs sample are encouraging, but further optimization is required to exploit their full potential for device applications. In the direction of aluminium oxide, it is possible to deposit single phase $\alpha$ aluminium oxide films at low substrate temperatures. However, further research is required to tailor the plasma parameters that match the energy required for the formation of $\alpha$ $Al_2O_3$.

# Index

## *T*



## *W*



## *X*



## *Z*

# List of Abbreviations

| | |
|---|---|
| ASTeX | Applied Science and Technology, Inc |
| CCD | Charge Coupled Device |
| CNT | Carbon nanotube |
| CNWs | Carbon nanowalls |
| CVD | Chemical Vapur deposition |
| DC Plasma | Direct Current Plasma |
| ED | Energy-Dispersive X-ray Spectroscopy |
| FEG | Field Emission Gun |
| FES | Field Emission Scanning Microscope |
| HFCV | Hot Filament CVD |
| HRTEM | High Resolution Tunneling Electron Microscope |
| ICP-CVD | Inductively Coupled Plasma Enhanced CVD |
| IMLS | Integral measurement system with luminescent screen |
| LED. | Light Emitting Diaode |
| MBE | Molecular Beam Epitaxy |
| MFC | Mass Flow Controller |
| MWPECVD | Microwave plasma enhanced CVD |
| NIRIM | National Institute of Research of Inorganic Materials |
| NRA | Nuclear Resonance Analysis |
| NEA | Negative Electron Affinity |
| PECVD | Plasma Enhanced Chemical vapor deposition |
| PMMA | Poly Methyl Methacrylate |
| PVD | Physical Vapor Deposition |
| RF power | Radio Frequency Power |
| SEM | Scanning Electron Spectroscopy |
| SIMS | Secondary Ion Mass Spectroscopy |
| STM | Scanning Tunneling Microscope |
| TEM | Tunneling Electron Microscope |
| TP | Thermographic Phosphor |
| XPS | X-ray Photon Spectroscopy |

# Publications from this thesis

- **Jain H.G**, Karacuban H, Krix D, Becker H-W, Nienhaus H, Buck V, "Carbon nanowalls deposited by inductively coupled plasma enhanced chemical vapor deposition using aluminium acetylacetonate as precursor", Carbon 49: 2011, 4987-4995
- **Jain HG**, Hartmann N, Buck V, Serbun P, Navitski A, Muller G,*"Electron emission of laser structured carbon nanowalls on Si and stainless steel substrates"* Vacuum Nanoelectronics conference: IEEE: 2011, 139-140
- **Gaur H,** Pflitsch C, Atakan B, Eckert C, Beluri I, Kluska S, Buck V, "New approach for in-situ measuring the substrate temperature during PECVD experiments: polycrystalline alumina deposition by ICP-CVD and substrate temperature measurement in a plasma environment", 17th Plansee Seminar 2009, Vol. 4, HM 34/1
- Barhai PK, Sharma R, Yadav A.K, Singh A.K, **Gaur H**, Buck V, *"Surface modification of PMMA with DLC using RF-PECVD",* Vienna Conference Proceedings 2009.
- **Gaur H**, Buck V "Study of Al doped diamond like carbon films deposited by ICP- CVD using metal organic precursors" 14. Fachtagung Plasmatechnologie – PT 14, 2009 00